Optical properties of vanadium oxide nanostructures synthesized by Laser Pyrolysis

by

Lerato David Shikwambana

A dissertation submitted to the Faculty of Science, University of the Witwatersrand, Johannesburg, in fulfilment of the requirements for the degree of Master of Science.

05 October, 2011

Declaration

I declare that this dissertation is my own work. It is being submitted for the Degree of Master of Science in the University of the Witwatersrand, Johannesburg. It has not been submitted before for any degree or examination in any other University.

_____

(Signature)

_____ day of _____ 2011

Abstract

In this work, the primary investigation has been on the development of the laser pyrolysis setup and its optimization for the synthesis of nano-size VO_{2-x} films. More specifically the focus was on making VO_{2-x} depositions using various laser pyrolysis parameters and establish in this way (1) an optimum laser wavelength threshold for the photon induced dissociation of the molecular precursors while the thermal contribution was kept minimal by using low power density (laser energy of 30 W) and (2) the lower threshold for pure thermal contributions by working with wavelengths far from resonance in order to minimize pure photon induced contributions. The interest in synthesizing nano-size VO_{2-x} materials stems from the low metal-insulator transition temperature at near room temperature with opto-electronic and thermo-electronic properties that can be used in specialised applications.

A large number of samples were synthesized under various conditions and annealed under argon atmosphere for 17 hours. XRD analysis identified the VO_2 (B) and/or β-V_2O_5 vanadium oxide phases characteristic for certain samples grown under optimum conditions. Raman spectroscopy also confirmed these vanadium oxide phases with bands observed at 175, 228, 261, 303, 422 and 532 cm^{-1}. SEM analysis revealed a plethora of different nanostructures of various size and shapes. The particles have a range of sizes between 55 nm to 185 nm in diameter. The particles showed morphologies which included nano-rods, nano-spheres and nano-slabs. An interesting phenomenon was observed on the samples synthesized with high power density, which was observed and reported by Donev

et al. EDS analysis on the particles was also used to probe the elemental composition of the sample. Optical studies were performed on the samples which showed transitions in the visible and infrared region in accordance with the ones observed in the international literature using different nano-synthesis methods.

Dedication

To my loving wife, Boitumelo Shikwambana

for her support, believe and inspiration.

To my parents, Andrew and Flora Shikwambana, for bringing me up and giving me education.

To my sister, Tinyiko Shikwambana for her support.

Acknowledgements

I would like to thank God for His love and mercies through my walk thus far. I would also like thank Professor Andrew Forbes and Professor Elias Sideras-Haddad for giving me the opportunity to conduct my research in well-established institutions being the CSIR National Laser Centre and the University of the Witwatersrand. I would like to thank them for the advice throughout my Masters.

A special thanks to Dr. Bonex Mwakikunga who made sure that everything concerning my work was done. I would also like to thank him for showing confidence in my work and me. I appreciate the advices and support you gave me.

I would also like to thank Malcolm Govender, Steven Nkosi, Darryl Naidoo, Bathusile Masina and Kaminee Maduray for all their input and making this research fun.

Table of Contents

List of Figures

List of Tables

Chapter 1: Literature Review

1.1 Nanoscience and nanotechnology

1.1.1 Overview

"I want to build a billion tiny factories, models of each other, which are manufacturing simultaneously… The principles of physics, as far as I can see, do not speak against the possibility of manoeuvring things atom by atom. It is not an attempt to violate any laws; it is something, in principle, that can be done; but in practice, it has not been done because we are too big." these were the words of the Physics Nobel prize winner, Richard P. Feynman, in his lecture in 1960. What Feynman supposed in his lecture is today called nanoscience. This is the study of the controlling of matter on an atomic and molecular scale. Nanoscience generally deals with structures of the size 100 nanometers or smaller in at least one dimension. The nano-structures can be manipulated to perform various or specific functions in devices or pharmaceutical products [1]. To be able to build these devices and make these pharmaceutical products, the knowledge of an interdisciplinary science in areas such as physics, chemistry, mathematics, biology, toxicology and environmental sciences is imperative [2].

Prior to Feynman's lecture in the 1950s minimal experiments were conducted on small metal particles. It was in 1956 that Uhlir *et al* [3] reported the observation of the first porous silicon but it was only in 1990 that fluorescence in room temperature was observed [3]. There were other groups (in the 1950s) which synthesized alkali metal nanoparticles by vaporising sodium or potassium metal

and condensing them on cooler materials [3]. In 1963 Wagner and Ellis proposed a mechanism by which particles act as seeds for one-dimensional growth, which they named the Vapour-Liquid-Solid (VLS) mechanism [4]. A further development of the VLS mechanism was done by Givargizov *et al* in 1975 [4]. This work expanded on the details of this process, describing the relevant processes involved and predicting the morphology expected from the relative importance of these processes under various conditions. The relevant processes were specified as the dissociation of supply material at the particle surface, incorporation of growth material into the particle, diffusion through the particle, and nucleation at the interface [4].

Although work has been done to understand the growth of nano-structures, it was only in the 1980s that research started to grow; this was due to the emergence of various synthesis methods introduced. The synthesis methods were the RF plasma, chemical methods, thermolysis and pulsed laser methods [3]. In the RF plasma method the starting metal is wrapped around high voltage RF coils, the metal is heated above its evaporation point forming high temperature plasma. The metal vapour is then collected on a cooler substrate; this is where the nanoparticles are formed. Chemical methods involve chemical reactions to synthesize the nanoparticles, this usually involves heating the mixture at a particular temperature and time. Thermolysis is used for solids with metal cations, and molecular anions or metal organic compounds, the solids are decomposed at high temperature to form nanoparticles. The material is placed in an evacuated tube and heated for some time. The pulsed laser method of thin film and

nanoparticle growth involves evaporation of a solid target in an ultra high vacuum chamber by means of short and high-energy laser pulses.

1.1.2 The present and future state of nanoscience and nanotechnology

Public authorities and enterprises invest billions of dollars worldwide in research and nanotechnology application because nanotechnology is regarded as the future key technology [5]. Nanotechnology is seen to have many applications in areas such as electronics, telecommunications, data processing, biotechnology, precision technology and material science [5]. The enhancement in technology will help people in their everyday lives, better medicine can be made, faster computers can be produced and smart windows can be manufactured. Research on nanotechnology is growing rapidly as seen from the number of nanotechnology publications which grew from 11 265 in 1991 to 64 737 in 2005 [6], shown in Figure 1.1.

The United State of America (USA) and China are the leading countries in producing nanotechnology papers accounting 40% of the worlds production, Table 1.1 shows the 20 leading countries in the production of nanotechnology articles in 2005 [6].

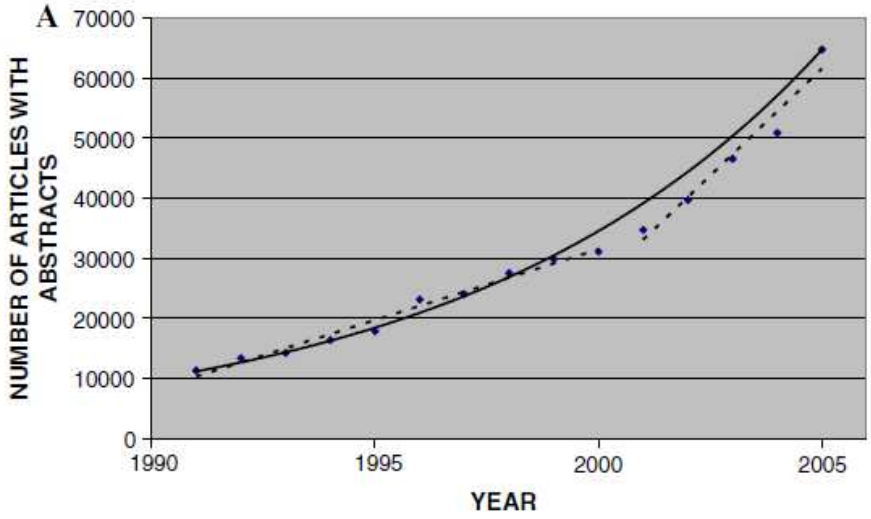

Figure 1.1: Science Citation Index (SCI) and Social Sciences Citation Index (SSCI) articles versus time total records retrieved [6].

Nanotechnology research is still in its infancy in South Africa but the government is investing money in 'nano-activies' to make developments in nanotechnology [7]. In the year 2002 the South African Nanotechnology Initiative (SANi) was formed to create awareness to South Africans about nanotechnology. The group, together with the government, launched a 10 year plan for nanotechnology. Strategy for the first three years is shown in Table 1.2. [8].

In 2008/2009 the group decided to spend some of the R50 000 000 in the characterization equipment. The equipment is expensive but very important because it enables one to observe what has been synthesized. Vanadium dioxide (VO_2) nanostructures are one example of the material that can be analysed from these instruments.

Table 1.1: Countries producing most nanoscience/nanotechnology articles (2005).

Country	Number of papers
USA	14750
People R China	11746
Japan	7971
Germany	5665
South Korea	4098
France	3994
England	2786
Italy	2297
Russia	2185
Taiwan	2165
India	2103
Spain	1700
Canada	1579
Netherlands	1130
Poland	1105
Australia	1048
Singapore	1045
Switzerland	1009
Sweden	944
Brazil	932

Table 1.2: Estimated budget for the implementation of the nanotechnology strategy for the first 3 years [8].

Key Interventions	2006/7 (R000's)	2007/8 (R000's)	2008/9 (R000's)
Cross-cutting S&T and Frontier Programmes			
Capacity Building (R&D and HRD)	30 000	60 000	80 000
Research and Innovation Networks	10 000	20 000	20 000
Flagship Projects	20 000	30 000	50 000
R&D Infrastructure			
Characterisation Centres	40 000	40 000	50 000
Total per year	**100 000**	**150 000**	**200 000**
TOTAL FOR 3 YEARS			**450 000**

1.1.3 Objectives of the project

The present research team, based at the Council for scientific and industrial research- National Laser Centre (CSIR-NLC) and the University of the Witwatersrand, has in the past synthesized vanadium oxide nano-structures using the laser pyrolysis (LP) and ultra-sonic spray pyrolysis (USP) techniques. Vanadium dioxide (VO_2) is of interest because of its thermo-chromic property which has an application in energy efficient windows. In the past main focus in synthesizing these materials has been on the USP method. In this work our aim to achieve the following:

i. Improve the laser pyrolysis setup and repeat systematically some of the experiments that have led this group to the discovery of VO_2 nano-belts by laser pyrolysis and thermal annealing.
ii. Obtain thin films and powders by (a) varying laser power while keeping the laser wavelength constant and (b) varying wavelength and keeping power constant, in order to find the link between laser power on the VO_2 stoichiometry, structure, shape, and size of the particles.

1.2 Vanadium dioxide (VO_2)

1.2.1 Vanadium in South Africa

Vanadium is a soft, silvery grey and ductile transition metal with a high boiling and melting point, it is also considered toxic. China and the USA produce vanadium but South Africa is the major producer, producing about 40% of the

world's vanadium. South Africa has five major vanadium mines; Brits Vanadium, Rhovan, Vantra, Highveldt Steel & Vanadium Mill and Vantech. Vanadium is usually produced as vanadium pentoxide (V_2O_5) and most of it (about 85 %) is used as a steel additive. It is also used as a catalyst in the production of sulphuric acid and used in the aerospace industry in titanium alloys [9].

1.2.2 VO_2 particles and thin films

Vanadium oxides have many phases with the general formulas V_nO_{2n+1} and V_nO_{2n-1} [10]. The most popular vanadium oxides that have been produced and reported on are vanadium trioxide (V_2O_3), vanadium pentoxide (V_2O_5) and vanadium dioxide (VO_2). A noticeable difference in these oxides is their metal-to-insulator transition (MIT) temperature: V_2O_3 has a transition temperature at about -123^oC [11], V_2O_5 at about 375^oC [12] and VO_2 at about 68^oC [13], as shown in Table 1.3. VO_2 is of interest because its transition temperature, shown in Figure 1.2, is closer to room temperature compared to V_2O_5 and V_2O_3. The transition temperature of VO_2 can be lowered or increased using dopants such as tungsten and molybdenum depending on the application purpose.

Table 1.3: Transition temperature of vanadium oxide phases as a function of the oxygen to vanadium ratio.

Vanadium phase	Transition temperature (^{o}C)
VO	-148
V_2O_3	-123
V_5O_9	-138
VO_2 (M)	68
V_6O_{13}	-143
V_2O_5	375

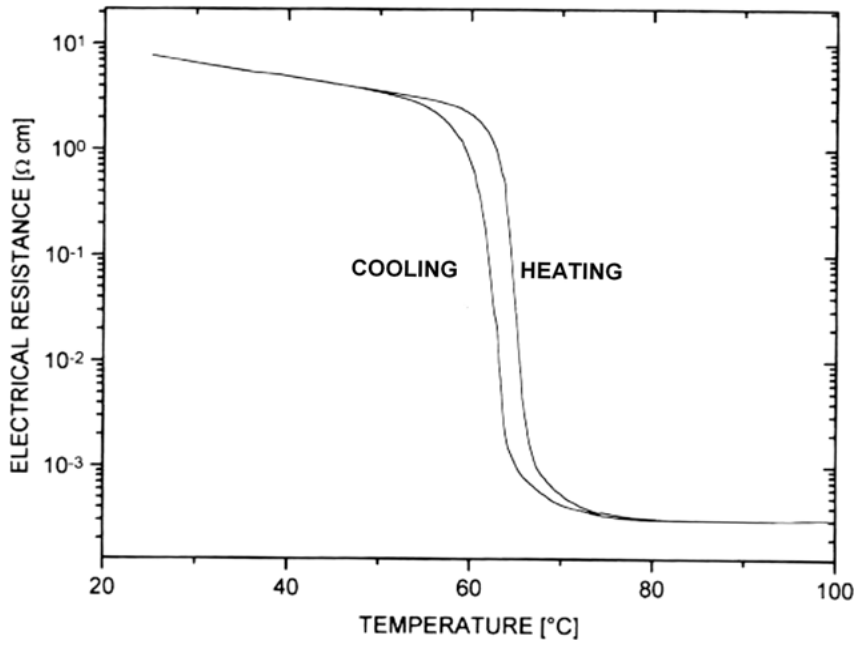

Figure 1.2: Measured hysteresis curves during the insulator–metal transition of a thin VO_2 film for electrical resistance [13].

Bulk VO_2 crystals exhibit the metal–insulator transition (MIT) at a critical temperature of about 68 ◦C accompanied by a first-order structural phase transformation from a monoclinic ($P2_1/c$) to tetragonal (rutile—$P4_2/mnm$) structure, characterized by a small lattice distortion along the c-axis [13]. As a transition-metal oxide with narrow d-electron bands, this strongly correlated electron system is extremely sensitive to small changes in extrinsic parameters such as temperature, pressure, or doping [13].

VO_2 is electrically conducting at temperatures higher than 68^oC and is electrically insulating at temperatures lower than 68^oC. It also has an interesting optical property shown in Figure 1.3, at temperatures below the transition it allows more infrared radiation (IR) and above the transition temperature it allows less IR. The reason for this switching is because of the difference in structure of VO_2 at low and high temperature. Figures 1.2 and 1.3 show hysteresis curves for electrical resistance and optical reflection, respectively, measured for typical thin films of VO_2 of order 100 nm thicknesses.

The driving mechanism of the transition is still not known but the theory suggests that it could be either electron correlation effects or structural instabilities. At low temperatures vanadium dioxide exhibits a monoclinic crystal structure and at high temperatures it exhibits a tetragonal crystal structure, shown in Figure 1.4. In the monoclinic phase the vanadium atoms arrange into pairs, but in the tetragonal phase (referred to as rutile) all V–V distances are equal and the symmetry is tetragonal [14].

One of the limitations of VO_2's application in smart window technologies is the cracking of the film after a certain number of switching transitions. VO_2 nanoparticles and thin films are much better than bulk VO_2 because they can survive the stress generated during repeated cycles of phase transition and their transition temperature can be modified to near room temperature by doping [15, 16]. Because of its optical and electrical properties, together with its transition temperature that is near room temperature, VO_2 thin films and nanoparticles have many technological applications which include thermochromic coatings, optical and holographic storage, fiber-optical switching devices, laser scanners, missile training systems and ultra-fast optical switching devices [16].

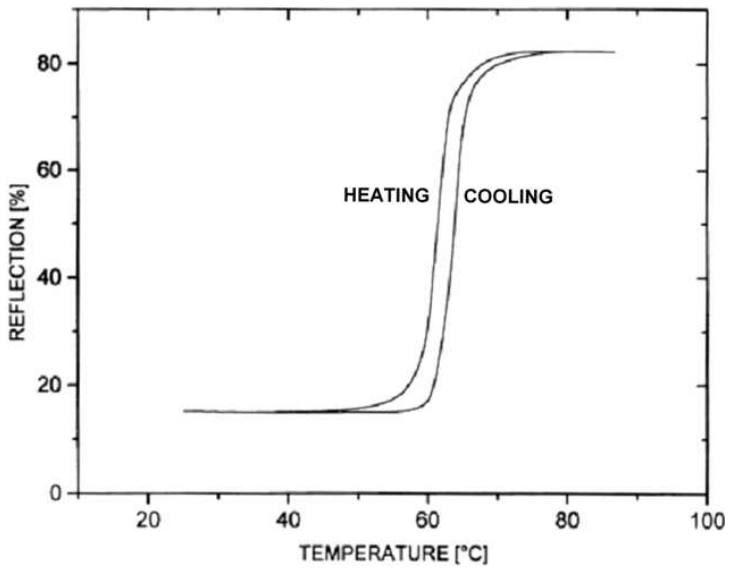

Figure 1.3: Measured hysteresis curves during the insulator–metal transition of a thin VO_2 film optical reflectivity at a wavelength of 2.0 µm [13].

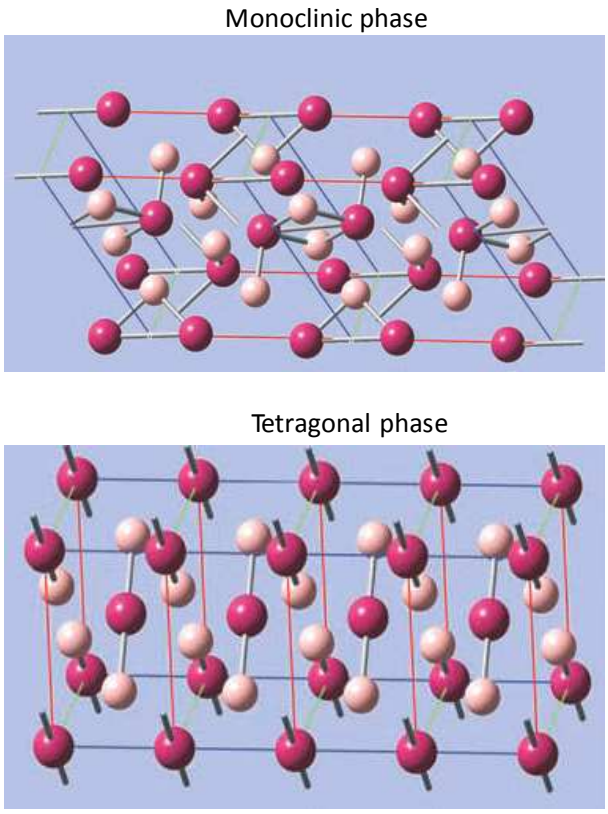

Figure 1.4: Crystal structure of the low-temperature monoclinic phase and the high temperature tetragonal phase [14].

VO_2 nanoparticles can be formed in a fused silica host by implanting vanadium and oxygen ions in proper proportions and annealing in an argon atmosphere at 1000^{o}C, the nanoparticles showed a hysteresis width of up to 50^{o}C [16]. A group has produced VO_2 nanobelts using the laser pyrolysis technique; these nanobelts showed a hysteresis width of 83^{o}C [17] which is the highest ever reported hysteresis for VO_2. The previously highest reported hysteresis was of the order of 15^{o}C [16]. The enhancement was due to the small particles produced as it is believed that the smaller the particles the bigger the hysteresis width.

X-ray diffraction (XRD) has also been used to estimate particle size and to identify the vanadium phases. Figure 1.5 illustrates a typical room temperature x-ray scan obtained after annealing the V- and O-implanted specimen at high temperature for 30 min. In addition to the broad structure due to the amorphous SiO_2 substrate, Bragg reflections at 2θ=27.81° and 57.67° were observed corresponding respectively to the (011) and (022) reflections of the VO_2 monoclinic phase [16]. VO_2 (B) has XRD characteristic peaks at 2θ =15º, 29º and 45º.

The VO_2 particle size can be estimated by using the Scherrer formula

$$\langle D \rangle = \frac{0.9\lambda}{\beta \cos\theta}, \qquad (1.1)$$

where λ is the x-ray wavelength used in the XRD study, β is the line broadening at half the maximum intensity (FWHM) in radians and θ is the Bragg angle. The Scherrer formula relates the crystallite size in the sample to the peak width of the spectrum.

Raman spectroscopy has been used to identify the vanadium oxide phases. Figure 1.6 shows a typical Raman spectrum of VO_2. The spectrum is dominated by two sharp peaks at 192 cm^{-1} and 224 cm^{-1} and a broader peak at 614 cm^{-1} which belong to the B_g Raman modes [18]. The Raman modes at 224, 305 and 614 cm^{-1} correspond to the A_g modes of VO_2 [19]. It can also be noted that the B_g modes are generally stronger than the A_g modes.

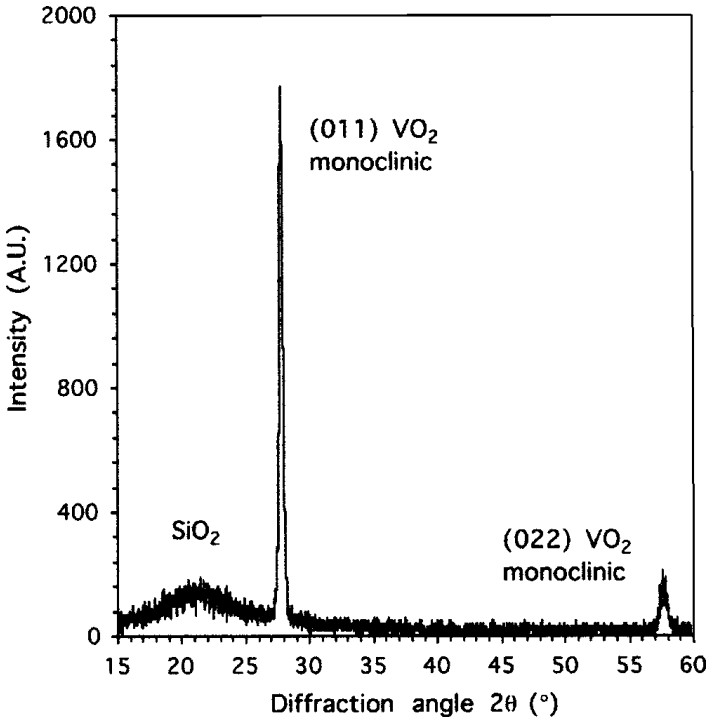

Figure1.5: XRD patterns of VO_2 thin films. The broad XRD peak in the region 15^o-25^o is due the amorphous glass substrate [16].

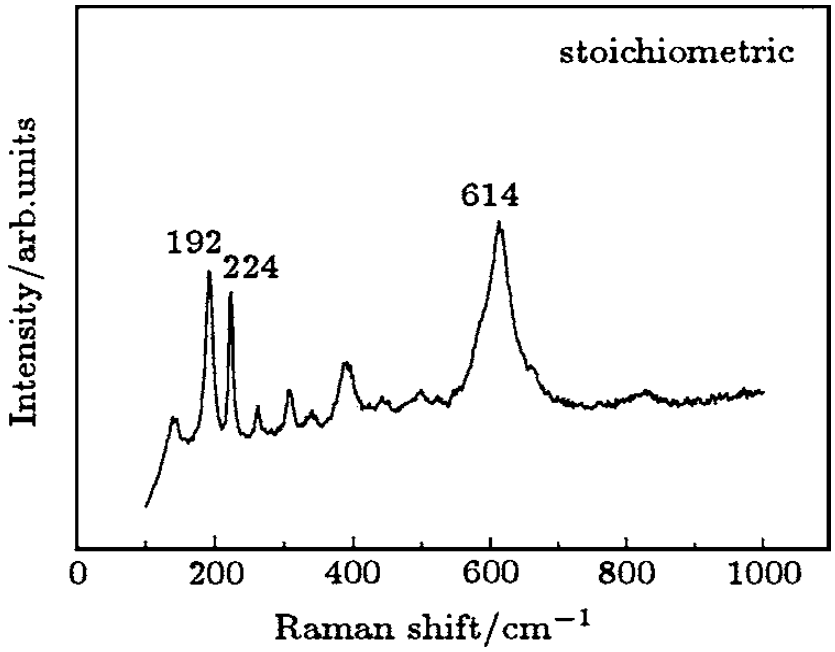

Figure1.6: A Raman spectrum of a VO_2 thin film [18].

1.3 Laser Pyrolysis (LP)

VO_2 thin films and nanoparticles have been produced using various methods such as sputtering [20], sol-gel [21], evaporation [22], pulsed laser deposition [23], chemical vapour deposition [24], ion implantation [16] and laser pyrolysis [17]. Laser pyrolysis has major advantages in producing thin films and nanoparticles over the mentioned techniques. Some of the advantages include the production of pure products since there is no contact with the chamber walls, the interaction volume is well defined, there is control of the nucleation rate, the growth rate and exposure times [25]. Although laser pyrolysis has many advantages it also has a few drawbacks. One of the drawbacks is imposed by the precursors: the desired elements must be present in vapor phase and at least one reactant should contain an infrared absorption band for the coupling of the energy with the laser beam [26].

The first laser pyrolysis experiment was performed by Bachmann between 1974 and 1975 [27]. Figure 1.7 shows the trend of publications since 1974. The graph shows a steady increase in the number of publications from 1974 to 2010. This suggests that LP is gaining popularity as a method of producing nanostructures. As mentioned earlier, in 1974 Bachmann's group were the first to synthesis BCl_3 particles using a CO_2 laser, this process was named differently then. In 1977 Bowden's group proposed a model for laser-induced photo-chemical reaction. This model was designed based on a pulsed CO_2 laser. In 1981 Haggerty's group introduced the LP parameters such as flow rates. They were also the first group to

synthesis Si nano-powder using this technique. The graph also shows some of the materials that have been synthesized using the LP method.

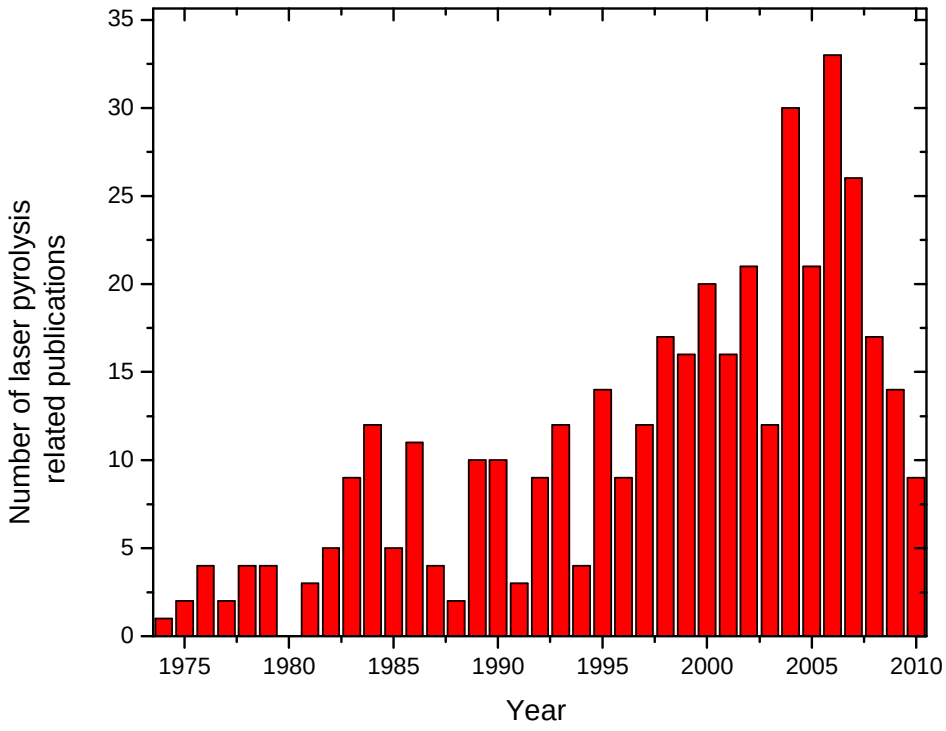

Figure 1.7: Annual publications on laser pyrolysis from 1974 to mid 2010.

Most of the laser pyrolysis experiments are performed using a CO_2 laser. This technique has been used to synthesis nano-crystals [28], nano-wires [17, 29], nano-belts [17], nano-powders [30] and nanoparticles [31].

In addition to the CO_2 laser, there are other parameters that play a major role in attaining the desired particle size. These parameters are flow rates, pressure in the chamber and the nature of the carrier gases [32]. It has been shown that C_2H_4 gas is excited by IR radiation which transfers its vibrational energy to the precursor

molecules to make them dissociated, the mean diameter of the particles formed was 5 nm [33]. A group has recently reported the synthesis of iron ultrafine nanoparticles by laser pyrolysis and by using a coagulation model based on the aerosol theory [34]. They derived an equation describing an average particle size with time given by

$$d(t) = \left(\frac{6N_0V_0}{\pi} \right)^{\frac{1}{3}} \left[N_0^{-\frac{5}{6}} + \frac{5}{6} kt \right]^{\frac{2}{5}}, \tag{1.1}$$

where N_0 is the initial number of atoms in the gas per unit volume, V_0 is their volume, t is the time of evolution of the average size and k is given by

$$k = 6^{\frac{2}{3}} \left[\frac{4kT}{\rho} \right]^{\frac{1}{2}} \left(\frac{N_0V_0}{\pi} \right)^{\frac{1}{6}}, \tag{1.2}$$

where T is the average coagulation temperature [34].

Another important parameter in laser pyrolysis is the measurement of temperature at the reaction zone (where the laser beam interacts with the aerosols). The method of measurement has to be non-contact so there is no interference with the reaction. It has been shown that temperature measurements of a reaction zone can be performed using coherent anti-Stokes Raman spectroscopy (CARS) [35]. The dynamics of the reactions are not yet fully understood and more has to be done on this subject. The question on how to measure the temperature of the reaction is still open.

1.4 Multiphoton Infrared Excitation

Multiphoton processes can be induced by intense radiation, and become extremely efficient if one or more resonance conditions are satisfied by the molecular energy levels. Vibrational levels are more or less equally spaced for the lowest levels of excitation, and so with infrared radiation of appropriate wavelength, multiphoton absorption can become highly significant.

Firstly, the case of multiphoton infrared absorption by a diatomic molecule is considered, as there is only one vibrational frequency. The appropriate energy levels are shown in Figure 1.8, where the arrows represent the absorption of infrared photons with the same frequency. Note that spacing between adjacent levels in the vibrational state starts off fairly constant, but thereafter diminishes at an increasing rate. Also note that each vibrational level contains more closely spaced rotational levels. Because each of these levels has an associated linewidth, this results in a quasi-continuum of states, which is represented by the shaded region in Figure 1.8. Eventually, there is a limit at which point there is no longer any restoring force as the two atoms move apart, leading to dissociation [36].

The process of multiphoton absorption displays different characteristics over different regions of the energy scale, and the regions are commonly referred to as region I, II, and III as illustrated in Figure 1.8. In region I, the vibrational levels are widely spaced, and the spacing is greater than the overall absorption bandwidth. However, the spacing is non-uniform, and so the photon energy soon gets out of step, allowing for muliphoton processes. For example, in Figure 1.8,

the transitions $v = 0 \rightarrow 1$, $1 \rightarrow 2$, $2 \rightarrow 3$, $3 \rightarrow 4$ and $4 \rightarrow 5$ all require energies close to that of a single photon and lying within the overall bandwidth [36]. These transitions therefore all take place by the process of single-photon absorption. However, the energy required for the $5 \rightarrow 6$ transition, is sufficiently different, that it lies outside the bandwidth and cannot take place by absorption of one photon. Excitation can still proceed up to the $v = 10$ level, as indicated by direct $5 \rightarrow 10$ transition involving four-photon absorption [36]. This is the main characteristic of region I that such concerted multiphoton processes take place on the way up the vibrational ladder.

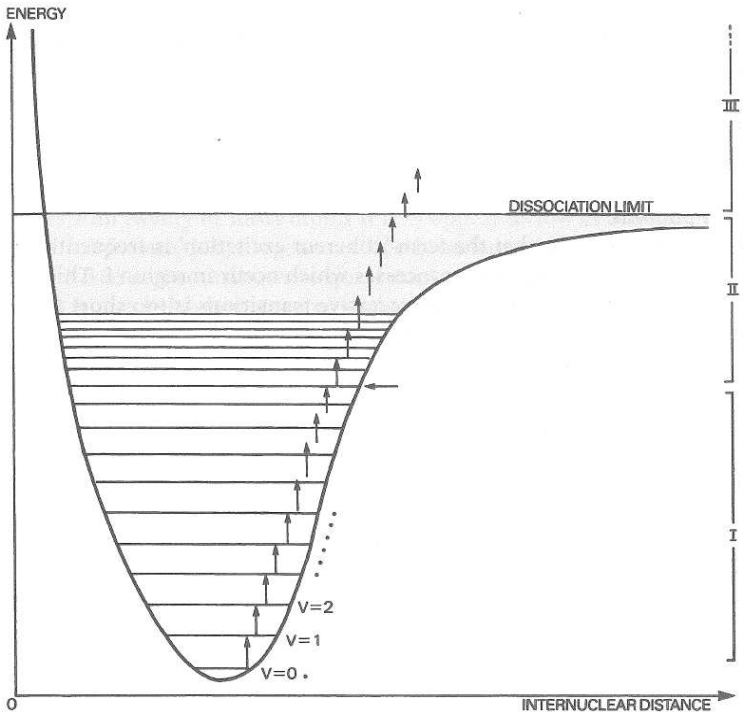

Figure 1.8: Energy levels and transitions involved in the multiphoton infrared dissociation of a diatomic molecule [36].

Region II is characterized by a quasi-continuum behaviour resulting from the fact that vibrational energy level spacing has become less than the bandwidth. Successive photons can be absorbed here in a series of energetically allowed single-photon transitions. Since energy conservation is satisfied at every step, the molecule can at each point exist for a finite lifetime before absorbing the next photon. Therefore, excitation through this region does not necessitate the enormously large photon flux which might have first appeared. Once the level of excitation has reached the dissociation threshold, a true energy level continuum is encountered, and more photons can be absorbed in the short time before the atoms separate. The region where more photons can be absorbed in the short time before the atoms separate is known as region III behaviour [36].

Chapter 2: Theory of VO_2 transition

2.1 Metal-insulator transitions

2.1.1 Introduction

Interest in the metal-insulator transition arose in Bristol at a conference in 1937. de Boer and Verwey pointed out that nickel oxide should be metallic according to Bloch-Wilson model because the eight electrons of the Ni^{+2} ion would only partly fill the d band [37]. Peierls, in the discussion, said he thought that must have been due to correlation and he gave a convincing description of how this could occur [37]. In the 1950s Mott described a metal-insulator transition by imagining a crystalline array of hydrogen-like atoms with lattice constant a that could be varied [37]. The example of nickel oxide suggested that for large values of a the material would be insulating, while the example for monovalent metals like sodium showed that for small values it would be metallic [37]. The question was, at what value of a would a metal-insulator transition would occur? A value was obtained, namely

$$n^{1/3} a_H \cong 0.2 , \qquad (2.1)$$

where n is the number of centres per unit volume and a_H the hydrogen radius. This formula was applied to heavily doped semiconductors successfully. Moreover, the prediction was made that the number of free carriers must change discontinuously at the transition. This is because a small number of electrons and

holes attracting one another with a coulomb force must form neutral pairs; only if they are strongly screened by other carriers [37].

2.1.2 The free electron model of metals

Suppose all valence electrons are free, and do not interact with other electrons and with the atoms of the lattice. The electron can be described by a wave function

$$\psi = Ae^{i\vec{k}\bullet\vec{r}}, \tag{2.2}$$

which is identical to an electron in free space. The vector k describes the momentum of the electron and unlike the electrons in free space the values that k can have are quantized. In a cube of side $L\left(\Omega = L^3\right)$, if we write

$$\vec{k}\bullet\vec{r} = k_1 x + k_2 y + k_3 z, \tag{2.3}$$

then k_1, k_2, k_3 can have the values

$$k_1 = \frac{2\pi l_1}{L},\ k_2 = \frac{2\pi l_2}{L},\ k_3 = \frac{2\pi l_3}{L}, \tag{2.4}$$

where l_1, l_2, l_3 can be positive or negative integers. In k-space the number of states in a volume element $d^3k\left(= \mathrm{d}k_x \mathrm{d}k_y \mathrm{d}k_z\right)$ is

$$\frac{\Omega \mathrm{d}^3 k}{8\pi^3}, \tag{2.5}$$

and the number of states for which k, the modulus of $\vec{k}$, lies in the range k to $k + \mathrm{d}k$ is

$$4\pi\Omega k^2 \mathrm{d}k \Big/ 8\pi^3 \ . \tag{2.6}$$

The density of states per unit energy range and per unit volume, for a given spin direction, is written $N(E)$, where E is the energy. From (2.6), setting $\Omega = 1\,\mathrm{cm}^3$, we get

$$N(E)\mathrm{d}E = 4\pi k^2 \mathrm{d}k \Big/ 8\pi^3 \ , \tag{2.7}$$

since the relationship between E and k is given by

$$E = \frac{\hbar^2 k^2}{2m}, \tag{2.8}$$

Substituting for k we find

$$N(E) = \frac{1}{4\pi^2}\left(\frac{2m}{\hbar^2}\right)^{3/2} E^{1/2} . \tag{2.9}$$

The free electron model came from combining it with Fermi- Dirac statistics which states that the number of electrons in each orbital state cannot be greater than two. At absolute zero of all temperatures all states are occupied up to a maximum energy E_F given by

$$2\int^{E_F} N(E)\mathrm{d}E = n, \tag{2.10}$$

where n is the number of electrons per unit volume. Substituting (2.9) into (2.10) gives

$$\frac{\left(\frac{2mE_F}{\hbar^2}\right)^{3/2}}{3\pi^2} = n\,, \tag{2.11}$$

where E_F is called the Fermi energy, and in most metals its magnitude is that of several volts.

The kinetic energy of the electron gas increases as the temperature increased: some energy levels are occupied which were vacant at absolute zero, and some levels are vacant which were occupied at absolute zero [38].

The situation is illustrated by Figure 2.1, where plotted curves are of the function

$$f(E) = \frac{1}{e^{(E-\mu)/k_BT} + 1}. \tag{2.12}$$

This is the Fermi-Dirac distribution function: it gives the probability that a state at energy E will be occupied in an ideal electron gas in thermal equilibrium. The quantity μ is called the chemical potential and at absolute zero μ is equal to the Fermi energy [38].

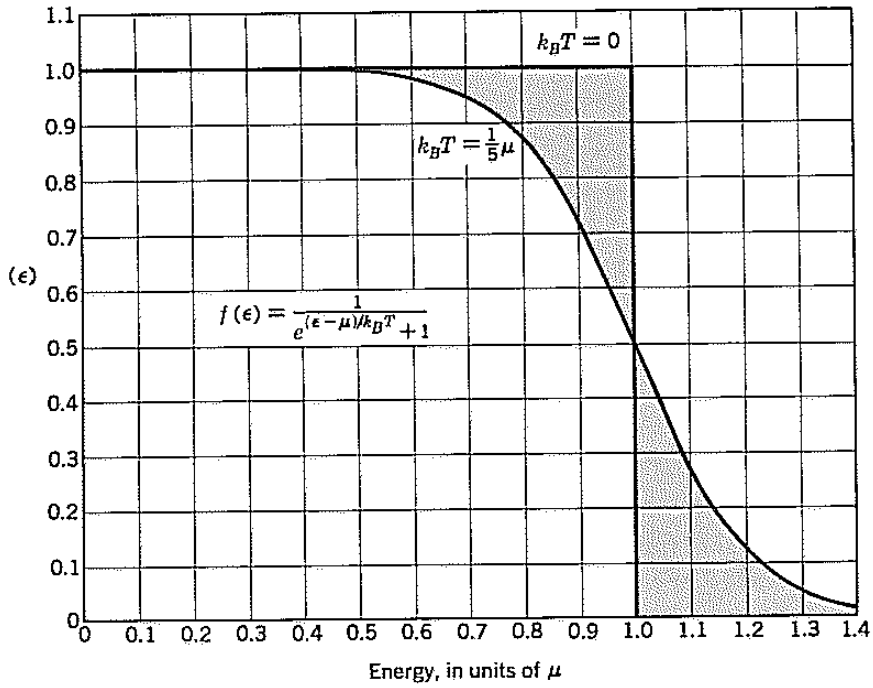

Figure 2.1: Plot of the Fermi-Dirac distribution function $f(E)$ versus E/μ, for zero temperature and for a temperature $k_BT = 1/5\mu$. The value of $f(E)$ gives the fraction of levels at a given energy which are occupied when the system is in thermal equilibrium [38].

2.1.3 Energy bands

Electrons in crystals are arranged in energy bands, Figure 2.2, separated by regions in energy for which no electron energy states are allowed; such forbidden regions are called energy gaps or band gaps. If the number of electrons in the crystal is such that allowed energy bands either filled or empty, then no electrons can move in an electric field and the crystal will behave as an insulator. If all bands are entirely filled, except for one or two bands which are slightly filled or

slightly empty then the crystal is said to be a semiconductor. If one or more bands are partly filled, 10 to 90 percent filled, the crystal will act as a metal.

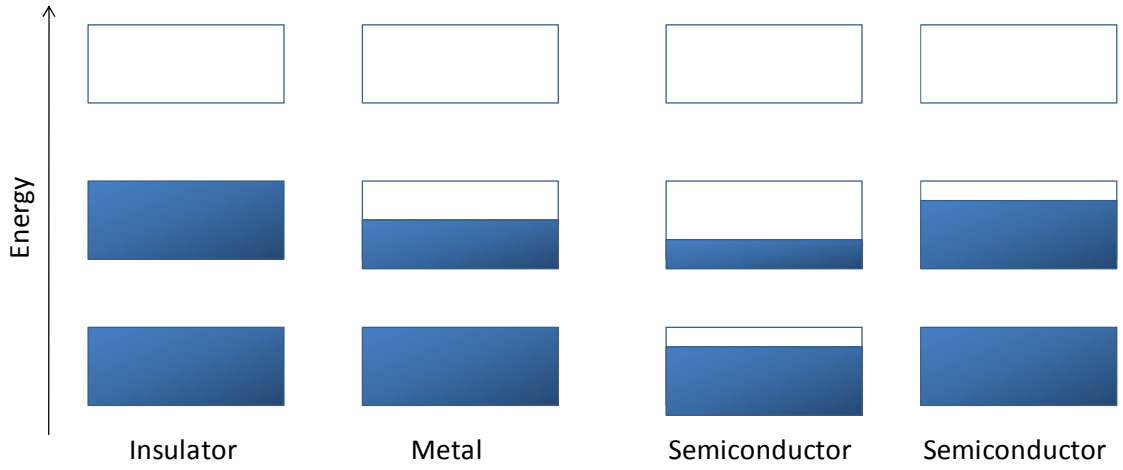

Figure 2.2: Schematic electron occupancy of allowed energy bands for an insulator, metal, and two semiconductors. The vertical extent of the boxes indicates the allowed energy regions; the shaded areas indicate the regions filled with electrons.

On the free electron model the allowed energy values are distributed continuously from zero to infinity. It has been shown that

$$E_k = \frac{\hbar^2}{2m}(k_x^2 + k_y^2 + k_z^2), \tag{2.13}$$

where E_k is the energy eigenvalue of the state with wavevector k; here $E_k = 0$ for $k = 0$. For boundary conditions over a cube of side L,

$$k_x, k_y, k_z = 0; \qquad \pm\frac{2\pi}{L}; \pm\frac{4\pi}{L}; ..... \tag{2.14}$$

The free electron wavefunctions are of the form

$$\psi_k(r) = (1/V)^{1/2} e^{ik\cdot r} \ , \qquad (2.15)$$

where $V = L^3$ is the volume; they represent running waves and carry momentum $p = \hbar k$.

Bragg reflection is a characteristic feature of wave propagation in crystals. It occurs also for electron waves in crystals and leads to energy gaps. That is, there may arise substantial regions of energy in which wave-like solutions of the Schrödinger equation do not exist, as in Figure 2.3. These energy gaps are of decisive significance in determining whether a solid is an insulator or a conductor.

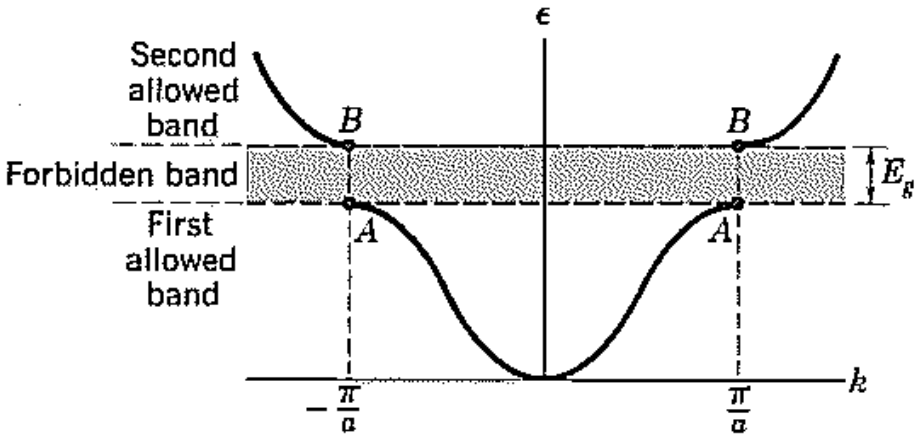

Figure 2.3: Plot of energy versus wavevector for an electron in a monatomic linear lattice constant a . The energy gap E_g shown is associated with the first Bragg reflection at $k = \pm\pi/a$; other gaps are found at $\pm n\pi/a$, for integral values of n [38].

Figure 2.4 (a) shows an insulator with an indirect gap. The gap may be decreased by some external parameters as in Figure 2.4 (b). The system will become

metallic; there will be a condensed gas of electrons in the conduction band and of holes in the valence band and the Fermi energy (E_F) will be as shown.

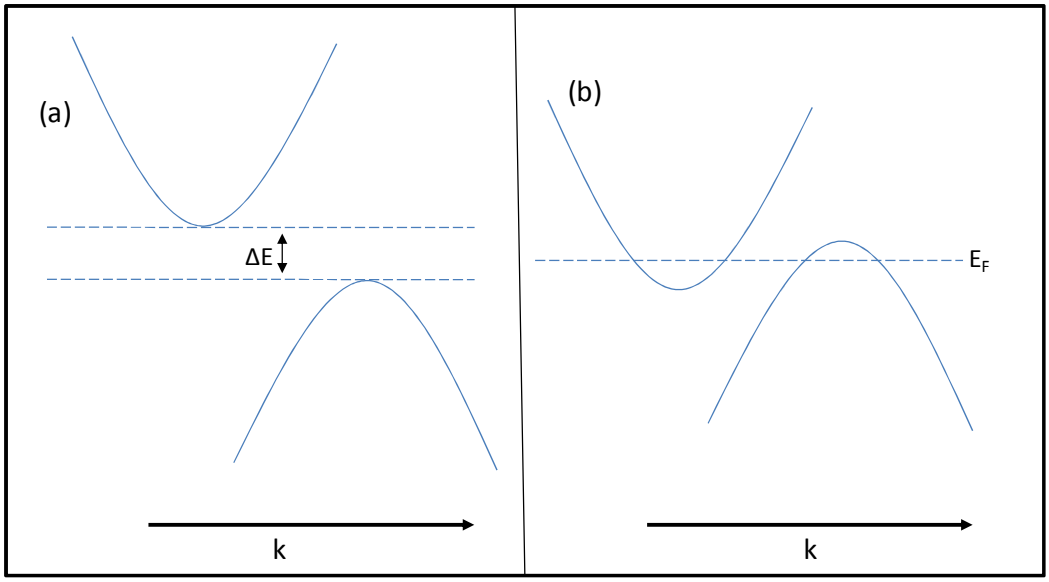

Figure 2.4: Metal-insulator transition of band-crossing type. $E(k)$ is plotted against k in the (a) insulating and (b) metallic states.

2.1.4 Metal-insulator transitions in compounds

Materials such as VO_2,V_2O_3 and NiS whether pure or alloyed with other oxides show transitions from insulator to metallic behaviour as the temperature is raised, or under pressure or with varying composition in systems such as $(V_{1-x}Ti_x)_2O_3$ [37]. When a transition from an insulator to a metal takes place with increasing temperature, the driving force must be related to the entropy in the metallic phase [37]. This can be due to two causes: (1) softer phonons modes in the high-temperature phase. This probably contributes a major part of the entropy in VO_2 and (2) the entropy of the electron gas [39].

2.1.5 Metal-insulator transitions in metal-oxides VO_2

The transition in vanadium dioxide (VO_2) from a low-temperature semiconductor to a metallic phase at 340 K was first observed by Morin in 1959 [40]. In the high-temperature phase VO_2 has a rutile structure, the structure of metallic VO_2 is based on a simple tetragonal lattice with space group $P4_2/mnm\left(D_{4h}^{14}\right)$, shown in Figure 2.5. The metal atoms are located at the Wyckoff positions $(2a):(0,0,0),\left(\frac{1}{2},\frac{1}{2},\frac{1}{2}\right)$ and the oxygen atoms occupy the positions $(4f):\pm(u,u,0),\pm\left(\frac{1}{2}+u,\frac{1}{2}-u,\frac{1}{2}\right)$. The rutile structure can be visualized in terms of a body-centred tetragonal lattice formed by the metal atoms, where each metal atom is surrounded by an oxygen octahedron [41].

Between 1971 and 1973 J. B. Goodenough proposed a n electronic band structure VO_2 as a merger of the separate electronic band configurations of V^{4+} anion and O^{2-} cation. These band structures were analyzed in both the room-temperature monoclinic phase and the high temperature tetragonal phase of VO_2. In the monoclinic phase, the V-V pairing splits the narrow d_{ll} band in two possibly due to electron correlations. The semiconducting character of the monoclinic phase requires that the π^* bands be raised above the E_F and the formation of V-V pairs stabilize V-V homo-polar orbitals below the E_F level. The band structure of the metallic phase of VO_2 is shown in Figure 2.6. The t_{ll} band contains two electrons per V atom, so that, whether the two bands overlap or not, metallic conduction is to be expected [39].

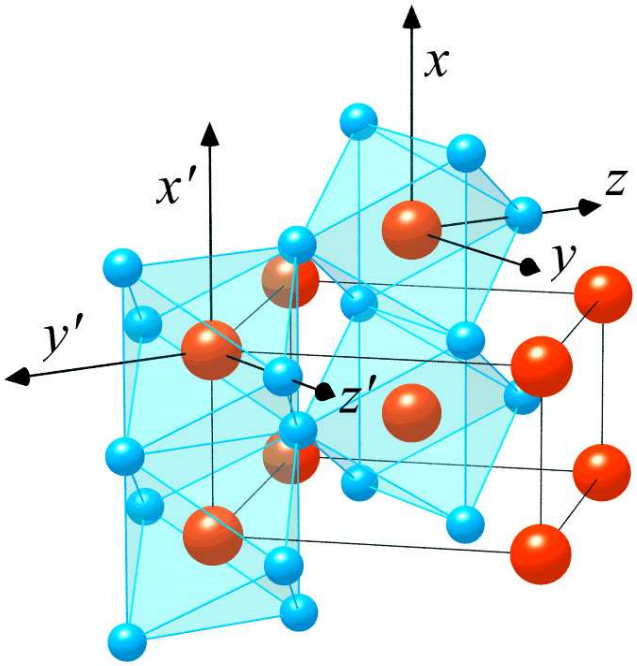

Figure 2.5: The rutile structure. Large and small spheres denote metal and ligand atoms, respectively [41].

Figure 2.6: Band structure of VO_2 as suggested by Goodenough (1971).

Below 340 K there is a distortion from the tetragonal structure to monoclinic symmetry. The monoclinic structure of VO_2 is characterized by a simple monoclinic lattice with space group $P2_1/C\left(C_{2h}^5\right)$ [41], shown in Figure 2.7. The metal atoms as well as the two different types of oxygen atoms occupy the general

Wyckoff position $(4e):\pm(x,y,z),\pm\left(x,\frac{1}{2}-y,\frac{1}{2}+z\right)$ [41]. In the low-temperature phase VO_2 is a semiconductor and discontinuities as great as 10^4 have been observed in the conductivity at the transition. The low-temperature phase is not antiferromagnetic so the pairing of the V ions splits the t_{II} band into two sub-bands, each capable of accommodating one electron per cation [39].

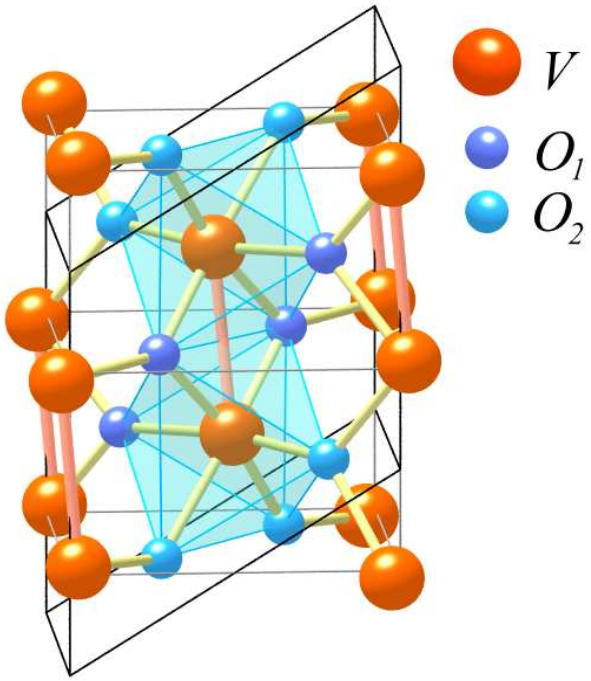

Figure 2.7: Monoclinic structure of VO_2. Large and small spheres denote metal and ligand atoms, respectively [41].

Many models have been developed to explain the transition of VO_2. Paquet and Leroux-Hugon presented a model of the VO_2 phase transition which included both the electron-electron and electron-lattice interactions. This accounted for the presence of the two d bands (π^* and $d_{//}$) overlapping at the Fermi level of the metallic phase [41]. The electron-electron interactions were explained using the

functional-integral treatment of the Hubbard Hamilton and the electron-lattice interactions were treated by choosing the centre-of-gravity and the shape of the d -bands so that they depended on the lattice distortion [42].

On the other hand, Vikhnin et al also proposed a VO_2 phase transition by assuming that the phase transition is governed by charge transfer mechanism [42]. This mechanism has two competing phenomena-(1) the negative dielectric parameter ε due to coulomb repulsion between the electron density (at the oxygen site) and the hole density (at the vanadium site) leading to electron-hole pair instability and (2) the electron-hole pair (exciton) effect due to the exciton's interaction with the lattice leading to attraction and electron-hole stability charge transfer [42].

Despite several models being proposed, ranging from Peierls-to Mott-Hubbard-type scenarios the origin of the phase transition is still not fully understood [41]. These models stress, to a different degree, the role of lattice instabilities, electron-phonon interaction and electron-electron correlations. So far, neither of these approaches has been successful in explaining the broad range of phenomena occurring in vanadium dioxide [40]. So far a general, complete and accepted picture of the physics of this material has not yet been developed [41].

2.1.6 Electrical properties of VO_2

In the semiconducting phase, the exponential behaviour of the resistivity can be explained by the thermal generation of free carriers. Because of the many

electronic defects inherent with the synthesis of the oxide, it is often treated as an extrinsic material in which the conductivity $\sigma = \frac{1}{\rho}$ is directly proportional to the number of majority carriers. In the case of electrons (n-type semiconductor) [43],

$$\sigma = nq\mu_n \tag{2.16}$$

where n is the concentration of electrons in the conduction band, q is the charge of an electron and μ is the carrier mobility. The temperature dependence is dominated by the one of the carrier concentration;

$$n(T) = N_c \exp\left(\frac{E_f - E_c}{kT}\right) \tag{2.17}$$

where N_c is the effective density of states, E_f is the energy of the Fermi level, E_c is the lowest energy available in the conduction band and k is the Boltzmann constant. The expression for the conductivity is defined by introducing a pre-exponential factor σ_0 and activation energy E_a,

$$\sigma(T) = \sigma_0 \exp\left(-\frac{E_a}{kT}\right). \tag{2.18}$$

Chapter 3: Beam assessment from a CO_2 laser

3.1 Introduction

A laser is a device that amplifiers light and produces a high-intensity beam that most often has a very pure frequency or wavelength. The word LASER is an acronym for Light Amplification by Stimulated Emission of Radiation. Albert Einstein formed the theoretical foundation for the laser in 1917 using Max Planck's law of radiation. In 1953 Charles H. Towns and his co-workers produced the first microwave amplifier device operating on the principles of a laser. In 1960 Theodore Maiman of Hughes Research Laboratories produced the first laser using a ruby crystal as the amplifier and a flash lamp as the energy source. In 1961 Ali Javan and his co-workers constructed the first gas laser using a mixture of helium and neon gases. The first carbon dioxide (CO_2) laser was invented by Kumar Patel of Bell Labs in 1964. This laser is of interest because of its high power output thus giving it applications in the industry for cutting and welding. It is has also been used in the synthesis of nanostructured materials, shown in Figure 1.5, this is our primary interest.

3.1.1 Gaussian beam propagation

Gaussian beams have interesting properties, one of them being that if the beam has a Gaussian transverse profile at one location then it will have a Gaussian transverse profile at all other locations, unless optical elements introduce a

distortion that is [44]. A simple Gaussian beam has a transverse distribution of the radial intensity described by

$$I = I_0 e^{-2r^2/w^2} \tag{3.1}$$

where I_0 is the maximum intensity and w is the beam radius. The Gaussian beam minimum waist w_0 occurs either at a point of focus after having passed the lens or in the region between two mirrors, such as within the optical resonator [44]. The beam then expands and diverges from that location. The beam radius at a distance of z from the minimum beam waist is described as

$$w(z) = w_0\left(1+\frac{z^2}{z_0^2}\right)^{1/2}, \tag{3.2}$$

where z_0 is the Rayleigh range and is given by

$$z_0 = \frac{\pi w_0^2}{\lambda}, \tag{3.3}$$

where λ is the wavelength of the beam. The Rayleigh range is described as the distance from the beam waist before the beam begins to diverge significantly (or the distance which the beam propagates from the waist before the area of the beam doubles). Figure 3.1 illustrates the propagation of the Gaussian beam and the position of the Rayleigh range.

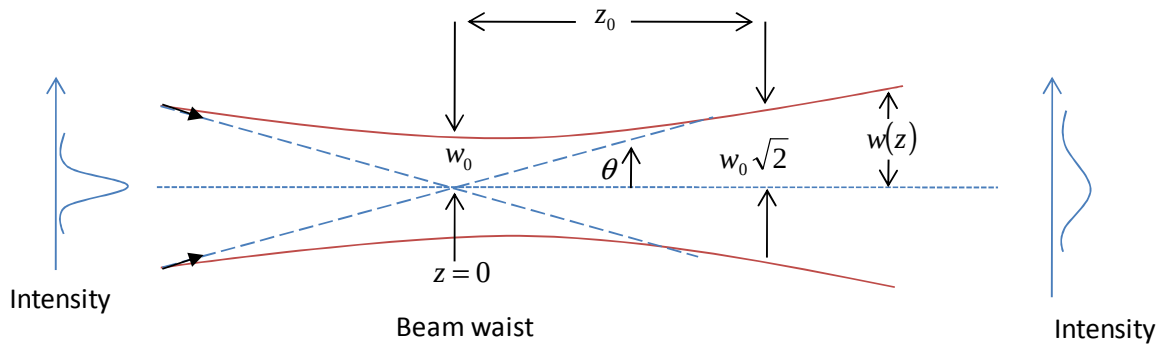

Figure 3.1: Variation of the spot size $w(z)$ of a Gaussian beam.

3.1.2 Gaussian beam focusing

Before we discuss Gaussian beam focusing, let us briefly look at how the beam size expands in the far field. It is known that the beam size expands linearly with distance as shown in Figure 3.2. The spot size $w(z)$ for the field amplitude in the far field for a Gaussian beam coming from a waist with spot size w_0 is given by

$$w(z) \approx \frac{w_0 z}{z_R} = \frac{\lambda z}{\pi w_0}, \qquad (z >> z_R) \tag{3.4}$$

which gives the relation

$$w(\infty) \times w_0 = \frac{\lambda z}{\pi}, \tag{3.5}$$

connecting the spot sizes at the waist and in the far field [45].

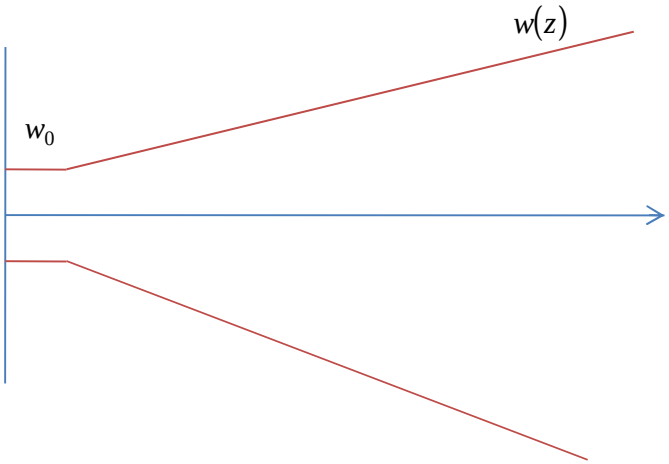

Figure 3.2: A Gaussian beam spreads with a constant diffraction angle in the far field.

Gaussian beam focusing is the opposite of Gaussian beam propagation in the far field. Instead of the beam spreading out it is focused to a spot. Gaussian beam focusing is important in many applications such as recording data on optical videodisks and drilling holes in razor blades [45]. A collimated Gaussian beam focused by a lens of focal length f is shown in Figure 3.3. The focusing lens can be viewed as being the far field at $z \approx f$. The relationship as in equation (3.5) can be written as

$$w(z) \times w_0 = \frac{\lambda f}{\pi} . \qquad (3.6)$$

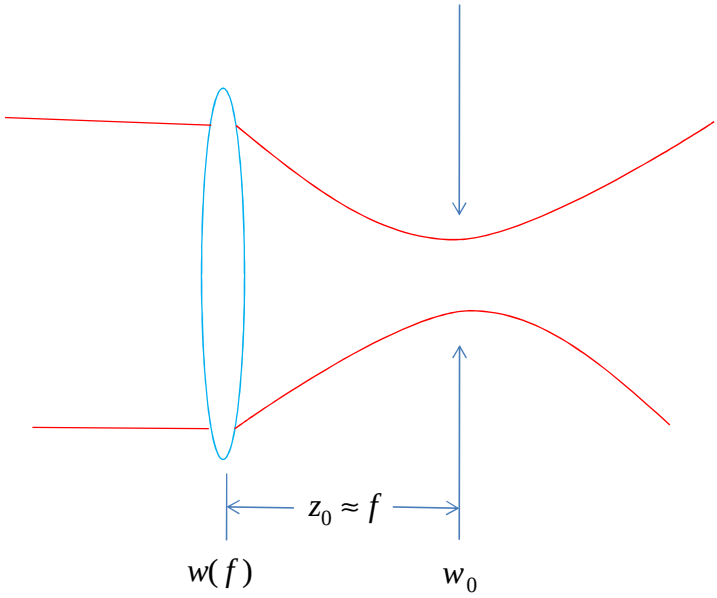

Figure 3.3: Focusing of a Gaussian beam to a small spot size.

3.2 Carbon Dioxide (CO_2) Laser

The carbon dioxide laser falls under the category of molecular gas lasers. These are the middle and far infrared lasers which occur on rotational-vibrational transitions or pure rotational transition [44]. Carbon dioxide lasers are one of the most powerful and efficient lasers available. They operate in the mid-infrared region on rotational-vibrational transition in the 9 µm and 11 µm wavelength region. Both pulsed and continuous wave (cw) laser output occurs in several different types of gas discharge configurations in a mixture of carbon dioxide, nitrogen, and helium gases [44]. The most useful CO_2 laser is a cw version producing power in the kilowatts range. Some applications of the CO_2 lasers are in the industry of cutting and welding, and in the medical uses such as laser surgery, skin resurfacing and dermabrasion.

The electronic energy levels and the quantization of vibrational and rotational states of the CO_2 molecules are of major importance to the CO_2 laser. The CO_2 molecule is a tri-atomic, linear and symmetric molecule consisting of two oxygen atoms covalently bonded to a central carbon atom, O-C-O. The individual atoms are bound by a force which acts like that of the force due to a spring - Hooke's law. The molecules can rotate and spin because they are in a gaseous state. They have two stretching vibrational modes and a bending mode: the vibrational symmetric mode is were two oxygen two atoms vibrate against each other; the vibrational asymmetric mode is were the two oxygen atoms oscillate against the carbon atom; and the bending mode is where the carbon moves out the molecular axis thus bending the molecule, Figure 3.4 illustrates these different types of modes. The first number is the excitation number of the symmetric mode, the second number is the excitation number of the bending mode and the third number is the excitation number of the asymmetric mode.

Figure 3.5 illustrates the vibrational energy levels showing the energy transfer from the Nitrogen (N_2) molecule to the CO_2 molecule that is relevant for laser action. Nitrogen is excited with energy from the discharge (produced by a high potential difference across the N_2, CO_2 and Helium (He) gas mixture) and the first vibrational energy level of that molecule provides a pump energy level that matches the upper lasing level in the CO_2 molecule (001,asymmetric mode) [46]. The energy of the N_2 is transferred to the CO_2 molecules and results in populating

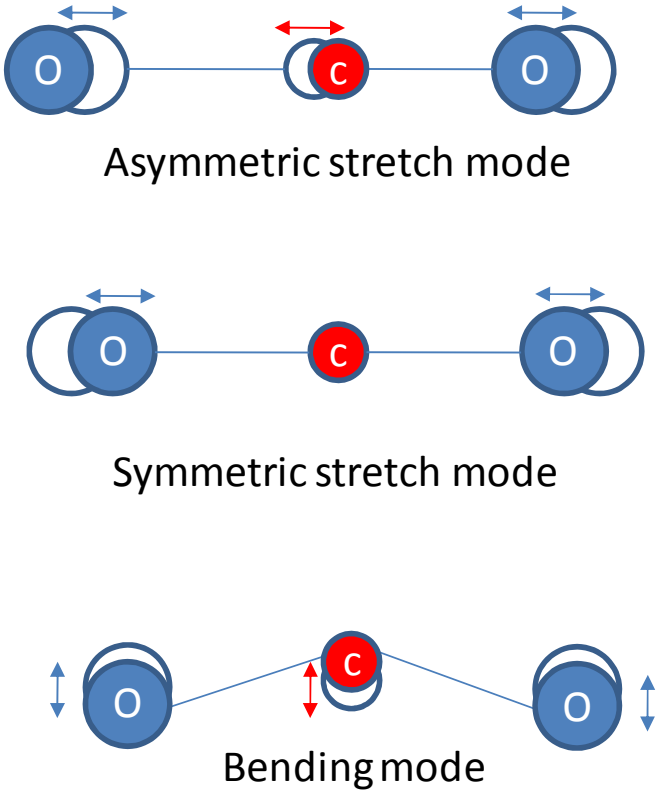

Figure 3.4: A schematic diagram illustrating the vibrational modes of a CO_2 molecule.

their upper levels. The transition between two vibrational energy levels in the CO_2 molecule results in lasing. The CO_2 molecule (001) can de-excite in two ways: it can decay to a lower energy level related to the symmetric stretch of the molecule (100) and it can decay to a lower energy level related to the bending mode of the molecule (020). The (001) molecule emits at 10.6 µm wavelength and the (020) molecule emits at 9.6 µm wavelength. The (100) and (020) molecule modes can decay further to lower energy levels emitting photons of different wavelengths until the ground state is reached. The Helium gas helps the population inversion

process to occur once the electrons get to the ground state. The gas also serves to conduct heat from the discharge to the walls of the tube. Water is used to cool the CO_2 laser but it is also used to reduce the thermal population of the lower energy levels close to the ground state. Figure 3.6 shows a picture of a typical CO_2 laser.

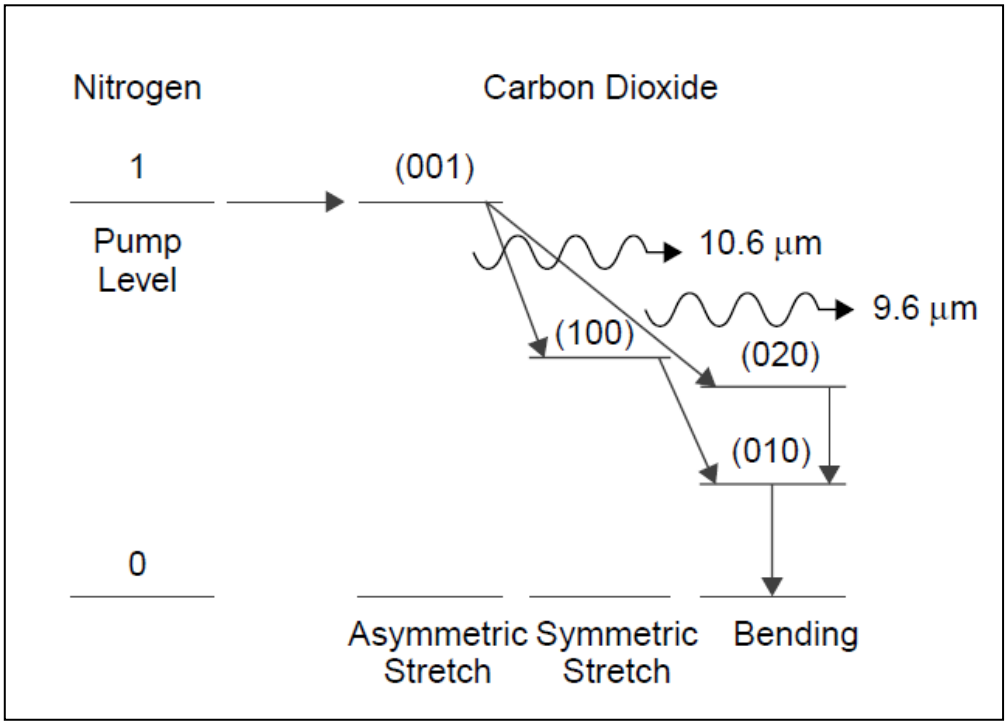

Figure 3.5: A schematic diagram of energy levels in the CO_2 laser.

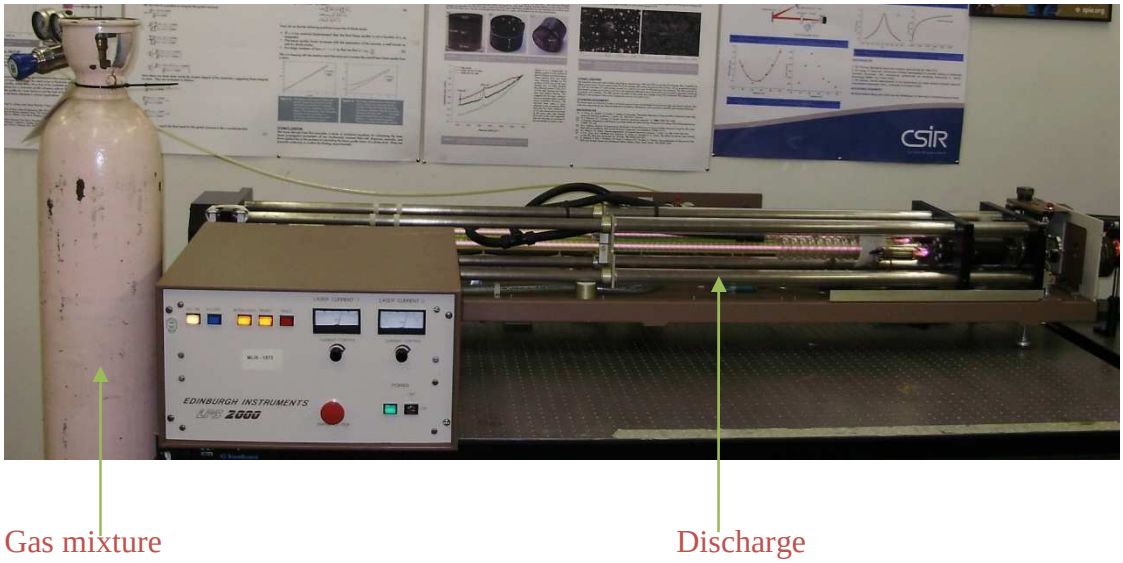

Figure 3.6: A picture of an Edinburgh instruments cw CO_2 laser (model PL-6).

3.3 Experimental procedure

There are several techniques used for beam-profiling: the scanning slit method, the scanning knife edge method, the scanning pinhole method, the scanning Ronchi ruling and the (charge-coupled device) CCD camera method. In this study the scanning slit and the CCD camera were the preferred methods. Figure 3.7 (a) and (b) illustrates the optical layout of the scanning slit and CCD camera methods. A continuous wave (cw) CO_2 laser from Edinburgh instruments (Model PL-6) was characterised. The Helium-Neon (HeNe) laser beam was aligned co-linearly with the CO_2 laser beam since the CO_2 laser beam emits light in the infrared region which is invisible. A spectrum analyzer (Optical Engineering Inc, model 16A) was used to measure the wavelength of the laser at varying laser powers. A polarisation based attenuator was used to allow power variability, as well as to monitor the polarisation state of the laser output.

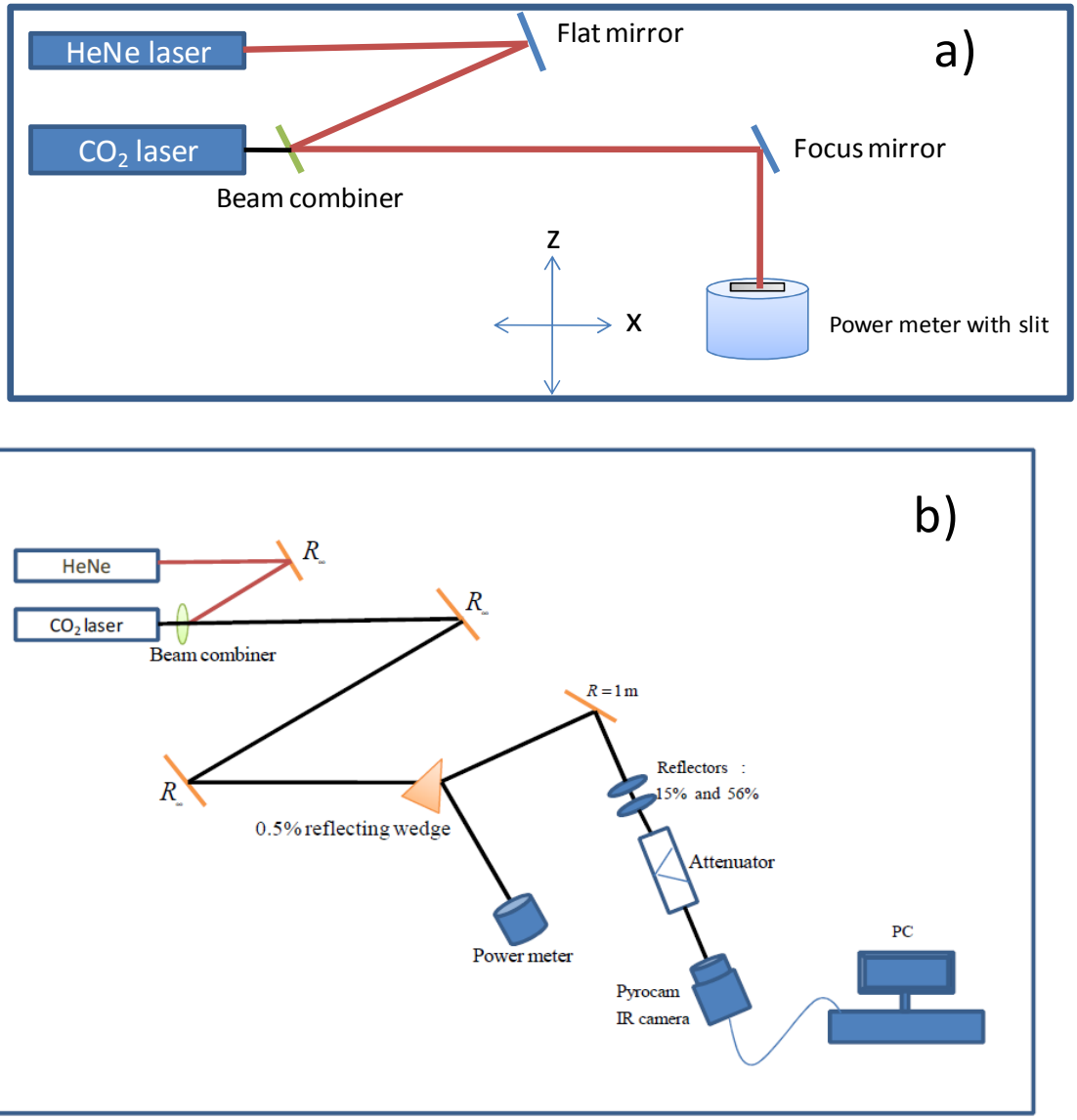

Figure 3.7: A schematic layout of (a) the scanning slit method to determine the beam parameters and (b) the CCD camera method to determine the beam parameters.

3.3.1 Laser output and wavelength

A laser enables the selection of the desired wavelength from any of the rotational lines of the CO_2 molecule by means of a diffraction grating in the CO_2 laser cavity. By changing the angle of the grating it was possible to tune the wavelength

of the laser beam from one rotational line to another. This is done by adjusting the micrometer attached to the grating.

3.3.2 Laser beam quality and size

As mentioned earlier, two methods were employed to determine the beam quality and size (beam parameters) of the laser beam. In both methods the beam parameters were determined by focusing the beam with a 1 m radius of curvature mirror. The scanning slit method involves a narrow finite slit (0.1 mm) passed between a laser beam and measuring the power transmitted at each point of the slit. Provided the slit width is known, it is not necessary for it to be less than 1/10 or 1/20 of the beam width [47]. The scanning slit method measurements results in a two dimensional profile in one dimension. The slit scans were performed at several propagation distances, z , from the focusing mirror and the resulting beam profiles were recorded. The beam resembled a Gaussian profile and the values for the beam radius $w(z)$ were determined by fitting a Gaussian function

$$y = y_0 + \frac{A}{w\sqrt{\pi/2}} \exp\left[\frac{-2(x - x_0)}{w^2}\right], \tag{2.7}$$

to the experimental data, where y_0 is the baseline offset, A is the total area under the curve from the baseline, x_0 is the centre of the peak, and w is the width of the Gaussian. The CCD camera method was also used to determine the beam parameters. The CCD camera method provides a more accurate and rapid two dimensional profile information [45].

3.3.3 Laser beam attenuation

As mentioned before, attenuator is used to allow power variability, as well as to monitor the polarisation state of the laser. In this experiment we determined the polarization of the laser beam by rotating the laser beam attenuator and measuring the beam power transmitted through as a function of the rotational angle. From the data we determined which fraction was horizontally polarized and which fraction was vertically polarized. Figure 3.8 shows a schematic diagram of the attenuator. The attenuator is made up of two Zinc Selenide (ZnSe) windows mounted at Brewster's angle.

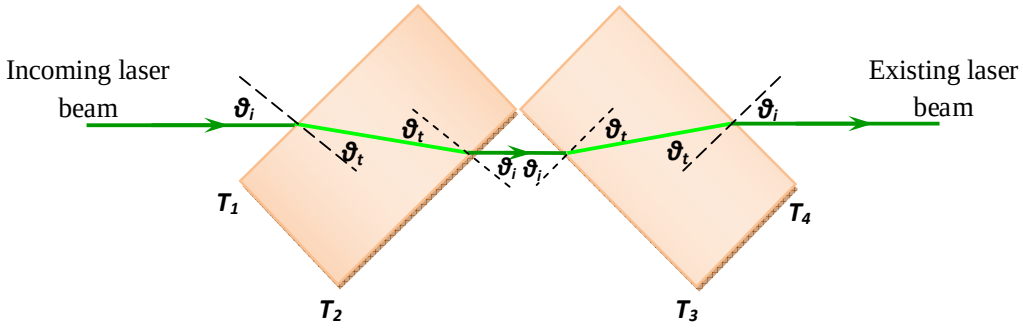

Figure 3.8: A schematic diagram of the propagation of a laser beam through two ZnSe windows at Brewster's angle.

The incident beam propagates through the air, with a refractive index n_1, to the first surface T_1 of the ZnSe window with a refractive index n_2. The laser beam strikes the surface T_1 at an incident angle θ_i and is refracted by an angle θ_t in the ZnSe window. The beam then strikes the surface T_2 of the ZnSe windows at the angle θ_t and leaves at an angle θ_i. The beam then propagates from the surface T_2 at an angle θ_i to surface T_3, it is then refracted by an angle θ_t. The beam finally

leaves the windows at an angle θ_i. The windows are fixed at Brewster's angle and as a consequence the angle of incidence equals Brewster's angle. The beam strikes the windows at Brewster's angle right through the rotation which means that only the plane of the light is affected. By varying the angle of the plane of the light we vary the transmission of the laser beam.

Fresnel equations of reflection and refraction describe the behaviour of light when moving between media of different refractive indices. Assuming that there is no absorption in the windows the reflectance (R) and transmittance (T) is given by

$$R + T = 1, \tag{3.8}$$

and the transmittance for parallel and perpendicular light are given by

$$T_{//} = 1 - R_{//}, \tag{3.9}$$

$$T_{\perp} = 1 - R_{\perp}, \tag{3.10}$$

where the intensity coefficients $R_{//}$ and $R_{\perp}$ of the windows for the parallel and perpendicular polarized light to the plane of incidence are given by

$$R_{//} = \left[\frac{\tan(\theta_t - \theta_i)}{\tan(\theta_t + \theta_i)}\right]^2, \tag{3.11}$$

$$R_{\perp} = \left[\frac{\sin(\theta_t - \theta_i)}{\sin(\theta_t + \theta_i)}\right]^2. \tag{3.12}$$

The total transmittance of the system is the multiple of the transmittance T_1 through T_4 of the window surface of the attenuator, this is given by

$$T_{T//} = T_{1//}T_{2//}T_{3//}T_{4//}, \tag{3.13}$$

and

$$T_{T\perp} = T_{1\perp}T_{2\perp}T_{3\perp}T_{4\perp}. \tag{3.14}$$

We now consider the incident beam on the attenuator window to be propagating in the z-direction and the polarization transmission axis of the attenuator to be in the y-direction. Assuming the polarisation transmission axis makes an angle α with the beam then the beam is partially polarized in the direction of the polarization transmission axis, Figure 3.9. The electric field vector (E) of the laser beam can be separated into components as it passes through the windows. We get the parallel component $E_{//}$ and the perpendicular component $E_{\perp}$ where

$$E_{//} = E_0 \cos\alpha, \tag{3.15}$$

and

$$E_{\perp} = E_0 \sin\alpha, \tag{3.16}$$

where E_0 is the amplitude of the electric field.

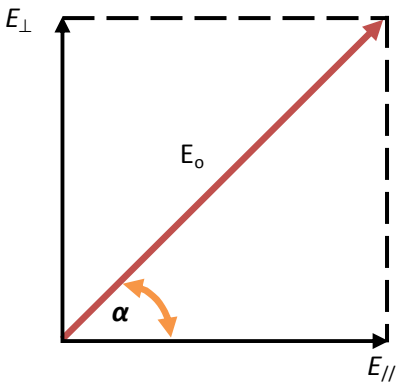

Figure 3.9: Polarization is composed of a parallel and perpendicular component.

Intensity is proportional to the square of the electric field and the intensities are given by

$$I_{//} = T_{T//} \times E^2 = T_{T//} \times E_0^2 \cos^2 \alpha, \tag{3.17}$$

and

$$I_{\perp} = T_{T\perp} \times E^2 = T_{T\perp} \times E_0^2 \sin^2 \alpha. \tag{3.18}$$

The total transmittance intensity of the Brewster windows is calculated by summing the two intensities of the parallel (3.17) and the perpendicular (3.18) polarization, this is given by

$$I = I_{//} + I_{\perp}. \tag{3.19}$$

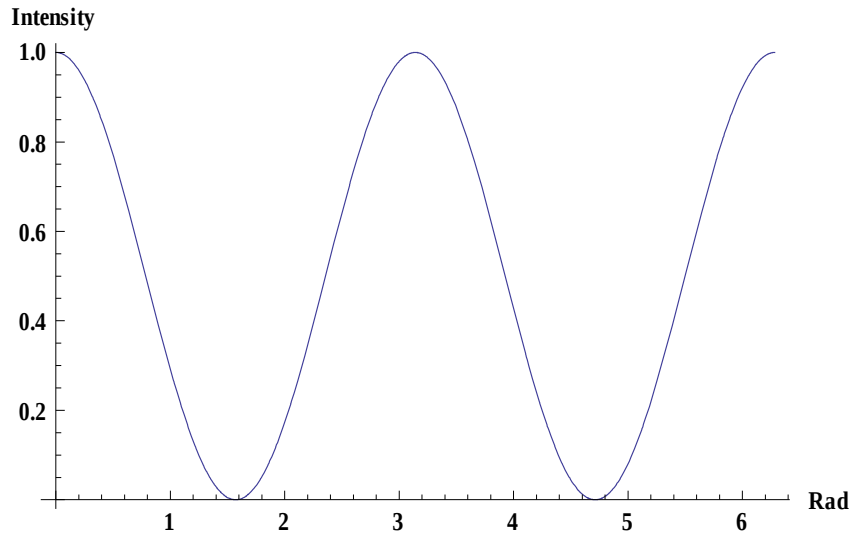

Figure 3.10: Total transmittance intensity of the parallel polarized light through ZnSe the windows.

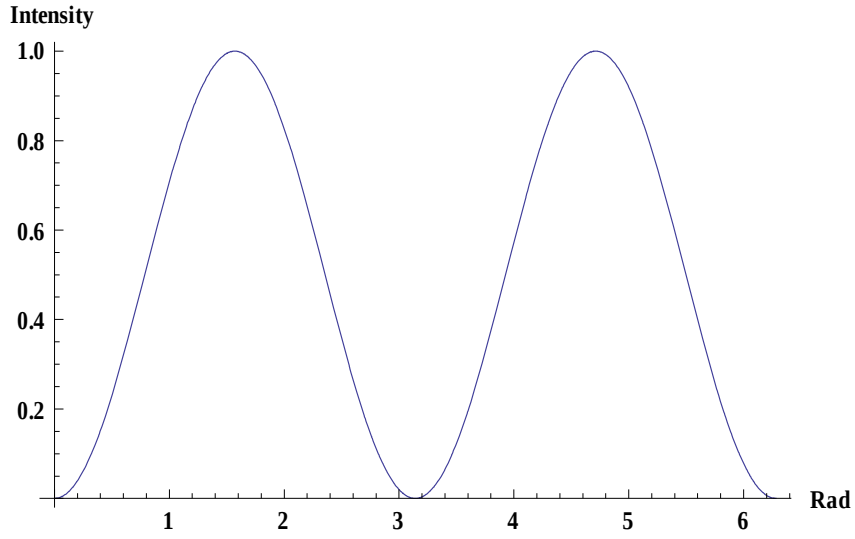

Figure 3.11: Total transmittance intensity of the perpendicularl polarized light through the ZnSe windows.

Figures 3.10 and 3.11 shows the theoretical curves of the parallel (3.12) and perpendicular (3.13) polarized light respectively.

3.4 Results and discussion

The results of the Gaussian profiles from the scanning slit method at different propagation distances are shown in Figure 3.12. Figure 3.12 shows the experimental data (black) with the Gaussian fits (red), plotted as a function of slit position. The results indicated that the beam has a Gaussian profile at propagation distances less than 55 cm. After the focus point of 55 cm, the beam has a different profile which means that equation 3.7 cannot be used to fit the experimental data. This means that the beam parameters cannot be determined using this method. We now use the CCD camera method to determine the beam parameters.

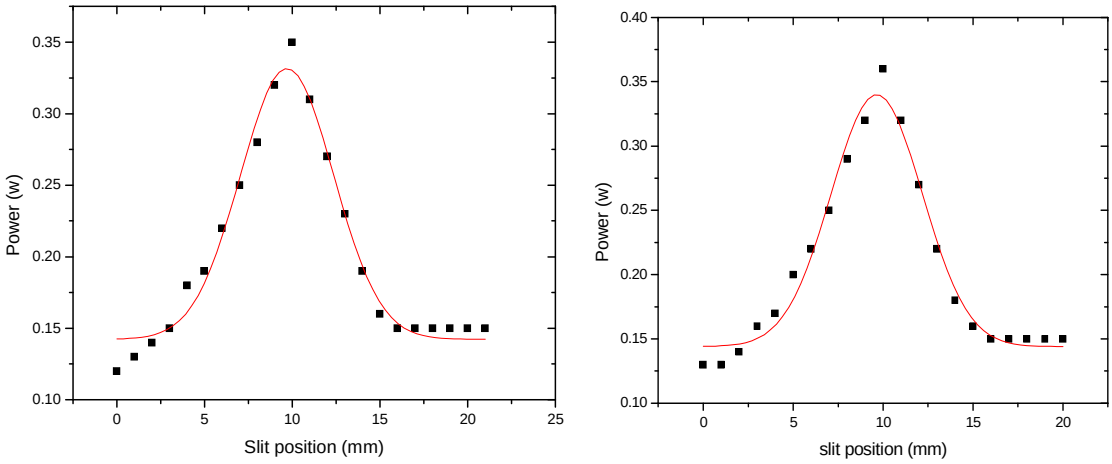

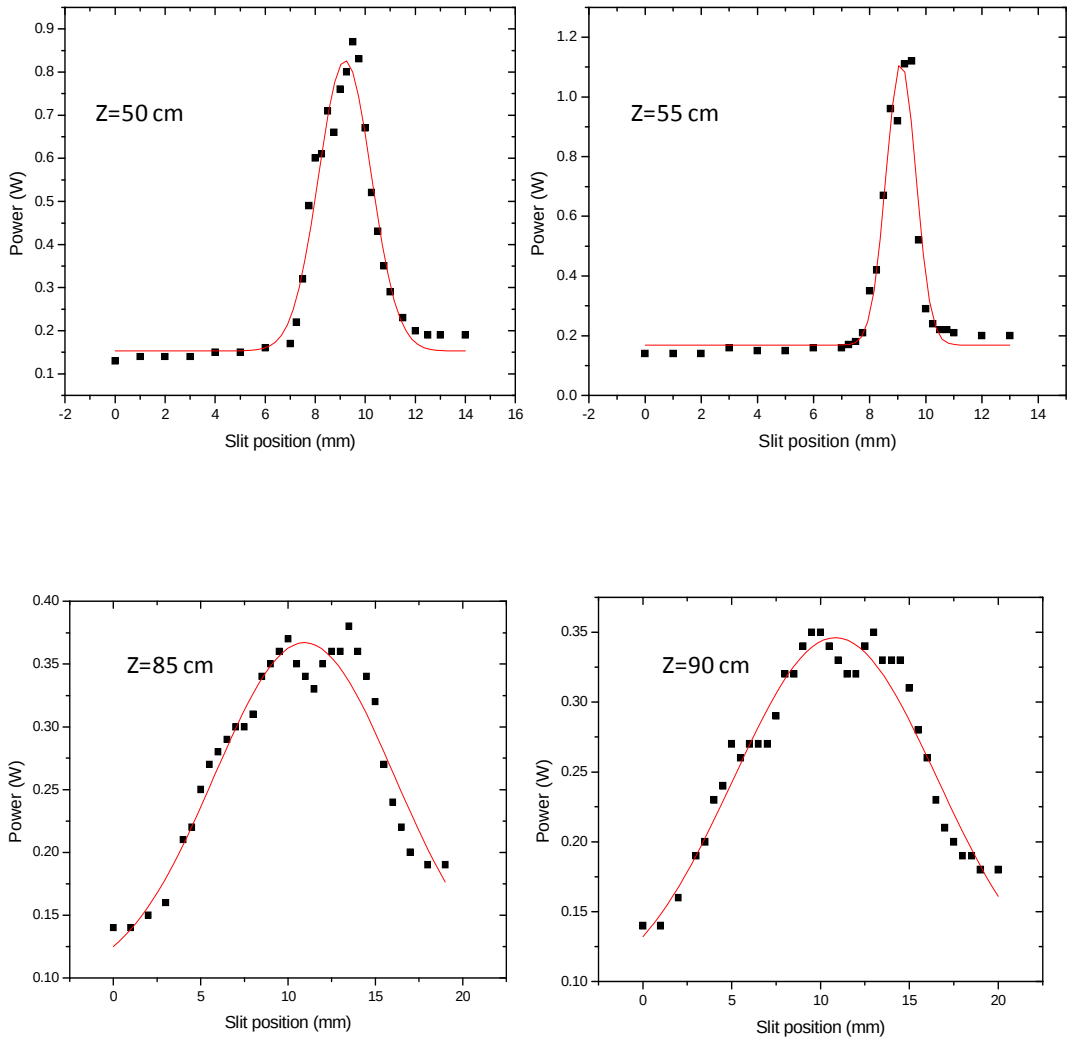

Figure 3.12: Some of the Gaussian beam profiles measured at various propagating distances after the focusing mirror.

A Pyrocam^{TM} III pyroelectric array camera is used in imaging the laser beam profile at different propagation distances. Figure 3.13 shows the images of the laser beam at different propagation distances.

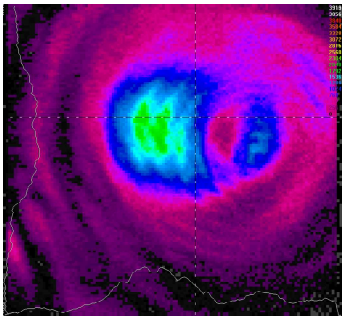

15 cm

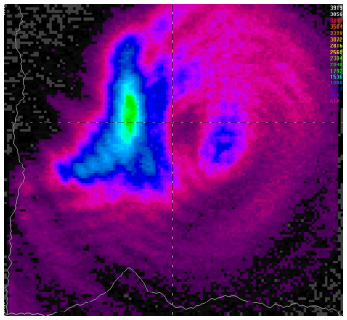

20 cm

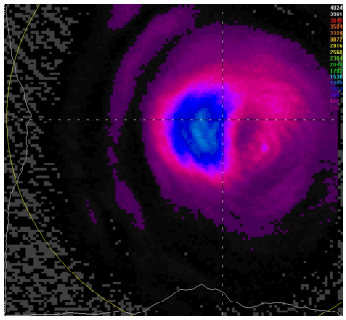

25 cm

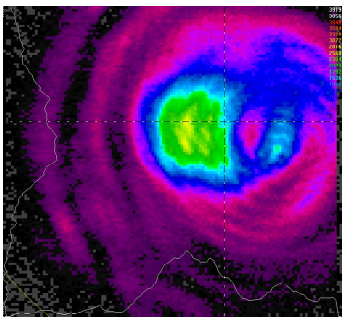

30 cm

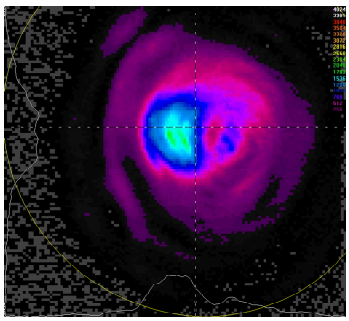

35 cm

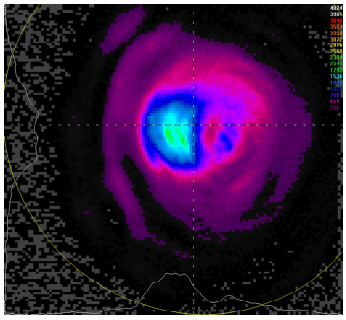

40 cm

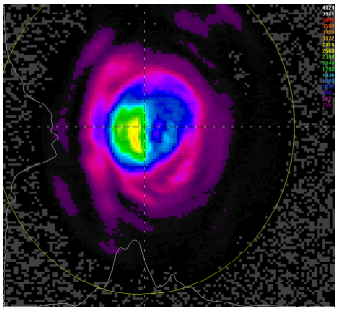

45 cm

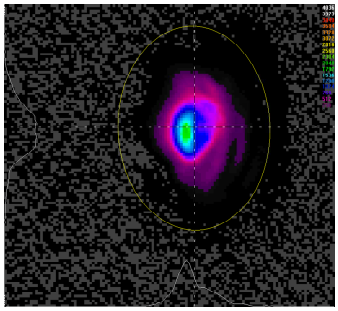

50 cm

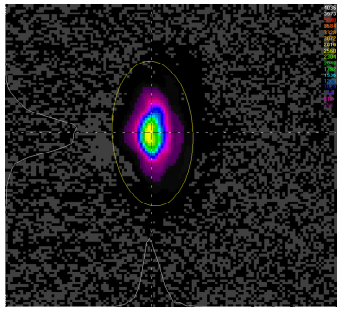

55 cm

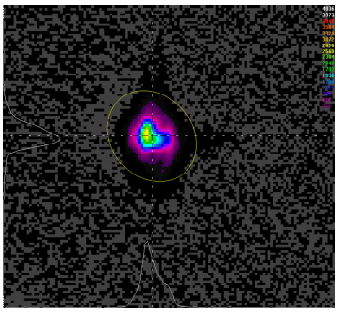

60 cm

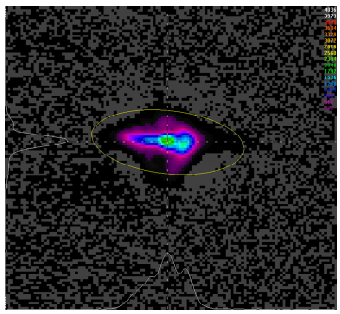

65 cm

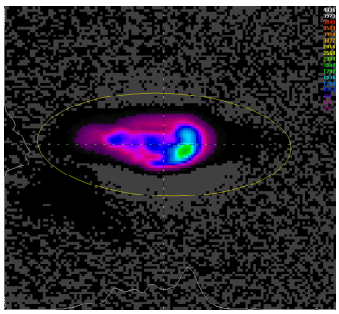

75 cm

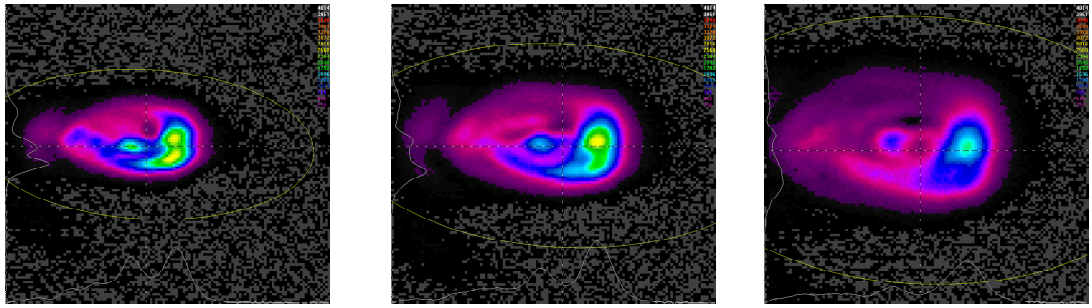

Figure 3.13: Images of beam size at different propagation distances from the focusing mirror.

The beam radius $w(z)$ values are extracted from each of these images and are squared. A plot against the distance at which the imaging is performed is done. A quadratic polynomial (red) is fitted to the experimental data (black) shown in Figure 3.14. The quadratic polynomial given by

$$w(z) = 2.736\times10^{-4} z^2 - 0.302z + 84.164 \qquad (3.20)$$

is extracted from the fit. The beam waist $w(z)$, the position of the waist z_0 and the beam quality factor M^2 are determined by comparing an expansion of the beam propagation equation (3.2) to the polynomial fit equation (3.20). The beam parameters are given in Table 1.

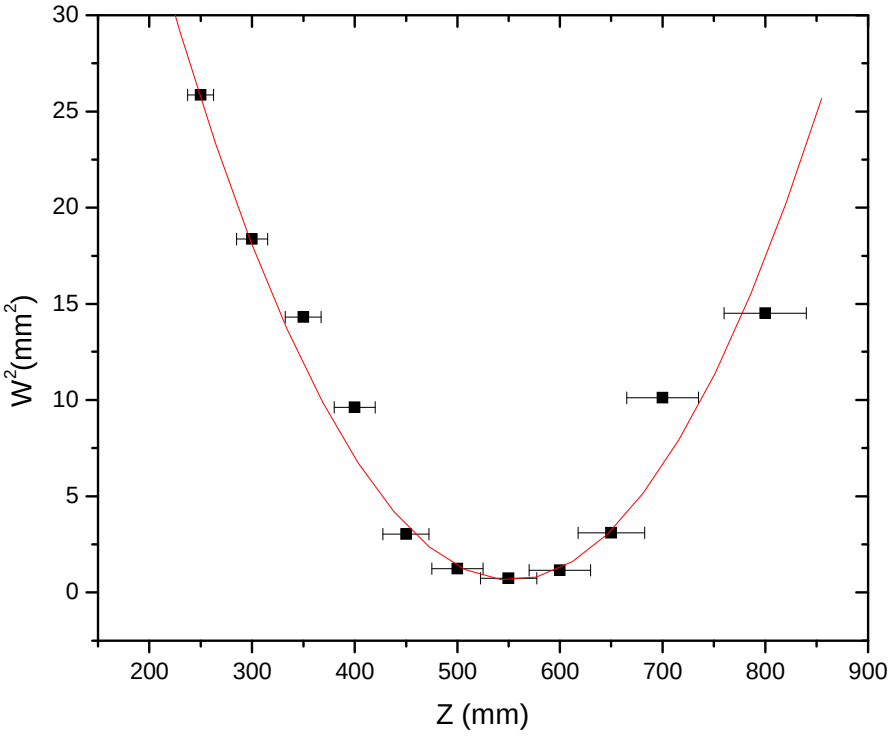

Figure 3.14: A plot of distance (z) versus the beam radius squared (W^2).

Table 3.1: Beam parameter measurements of a beam focused by a focal length of $f = 50cm$.

Beam Parameter	Measurement
Beam waist (w_0)	1.05±0.14 mm
Beam quality (M^2)	4.93
Position of beam waist (z_0)	616±43.1 mm

A beam quality of 4.93 means that the beam profile is not a perfect Gaussian, a perfect Gaussian profile has a beam quality of 1.

The results for the laser output power measured at each rotational line of the CO_2 molecule is plotted against the wavelength, Figure 3.15 illustrates. The wavelength range of the spectral line is between 9.19 µm to 10.84 µm and the highest laser power output is 60.5 W at the 10P (22) line corresponding to a wavelength of 10.6 µm. The 9R, 9P, 10R and 10P are the emission bands of the CO_2 laser.

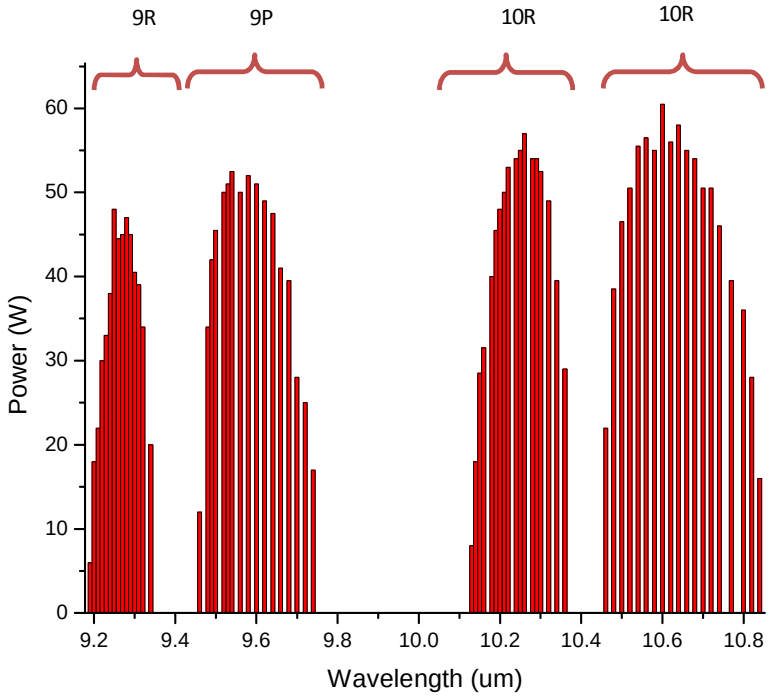

Figure 3.15: A plot of the laser power output versus wavelength.

As mentioned earlier in section 3.3.3, the polarization of the laser beam can be determined by rotating the laser beam attenuator and measuring the beam power

transmitted. Figure 3.16 shows the results of the laser power transmission as a function of the angle of the attenuator.

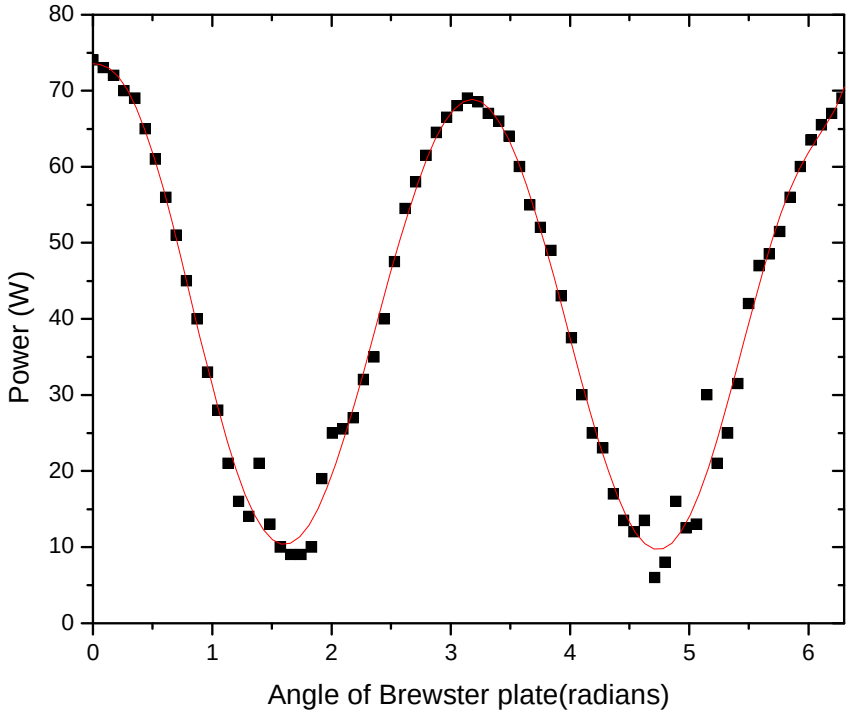

Figure 3.16: Experimental data for the power transmission as a function of the angle of the attenuator.

The result in Figure 3.16 show that maximum power transmittance is found at angles 0^o, 180^o and 360^o and the minimum power transmission is found at about 92^o and 270^o. The laser powers are the sum of the parallel and perpendicular polarization, equation (3.19). From calculations we find the maximum transmittance to be 73 and find the minimum transmittance to be 9, so the total transmittance is 82. The percentage for parallel polarization is 89% and the percentage for perpendicular polarization is 11%.

Chapter 4: Characterisation Techniques: Principles and Instrumentation

4.1 Introduction

It is all good and well to synthesize thin films but it is futile if the composition, the structure and properties of the material are not known. Characterisation techniques help in determining the chemical and physical properties of the material. In this chapter the different characterisation techniques, how they work and what information they provide us about the material, are discussed.

4.1.1 Reaction chamber

A reaction chamber, shown in Figure 4.1, is a compartment where the interaction of a laser beam and the aerosol takes place.

The chamber has six arms; two of the arms are where the laser beam propagates, the other two arms are for spectroscopic purposes. These arms are used for collection of the light emissions from the reaction in order to study the dynamics of the reaction and also to determine the temperature of the reaction. The other two arms are for the nozzle and the substrate holder. The reactant gases enter the chamber perpendicular to the laser beam through a system of three concentric tubes shown in Figure 4.2, at a controlled pressure. The gases are used to carry the aerosols to the reaction zone where reactions occur and products are formed. The gases further transport the product to a substrate where it is deposited.

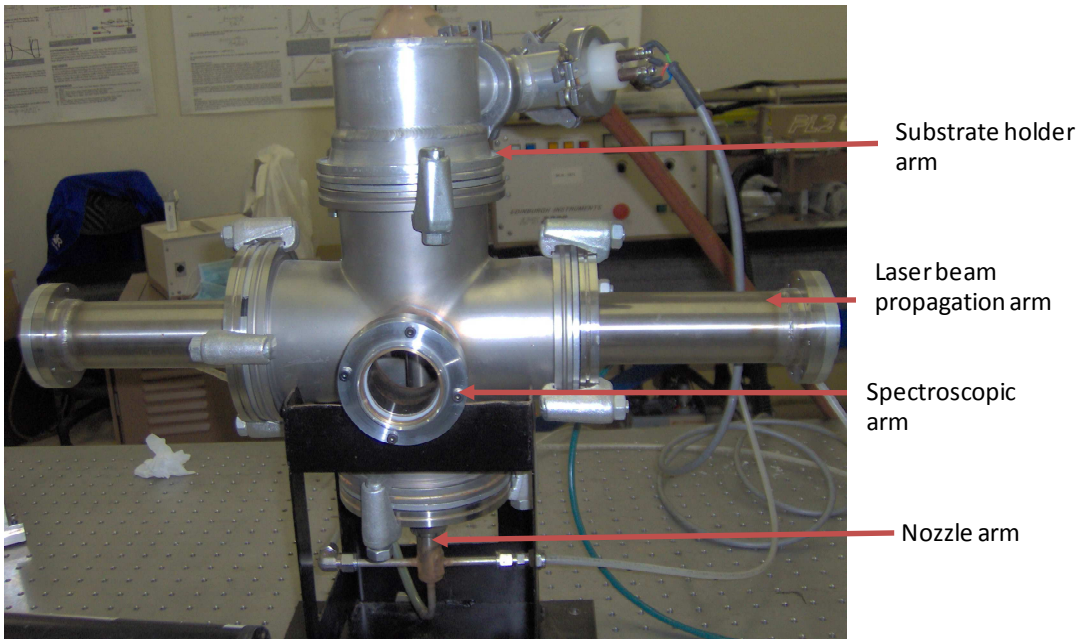

Figure 4.1: A Photograph of a six arm pyrolysis chamber.

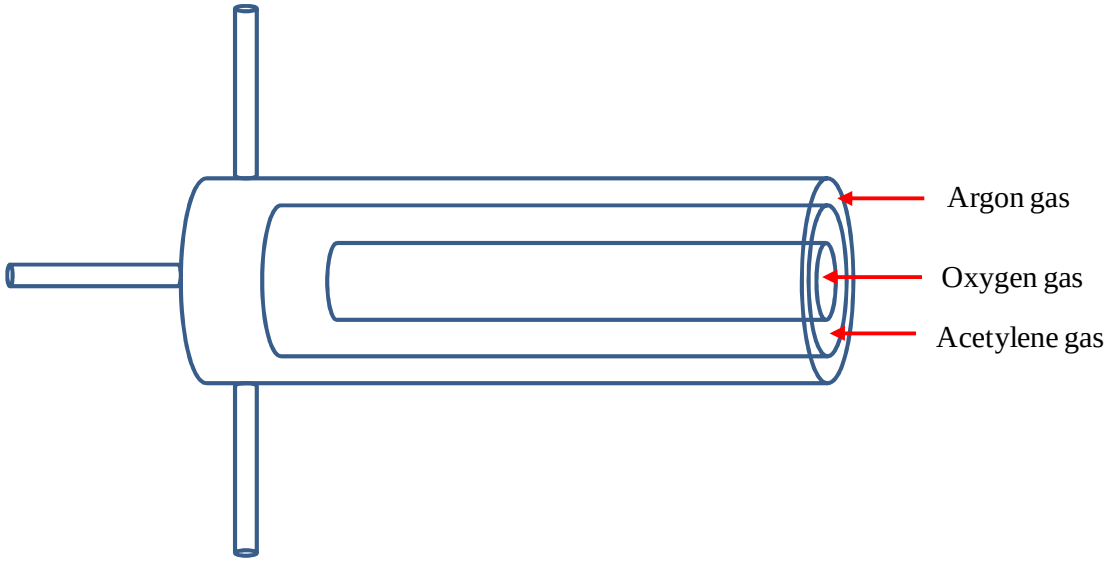

Figure 4.2: A schematic diagram showing a multiflow nozzle. The nozzle has an Argon, Oxygen and Acetylene outlet.

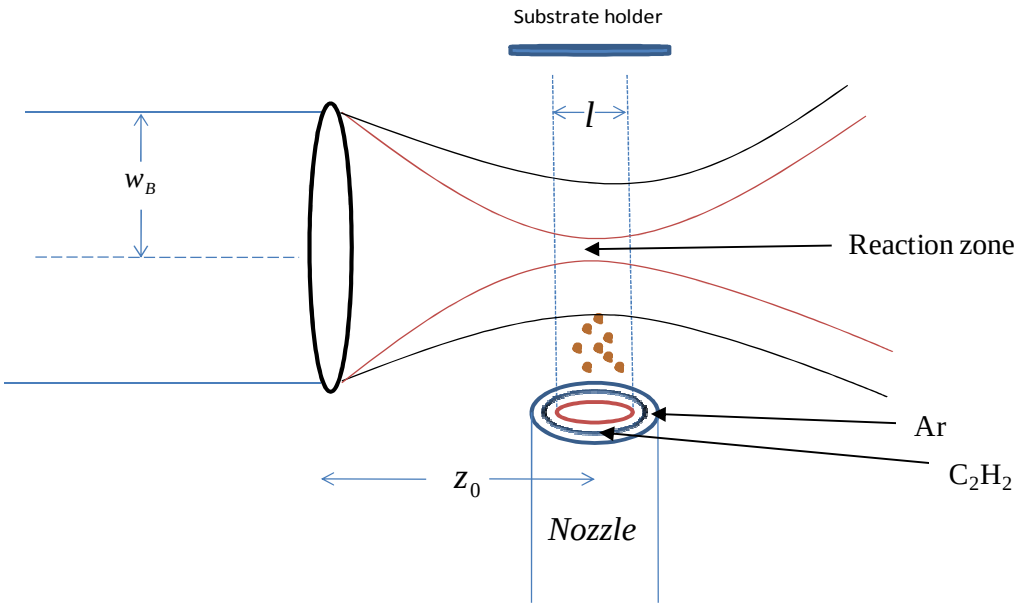

Figure 4.3: Schematic diagram showing the reaction zone inside the reaction chamber.

The red line in Figure 4.3 shows a focusing beam with a small beam waist and results in a small reaction zone but a high power density. On the other hand the black line shows a focusing beam with a large beam waist, this result in a large reaction zone but a low power density.

4.2 Microscopy techniques

There are three known types of microscopy: optical, electron and scanning probe. Optical microscopy involves using visible light and a system of lenses to magnify images of small samples; it is the oldest and simplest of the microscope. Electron microscopy uses a beam of electron to light up the specimen and create a magnified image of it. This microscope has a great resolving power as compared to the light microscope because electrons have much smaller wavelengths. The

scanning probe microscopy uses a physical probe that scans the sample to form images. This technique can reach atomic resolution.

4.2.1 Scanning electron microscope (SEM)

The scanning electron microscope (SEM) has little in common with the transmission electron microscope (TEM) apart from the use of the electron gun and a condenser lens system [48]. The column has only three lenses with no lenses after the specimen, Figure 4.4 shows this.

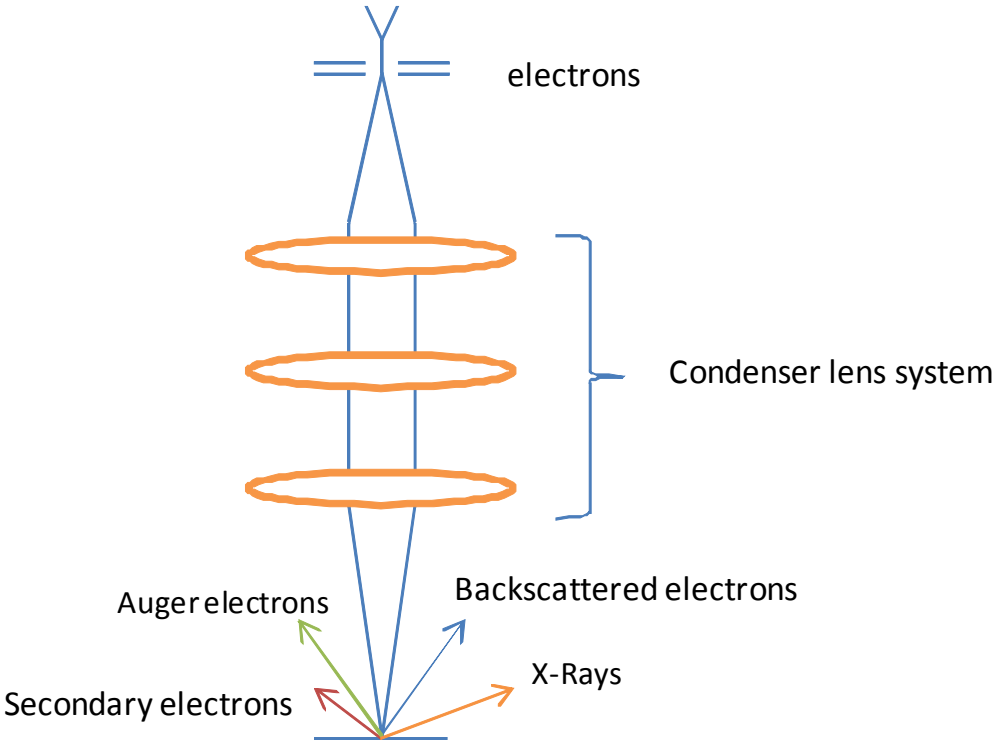

Figure 4.4: A Schematic diagram illustrating the principles of the SEM.

The diagram shows how the lenses produce a focused electron spot on the specimen. Table 4.1 shows the different types of electron sources. The electron gun for SEM is smaller than that of TEM because it produces a lower accelerating voltage (around 30 to 40 kV). The electrons from the source travel to the condenser magnetic lenses. The condenser magnetic lenses used in SEM are smaller than those used in TEM because they do not have to generate a strong magnetic field. The condenser lens system is used to produce a focused electron beam.

Unlike TEM which uses a stationary beam, the SEM incident beam is scanned horizontally across the specimen in two perpendicular directions (x and y) [49]. The x-scan is fast and is generated by a sawtooth-wave generator operating at a line frequency f_x. The y-scan is much slower and is generated by a second sawtooth-generator operating at a frame frequency $f_y = f_x / n$ where n is an integer. The whole process is called the raster scanning and causes the beam to cover the entire rectangular area on the specimen.

The image magnification on SEM is defined by equation 4.1

$$M = \frac{\text{scan distance in the image}}{\text{scan distance on the specimen}}. \qquad (4.1)$$

This is achieved by making the x- and y-scan distances on the specimen a small fraction of the size of the displayed image [49]. The magnification can be controlled over a range of x10 to x500 000.

The specimen of SEM is thick compared to that of TEM, so electrons do not transmit through the specimen. The accelerated electrons are scattered elastically (by electrostatic interaction with atomic nuclei) and inelastically (by interaction with atomic electrons) when they enter the solid. During the impact secondary electrons are emitted with energies of a few eV and re-emission of high-energy backscattered electrons from the primary beam occurs.

Table 4.1: Types of electron sources

Type of source	Tungsten thermionic	LaB_6 thermionic	Schottky emission	Cold field emission
Material	W	LaB_6	ZrO/W	W
φ (eV)	4.5	2.7	2.8	4.5
T(K)	2700	1800	1800	300
E(V/m)	Low	Low	$\approx 10^8$	$>10^9$
J_e(A/m2)	$\approx 10^4$	$\approx 10^6$	$\approx 10^7$	$\approx 10^9$
β (Am-2/sr-1)	$\approx 10^9$	$\approx 10^{10}$	$\approx 10^{11}$	$\approx 10^{12}$
d_s(μm)	≈40	≈10	≈0.02	≈0.01
Vacuum (Pa)	$<10^{-2}$	$<10^{-4}$	$<10^{-7}$	$\approx 10^{-8}$
Lifetime (hours)	≈100	≈1000	$\approx 10^4$	$\approx 10^4$

ΔE (eV)	1.5	1.0	0.5	0.3

Auger electrons and x-ray photons are also emitted from the specimen during the bombardment of the specimen. The secondary electrons are collected by a detector and translated into a signal. The signal is then amplified, analysed and translated into an image of the topography being investigated. The backscattered electrons can also be used for imaging but this type of imaging is used to distinguish one material from another. The Auger electrons and x-ray emissions can be used for elemental analysis. This will be discussed more in the next section.

SEM is used to image the morphology and topology of the specimen being studied. Figure 4.5 shows an image from SEM.

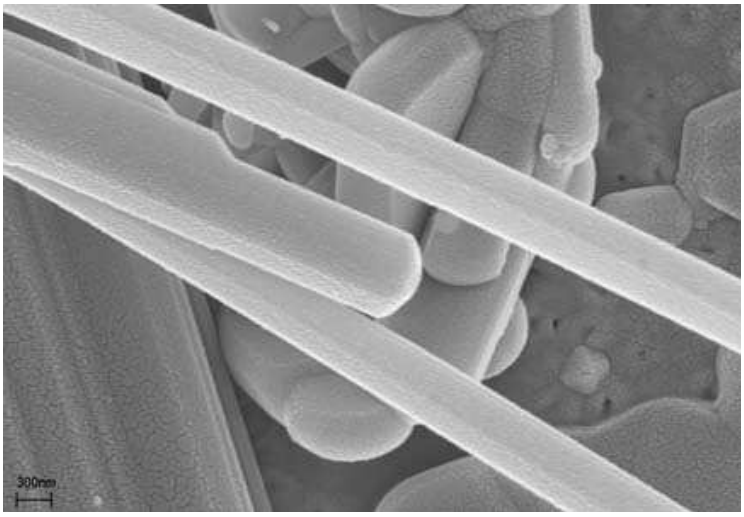

Figure 4.5: A picture of a SEM image showing VO_2 nano-rods [17].

4.2.2 Energy Dispersive X-Ray spectroscopy (EDAX or EDS)

Although energy dispersive x-ray spectroscopy (EDS) is not a microscopy technique but a spectroscopy technique, I will discuss it in this section because it is often found on the SEM or TEM microscope. The EDS technique detects x-rays emitted from the specimen (Figure 4.4) during electron bombardment to characterise and quantify the elemental composition of the specimen at that volume.

The technique uses a semiconductor detector to classify x-ray radiation according to energy rather than wavelength [48]. The semiconductor detector is an energy dispersive device fabricated from a single crystal of silicon or germanium [49]. The detector converts the energy of the incident x-ray photons into pluses of current proportional to the photon energy [49]. These pulses are amplified, digitised and finally fed to into a multichannel analyser which stores them in a location appropriate to the pulse height [49]. The final spectrum is then displayed on a monitor which can be monochrome or colour. Figure 4.6 shows an example of an EDS spectrum. Each peak in the spectrum represents an element present within a known region of the specimen [49].

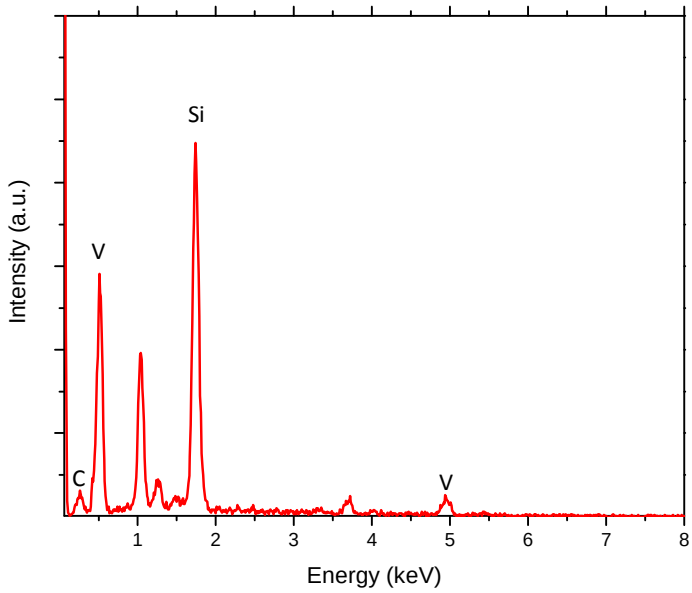

Figure 4.6: A typical EDS spectrum of a vanadium oxide sample.

The atom of every element releases x-rays with unique amounts of energy during the transfer process. So by measuring the amount of energy of the x-rays being emitted by the specimen during electron bombardment, the identity of the atom can be known.

Figure 4.7 shows a diagram of an atom with shells, the shells are labelled K, L, M, N from innermost to outermost because of the differing binding energy levels of the electrons around the nucleus. If a primary electron knocks out an electron on the K-shell then the electron on the L-shell will de-excite to the K-shell releasing an x-ray, Figure 4.8 illustrates.

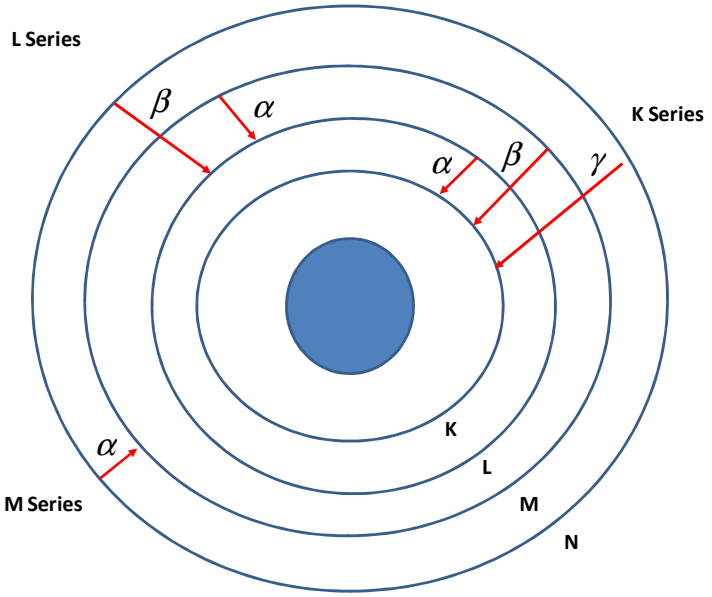

Figure 4.7: A schematic diagram showing the energy content of X-Rays emitted by their electrons as transfer from a higher-energy electron shell to a lower-energy electron shell.

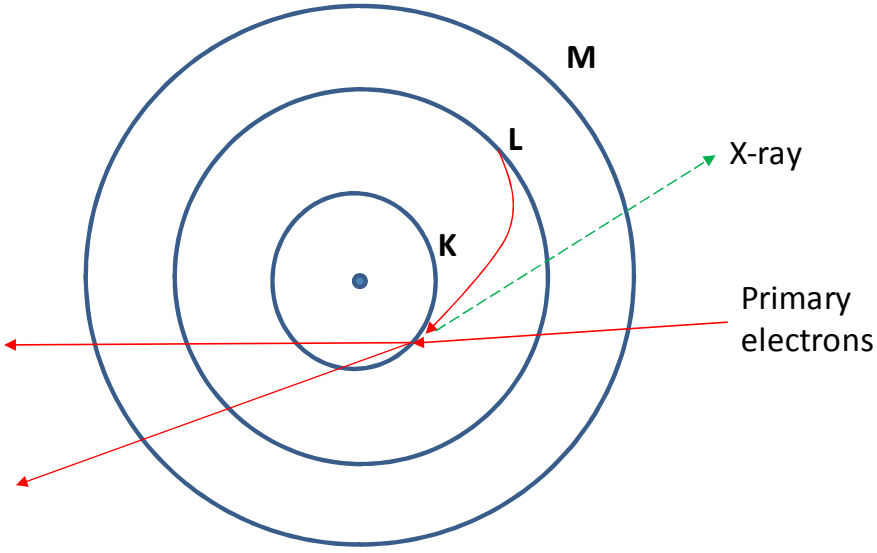

Figure 4.8: A schematic diagram showing the emission of an X-ray.

4.3 Spectroscopy techniques

Spectroscopy is the use of radiation, sound and particle emission to study matter. There are different methods of spectroscopy: electromagnetic spectroscopy which involves interaction of electromagnetic radiation with matter, electron spectroscopy which involves interaction of electron beams with matter and acoustic spectroscopy which involves interaction of frequency of sound with matter. In this section: Raman spectroscopy, x-ray diffraction, photoluminescence spectroscopy and ultraviolet-visible spectroscopy will be discussed.

4.3.1 Raman Spectroscopy

When a photon of light is incident on a specimen, the photon can be absorbed or scattered. For absorption to occur the energy of the incident photon must be equal to the energy difference between two states of the molecule and the transition between the two states must be accompanied by a change in the dipole moment. If these conditions are not met the photon can be scatted in two ways, elastically or inelastically. A process when photons scatter elastically is called Rayleigh scattering. In Rayleigh scattering, the incident energies of the photons are the same as the energies of the scattered photons. On the other hand, a process when photons scatter inelastically is called Raman scattering. In this process the incident energies of the photons are different from the energies of the scattered photons.

So when monochromatic radiation of wavenumber v_0 is incident on a specimen and interacts with the specimen then new pairs of wavenumbers of the type $v = v_0 \pm v_M$ are observed [50]. In the molecular systems the wavenumbers v_M are

found to lie in the ranges associated with transitions between rotational, vibrational and electronic levels [50]. These new wavenumbers are called Raman lines and collectively they form a Raman spectrum. Raman lines at wavenumbers less than the incident wavenumber ($v_0 - v_M$) are called Stokes lines and those greater than the incident wavenumber ($v_0 + v_M$) are called anti-Stokes lines, Figure 4.9 shows an illustration of this. It can be noticed in Figure 4.9 that the Stokes and anti-Stokes lines are equally displaced from the Rayleigh line. This is because in either case one vibrational quantum of energy is lost or gained. It can also be noticed that the Stokes line is more intense than the anti-Stokes line. This is because only molecules that are vibrationally excited prior to irradiation can give rise to the anti-Stokes line, so only the more intense Stokes lines are measured.

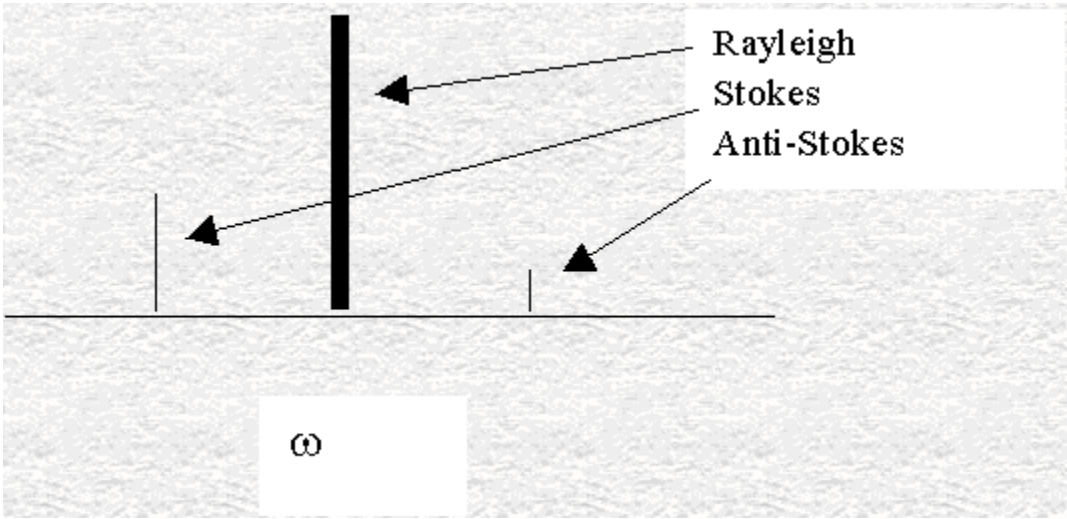

Figure 4.9: A schematic diagram showing how a Raman spectrum may appear.

A block diagram in Figure 4.10 shows the components of the equipment necessary for the observation of Raman spectra [50]. These components include a source of monochromatic radiation, a sample device, a dispersing system and a detection device. Each of these components will be discussed.

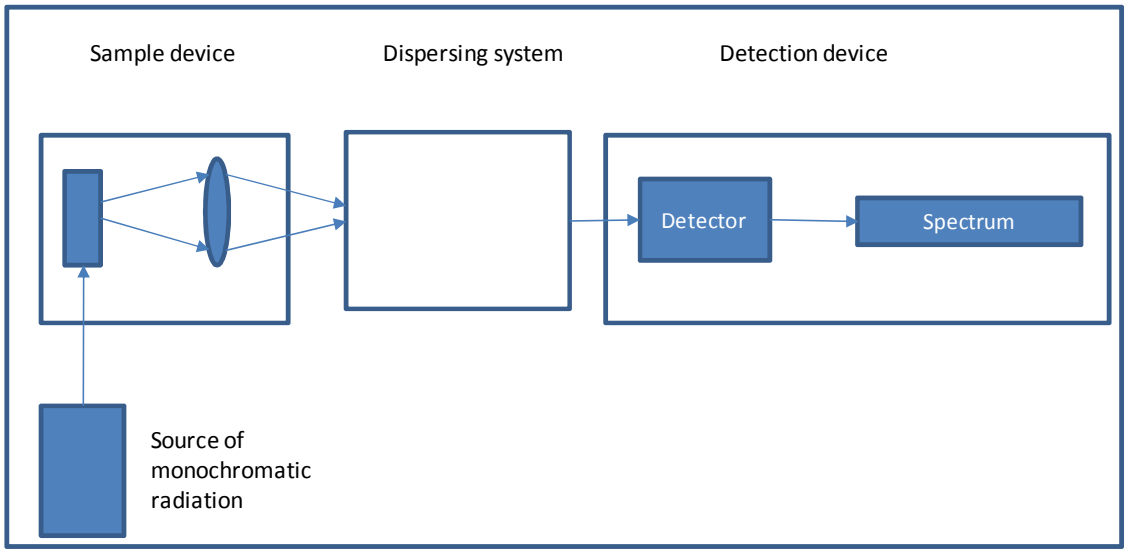

Figure 4.10: A block diagram of equipment for observation of Raman Spectra.

The requirements for the source are that it must be highly monochromatic and capable of giving a high irradiance at the sample. Gas lasers meet these requirements and provide radiation which is self-collimated and plane polarized [50]. Helium Neon (HeNe) laser, Krypton (Kr) laser, Argon (Ar) laser and Kr/Ar laser are examples of gas lasers that can be used as a source of excitation. The sample device is responsible for the illumination of the sample and collection of the scattered radiation for subsequent dispersion. The sort of the dispersing system depends on whether it is to be used for the resolution of individual lines in rotation and vibration-rotation Raman lines or for the study of vibrational lines under conditions of moderate resolution [50], the two kinds of study call for different design features. In both studies the dispersing system is described as a spectrograph. The last component, the detection device, is where data is acquired

and a curve fitted. In modern spectrometers the detectors are a charge-couple device (CCD). Figure 4.11 shows an example of a Raman spectrum obtained from the spectrometer.

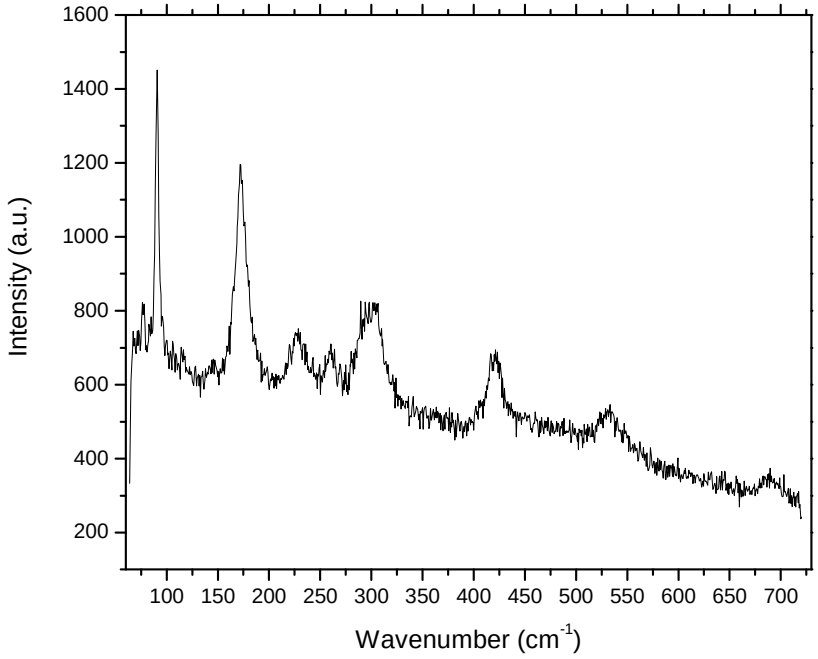

Figure 4.11: A typical Raman spectrum of a vanadium oxide thin film.

4.3.2 X-Ray diffraction (XRD)

X-ray diffraction (XRD) is a non-destructive analytical technique for identification and quantitative determination of the various crystalline forms of compounds present in solid materials and powders. Identification of an unknown compound is achieved by comparing the samples diffraction pattern with an internationally recognised data base containing reference patterns for many

phases. XRD also gives information on the crystallography of the sample from studying the interaction of monochromatic x-rays with a periodic crystal lattice.

In X-ray diffraction the incident X-ray radiation is scattered by the atom in all directions, Figure 4.12 illustrates. So when a monochromatic X-ray beam with wavelength λ, on the order of lattice spacing d, is projected onto a crystalline material at an angle θ, XRD peaks are produced by constructive interference of monochromatic beam scattered from each set of lattice planes at specific angles.

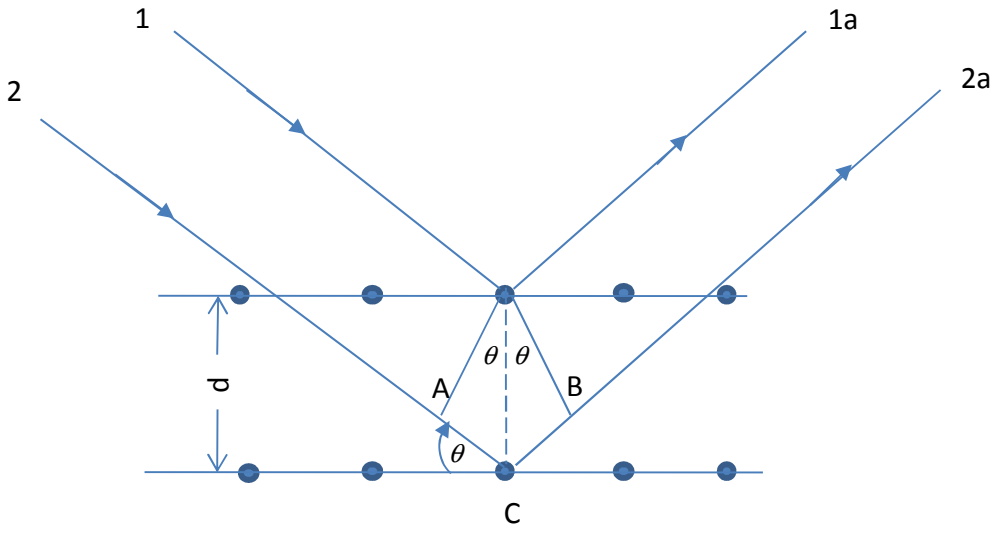

Figure 4.12: A diagram showing diffraction of X-rays in a crystal.

From Bragg's law given by

$$n\lambda = 2d \sin\theta \qquad (4.2)$$

where λ is the wavelength, d is the lattice spacing and θ is the angle of incident. The diffraction peaks can be determined from constructive interferences. By varying the angle θ, the Bragg's law conditions are satisfied by different d-spacing in polycrystalline materials.

Figure 4.13 shows a schematic layout of a diffractometer which has a 4 slit arrangement. The X-rays are produced in the source and propagate through the diffraction slit (DS) whose function is to define the irradiated sample area. (A narrower slit gives a slightly lower noise). The X-rays then diffract at the sample and propagate through the scattering slit (SS) which has a similar function to the DS. From the SS the X-rays travel to the receiving slit (RS) which optimizes the incoming radiation because a small slit will cut down on the incoming signal and a large slit will decrease the signal/noise ratio and broaden the peaks. The X-rays will then go through the receiving slit monochromator (RSM) to the detector. Figure 4.14 shows an example of an XRD spectrum.

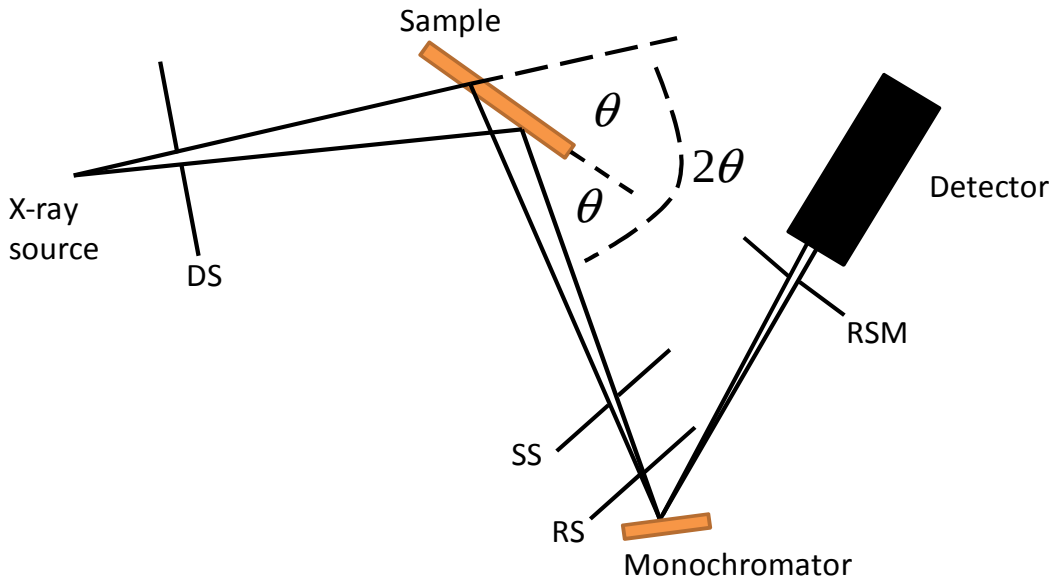

Figure 4.13: A schematic diagram of a diffractometer.

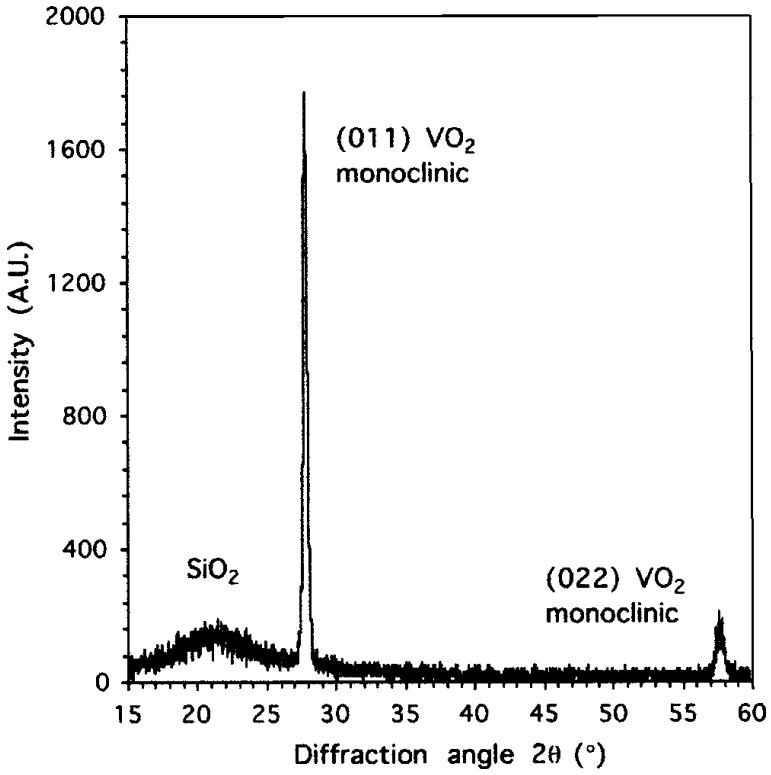

Figure 4.14: An XRD spectrum of VO_2 deposited on glass [15].

4.3.3 Ultra violet-Visible-Near infrared spectroscopy (UV-VIS-NIR)

Ultra violet-Visible-Near infrared (UV-VIS-NIR) spectroscopy probes the electronic transitions of molecules as they absorb light in the ultraviolet (UV), near-infrared (NIR) and visible (VIS) regions of the electromagnetic spectrum. This technique is capable of measuring absorbance, transmittance and reflectance of both liquid and solid (thin films) samples from around 175-3300 nm.

The spectrophotometer measures the intensity of light passing through the sample (I), and compares it to the intensity of light before it passes through the sample

(I_0). The ratio $\frac{I}{I_0}$ is called transmittance and is expressed as a percentage ($\%T$).

The absorbance, A, is based on the transmittance and is given by

$$A = -\log\left(\%T / \%100\right) \tag{4.3}$$

A basic spectrophotometer is shown in Figure 4.15. The basic components are a light source, a holder for the sample, a monochromator (to separate the different wavelengths of light) and a detector. Figure 4.16 shows an example of a UV-VIS-NIR spectrum. In Figure 4.16 there are three transmittance T(λ) curves at UV–Vis–NIR wavelengths. Insulator state T(λ) is pretty much the same at longer wavelengths for both samples, only there is 5% higher transmittance below 1200nm in the polycrystalline film deposited at higher oxygen pressure. In the metal state, the transmittance curves are almost identical. Insulator state T(λ) data was reasonably fitted with Lorentz multiple oscillator model with RMSE < 0.5 [51].

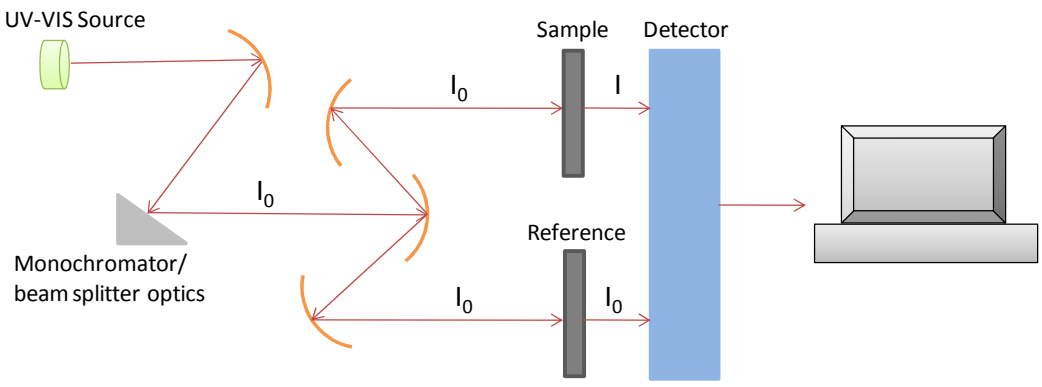

Figure 4.15: A schematic diagram of UV-VIS-NIR spectrophotometer.

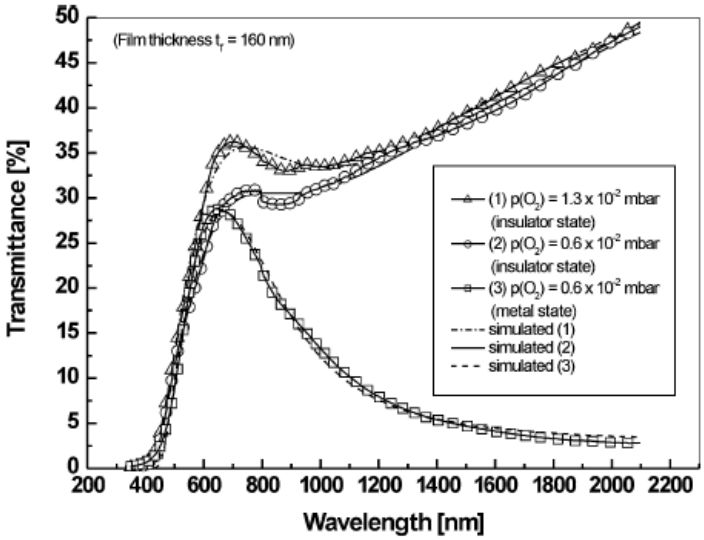

Figure 4.16: A UV-VIS-NIR spectrum of VO_2 [51].

Chapter 5: Deposition Parameters

5.1 Introduction

As mentioned in chapter 1, the laser pyrolysis technique has the ability to synthesis pure products [23]. For this reason it was chosen in this work instead of the other techniques. This work is a follow up on B. Mwakikunga et al [17] report on the deposition of VO_2 nanostructures using a CO_2 laser beam at a wavelength of 10.6 µm at a constant power of 50 W.

In the present study the focus was on making VO_{2-x} depositions using the laser pyrolysis technique: (1) while the laser power was kept constant at 30 W and the laser wavelength varied at eight allowed lines, and (2) while the laser wavelength was kept constant at 10.6 µm and the power varied from between 0-65 W. The aim was to investigate the effect of wavelength and laser power in the formation of VO_{2-X} nanostructures.

5.1.1 Power dependent and wavelength dependent VO_{2-x} depositions using unfocused CO_2 laser beam

A wavelength tuneable Continuous Wave (CW) CO_2 laser (Edinburgh Instruments, PL6) was used to pyrolyse the vanadium ethoxide liquid precursor. The precursor was prepared by dissolving 1 g of vanadium trichloride (VCl_3) powder (97 % Sigma-Aldrich) into 100 ml of ethanol (CH_3CH_2OH) (≤ 99.8 % Sigma-Aldrich). The solution was stirred for 3 hours using a magnetic stirrer and

then left for 3 days for the reaction to complete. In Figure 5.1 the green solution indicates the +3 oxidation state of vanadium and this occurs when the VCl_3 is dissolved in ethanol. The blue solution indicates the +4 oxidation state of vanadium and occurs after 3 days. The vanadium ethoxide solution was placed in a nebuliser holder (Medel, family silver), sprayed into the reaction zone through the nozzle (Figure 4.2) and collected on the substrate. Corning® glass was used as a substrate for the deposition of the vanadium oxide. The dimensions of the glass substrate were about 1 cm by 1 cm.

The samples were annealed at 500^{o}C for 17 hours in an argon environment.

A set of eight different samples (VEW1-VEW8) of thin VO_{2-x} films were synthesized utilising different deposition parameters shown in Table 5.1. The flow rates for C_2H_2, Ar and O_2 gases were kept constant at 30, 50 and 5 ml/min accordingly. For this set the laser beam was kept unfocused and at a constant power of 30 W.

An additional set of twelve different samples (VEP1-VEP12) of the thin VO_{2-x} films were also synthesized at different deposition parameters tabulated in Table 5.2. The flow rates for C_2H_2, Ar and O_2 gases were kept constant at 30, 50 and 10 ml/min accordingly. For this set the laser beam was kept unfocused and at a constant wavelength of 10.6μm.

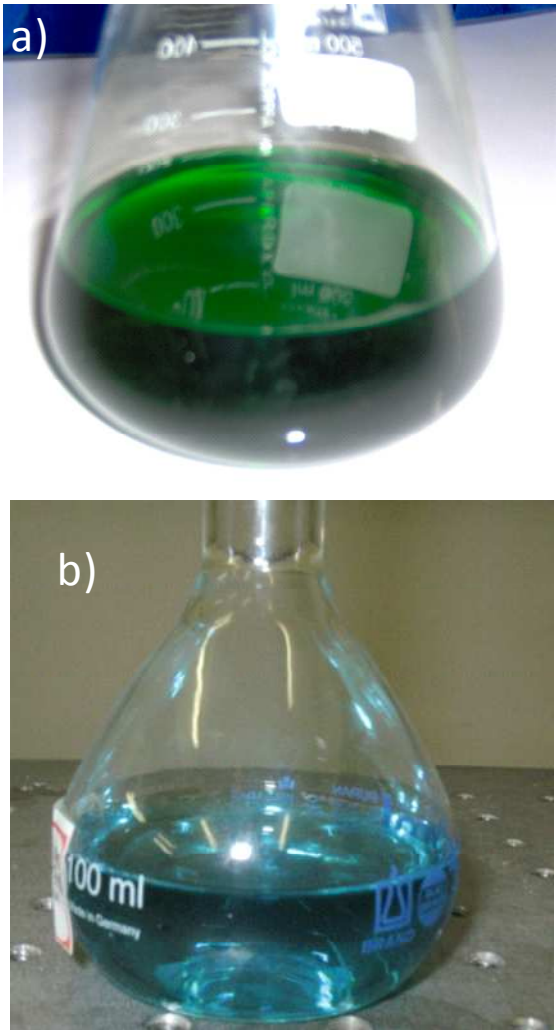

Figure 5.1: Photographs of the VCl_3 in ethanol solution a) before 3 days and b) after 3 days.

Table 5.1: Laser pyrolysis deposition parameters at a constant power of 30 W of an unfocused beam.

Sample number	Wavelength (µm)	C_2H_2 flow rate (ml/min)	O_2 flow rate (ml/min)	Ar flow rate (ml/min)
VEW 1	9.22	30	5	50
VEW 2	9.32	30	5	50
VEW 3	9.48	30	5	50
VEW 4	9.70	30	5	50
VEW 5	10.16	30	5	50
VEW 6	10.36	30	5	50
VEW 7	10.48	30	5	50
VEW 8	10.82	30	5	50

Table 5.2: Laser pyrolysis deposition parameters at a constant wavelength of 10.6 µm of an unfocused beam.

Sample number	Power (W)	Power density (W/cm^2)	C_2H_2 flow rate (ml/min)	O_2 flow rate (ml/min)	Ar flow rate (ml/min)
VEP 1	10	16.825	30	10	50
VEP 2	15	25.237	30	10	50
VEP 3	20	33.650	30	10	50
VEP 4	25	42.063	30	10	50
VEP 5	30	50.475	30	10	50
VEP 6	35	58.888	30	10	50
VEP 7	40	67.300	30	10	50
VEP 8	45	75.713	30	10	50
VEP 9	50	84.125	50	10	50
VEP 10	55	92.538	30	10	50
VEP 11	60	100.950	30	10	50
VEP 12	65	109.363	30	10	50

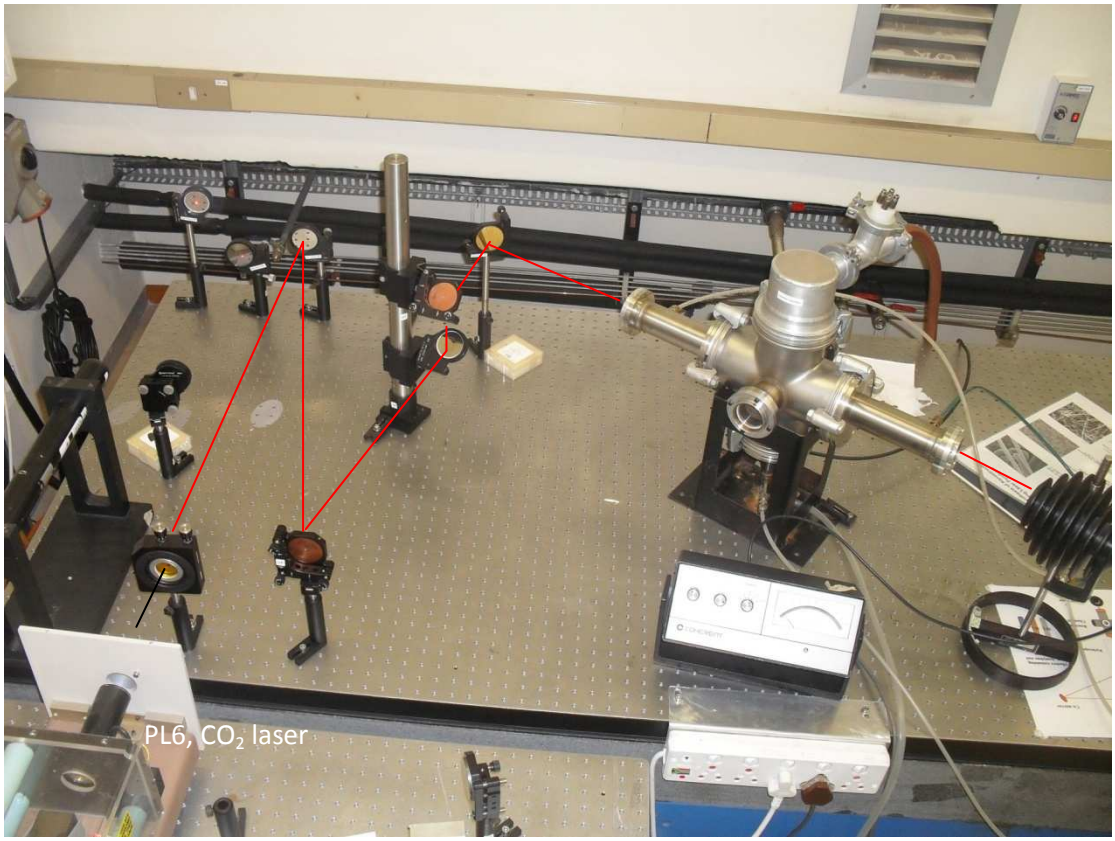

Figure 5.2: Optical layout of the laser pyrolysis experiment showing the delivery of the CO_2 laser beam into the reaction chamber.

5.1.2 VO_{2-x} deposition using a 30 W focused CO_2 laser beam at 10.6 µm wavelength

A non-tuneable CO_2 laser (Synrad, D48-2-115) was used to pyrolyse the vanadium ethoxide liquid precursor. This laser has a fixed wavelength of 10.6 µm and a maximum power of 30 W. The same solution (VCl_3 in ethanol) mentioned earlier was used as the precursor and the product was collected on a Corning® glass substrate. Figure 5.3 shows the experimental setup. Depositions where made at a constant laser power and laser wavelength, Table 5.3 shows the parameters used for the deposition.

Figure 5.3: Optical layout of the laser pyrolysis experiment showing the delivery of the focused CO_2 laser beam into the reaction chamber.

Table 5.3: Laser pyrolysis deposition parameters for a focused beam

Sample number	Power (W)	Wavelength (µm)	Beam waist (mm)	C_2H_2 flow rate (ml/min)	Ar flow rate (ml/min)
VB	30	10.6	0.89	15	12

Chapter 6: Results and Discussions

6.1 Introduction

In this section the morphology, structure and optical properties of the thin films synthesized under the different conditions tabulated in Table 5.1 to Table 5.3 are discussed. It can be seen that by changing the laser pyrolysis parameters such as laser wavelength, laser power and power density, the morphology and optical properties of the samples are affected.

6.2 X-ray diffraction (XRD)

The crystal structure of the three set of samples synthesized under the different growth conditions shown in Table 5.1 to Table 5.3 have been investigated using a Phillips (PANalytical) X-ray diffractometer using Cu Kα (k = 1.54 Å) radiation source

The XRD spectra (scanned from 5^o to 90^o) corresponding to samples VEW1-8, synthesized at different wavelengths and constant laser power of 30 W are shown in Figure 6.1 (a). The diffraction spectra indicate that the samples synthesized at wavelengths between 9.32 µm and 10.86 µm are amorphous as no distinct peaks were observed. The above does not apply to sample VEW1 which has been synthesized at a wavelength of 9.22 µm. The corresponding XRD spectrum for this is shown in Figure 6.1 (b). Interestingly, two peaks at $2\theta=29.1^o$ and $2\theta=44.3^o$ are visible, and correspond to the VO_2 (B) compound [52]. These diffraction

peaks can be indexed to the VO_2 (B) monoclinic structure with lattice constants of a = 2.03 Å, b = 3.693 Å and c = 6.42 Å, and β = 106.6° (JCPDS # 31 -1438). The spectrum also exhibits a broad hump at around $2\theta=22^{o}$-40^{o} which is due to the SiO_2 in the glass substrate.

No peaks of any other phases or impurities are observed, demonstrating that almost pure VO_2 (B) nano-materials could be obtained using the laser pyrolysis process.

It is important to note that by having kept the laser power density at relatively low levels, it made it possible to assess the significance of the laser wavelength alone in terms of its contribution to the different growth mechanisms involved within the reaction volume.

There is an inverse relationship between the energy of a photon (E) and the wavelength of the light (λ) given by the equation,

$$E = \frac{hc}{\lambda}, \qquad (6.1)$$

where h is Planck's constant and c is the speed of light. The above inverse relationship means that light consisting of high energy photons has a short wavelength and light consisting of low energy photons has a long wavelength. In the case where the wavelength is varied from 9.22 µm to 10.86 µm it is observed that only the 9.22 µm sample is crystalline and the product is VO_2 (B). The formation of the product could be due to the high energy (eV) photons for this wavelength (9.22 µm) as described in equation (6.1).

It is possible that, at wavelengths longer than the 9.22 μm the laser beam do not dissociate the molecular bonds which form VO_2 (B) crystalline products but merely excite those bonds. The laser beam wavelengths could be far from resonance to form the desired product, i.e. $\lambda_{laserbeam} >> \lambda_{desired\ dissociation\ bond}$. In that case other non-crystalline vanadium oxide products might be formed which are invisible to XRD analysis because they are non-crystalline.

From the formula VO_{2-x} and the XRD results presented above, we can hypothesize the value of x to be x = 0 since XRD revealed the phase of the sample to be VO_2 (B). However, the best technique to verify this would be X-ray photoelectron spectroscopy (XPS).

The XRD spectra (scanned from 5^o to 90^o) of samples VEP1-VEP12 synthesized at different laser powers are shown in Figure 6.2. The spectra show the absence of XRD peaks from the 10 W to 40 W laser powers indicating that the samples are amorphous. For laser powers above the 45 W a peak at $2\theta=18.4^o$ is observed which corresponds to the β-V_2O_5 [52] vanadium oxide phase. Above the 45 W laser power the samples shows a polycrystalline state and below the 45 W powers the samples shows an amorphous state. Figure 6.3 shows a spectrum of the 65 W laser power with peaks at $2\theta=12.5^o$ and $2\theta=18.4^o$ corresponding to β-V_2O_5 [52, 53] while the $2\theta=29.1^o$ peak observed corresponds to the VO_2 (B) [52]. This indicates that the sample exhibits mixed phases of vanadium oxides.

The VO_2 (B) phase is gradually formed by the thermal decomposition of V_2O_5 during the annealing process [54]. V_2O_5 is the most stable of the vanadium oxides

but when it is in a high temperature reducing environment such as in a furnace it can transform from V_2O_5 to VO_2.

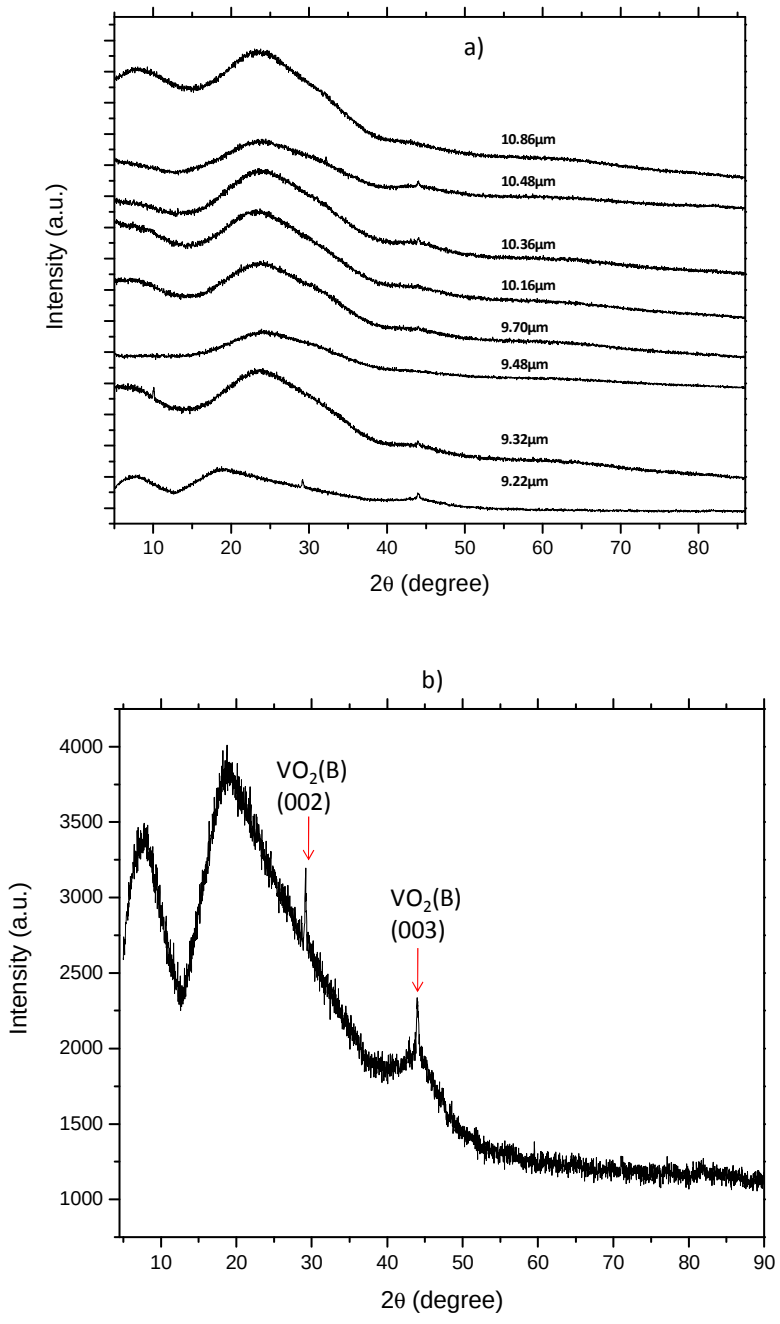

Figure 6.1: (a) X-ray diffraction patterns of VO_{2-x} deposited at different wavelengths. (b) X-ray diffraction pattern of VO_{2-x} deposited at a wavelength of 9.22 µm.

Having kept the wavelength constant at a value of 10.6 μm, which is situated further away from the rather optimum value of 9.22 μm which corresponds to the wavelength threshold at which photolysis-photochemistry related mechanism is triggered, a second set of samples was produced as a function of varying laser power density. In this manner, one can now assess the contribution of the purely thermal induced processes within the reaction volume and a lower power density threshold can be established.

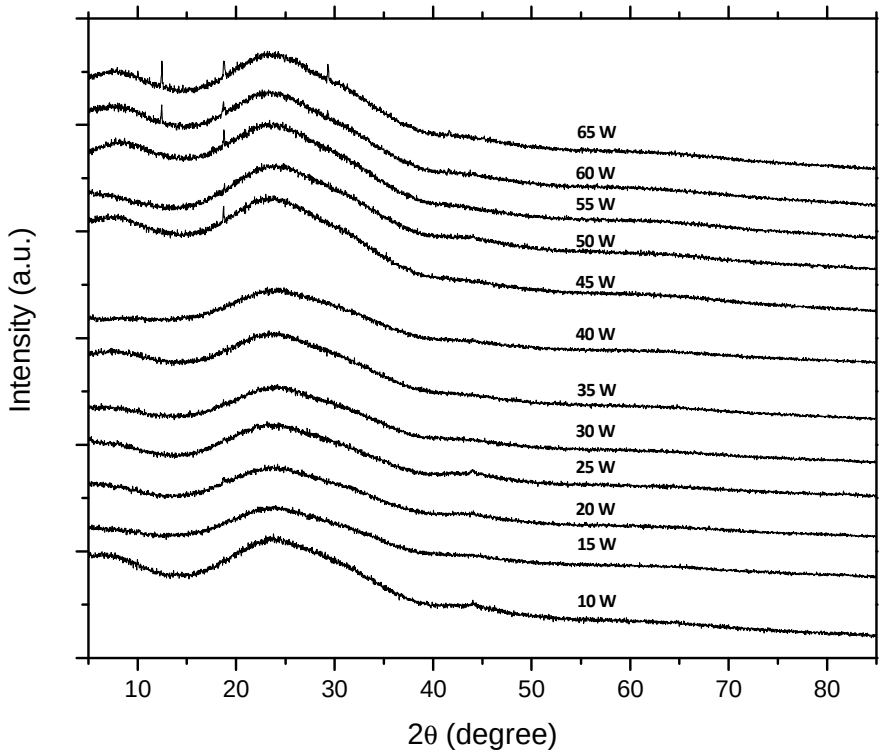

Figure 6.2: X-ray diffraction patterns of VO_{2-x} deposited at different laser powers.

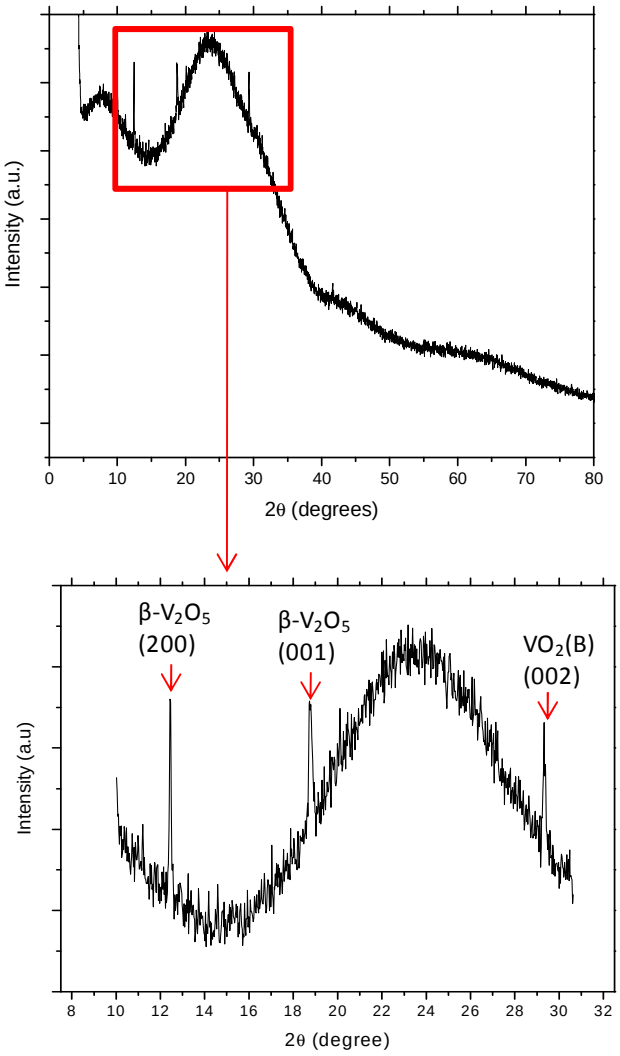

Figure 6.3: X-ray diffraction patterns of VO_{2-x} deposited at 65 W.

Also, from the results we have just presented we can hypothesize the value of x, from the formula VO_{2-x}, to be x = 2.5 in some instances and x = 0 in another. The reason for these differences is because of the mix phases of vanadium oxide present in the sample (VO_2 (B) and β-V_2O_5). In some areas the sample is made up of β-V_2O_5 while in others it is made up of VO_2 (B). Again XPS would be the best technique to employ to determine the exact value of x.

XRD analysis (spectrum scanned from 5^o to 90^o) is also performed on a sample (VB) synthesised with higher power density (2.2 kW/cm^2) and 10.6 μm laser wavelength is shown in Figure 6.4. The spectrum shows a distinct peak at $2\theta=44.1^o$ which corresponds to VO_2 (B). The absence of the other peaks might be caused by the size of the particles. The small broadness of the peak corresponding to bulk material (very narrow peak at ~ 43^o) confirms that the particles are indeed nano in size. The spectrum also shows no evidence of other phases of vanadium oxide present in the sample. The spectrum hump at around $2\theta=22^o$-40^o is due to the SiO_2 in the glass substrate.

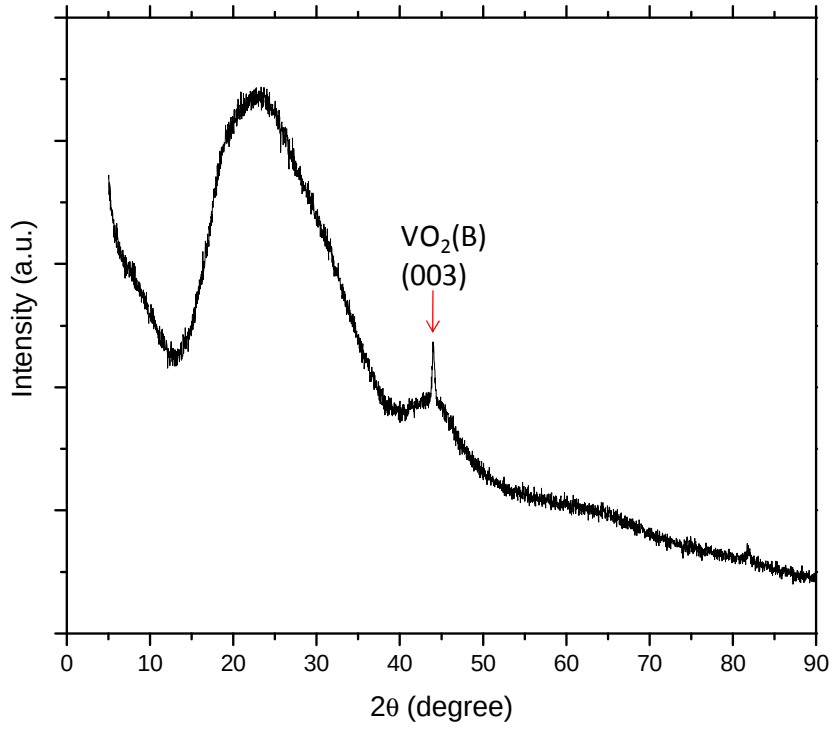

Figure 6.4: X-ray diffraction patterns of VO_2 (B) observed in the VB sample.

6.3. Morphology of the thin films

Morphological studies and analysis are performed using the LEO 1525 field emission scanning electron microscope (SEM). The elemental composition is also investigated by using the Energy Dispersive X-Ray spectrometer (EDS) which is attached to the SEM instrument.

The morphology of sample (VB) synthesized with a focused beam at a power density of 2.2 kW/cm^2, a laser power of 30 W and a laser wavelength of 10.6 μm is shown in Figure 6.5. Rod-like nanostructures scattered all over the sample are observed. The observed structures have an average diameter of 55 nm and an average length of 400 nm. There are other nano-structures present in the sample but the dominant structures are the nano-rods.

It is important to note that such VO_2 nano-rods of this particular cylindrical geometry and rather small size have not been produced before. There are reports of course from various groups in the relevant literature on larger nano-platelets/nano-belts structures synthesised with different techniques including laser pyrolysis [17, 29]. B. Mwakikunga et al. [17] have reported on VO_2 nano-belts formation using similar synthesis conditions. The large morphological differences between those structures and the VO_2 nano-rods grown in the present studies indicate that even extremely subtle parameter variation during the laser pyrolysis method, such as intensity, wavelength, residence time within reaction volume and annealing conditions, can have an enormous effect.

EDS analysis, shown in Figure 6.6 (a), indicates the presence of vanadium, oxygen, carbon, calcium, silicon, potassium and sodium atoms. The X-ray peaks

due to Ca, Si, K and Na are associated with the impurities being present in the substrate, shown in Figure 6.6 (b), while the oxygen peak is attributed to contributions from both the substrate and precursors. Since glass is not conducting, the sample was coated with a carbon layer in an evaporation vacuum chamber to make it conductive.

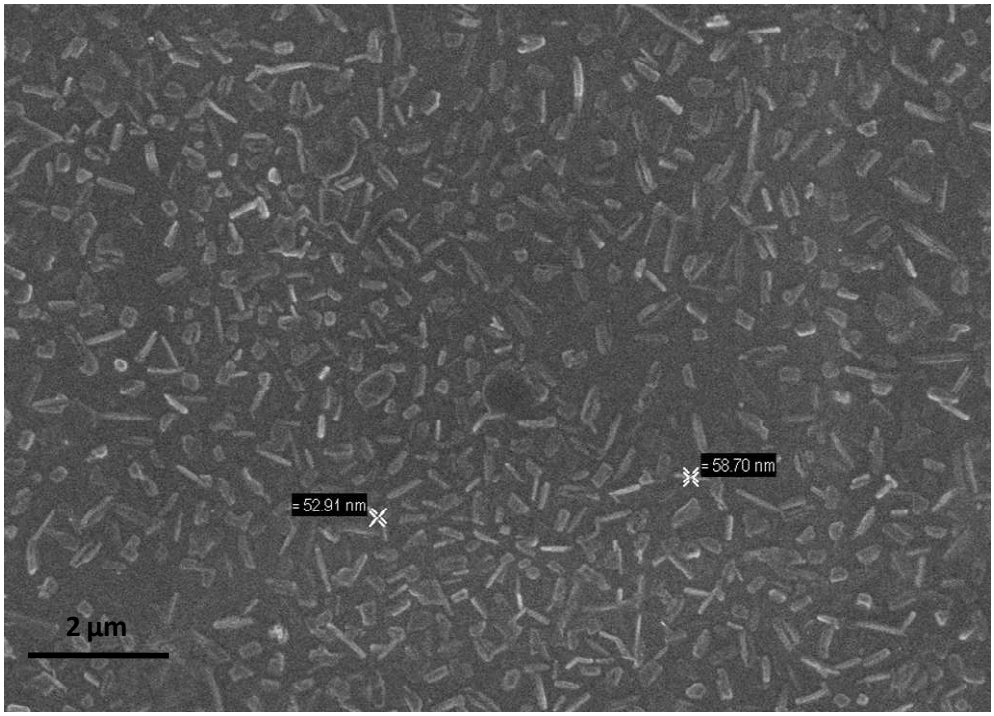

Figure 6.5: A SEM micrograph showing the morphology of the sample VB synthesized using a focused laser beam at 30 W power, 10.6 µm wavelength and a flow rate of 15 ml/min.

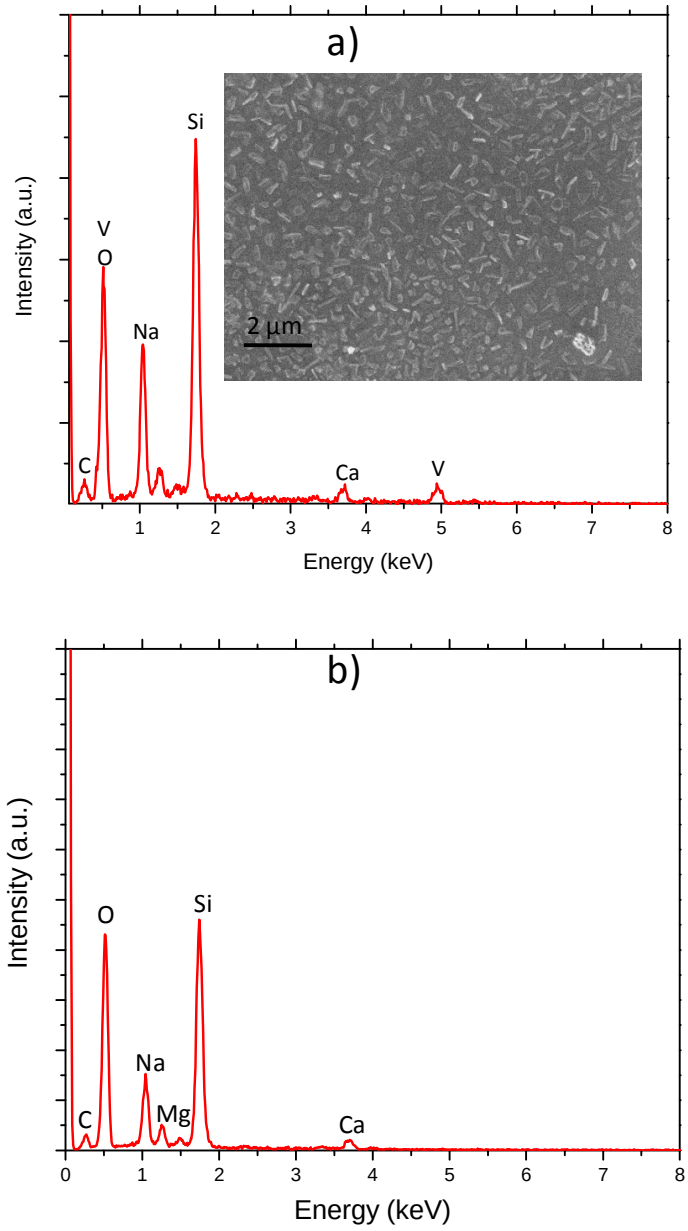

Figure 6.6: (a) A SEM micrograph showing the morphology and the EDS spectra of the sample VB synthesized using a focused laser beam 30 W power, 10.6 µm wavelength and a flow rate of 15 ml/min. (b) EDS spectrum of the glass substrate.

Sample VEW1 showed a different morphology to sample VB as shown in Figure 6.7. Islands with cracks are observed with each individual micro-crack [Figure 6.7

(b)] harbouring self assembled nanostructures [Figure 6.7 (c)] which unveiled to be 70 nm nano-rods , nano-slabs and what seemed to be nano-spheres [Figure 6.7 (d)]. EDS analysis, Figure 6.8, shows the same atoms as in Figure 6.6. The analysis shows the presence of the vanadium, oxygen, carbon, calcium, silicon, potassium and sodium atoms. Here also, the Na, K, Ca and Si originate from the glass substrate. The quantities of these atoms in percentages are shown in Table 6.1. Vanadium and oxygen atoms accounted 11.57 % and 36.99 % respectively. Although oxygen shows a large percentage, the contribution originates from both the glass substrate and the precursor.

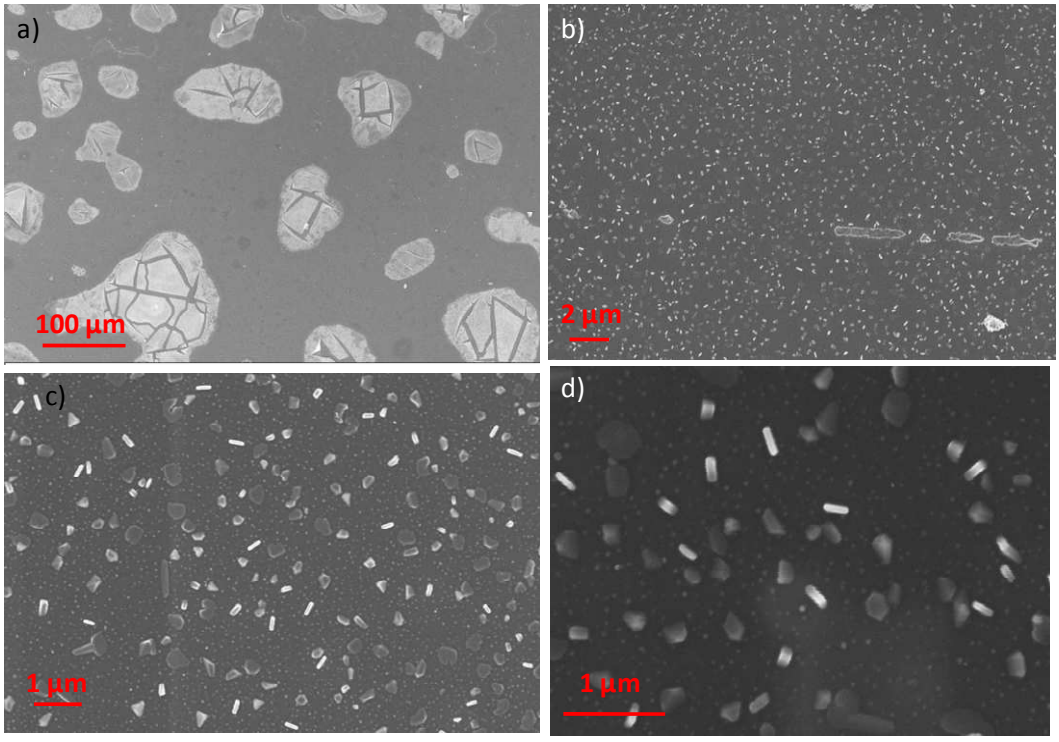

Figure 6.7: SEM micrographs of sample VEW1 VO_{2-X} structures (a) islands with cracks (b) nanostructures growing with each micro-crack at a magnification of x10000 (c) nanostructures growing with each micro-crack at a magnification of x35000 and (d) nano-rods, nano-slabs and nano-spheres at a magnification of x55000.

Table 6.1: EDS quantitative analysis on the VEW1 sample.

Element	C	O	Na	Mg	Si	Ca	V
Atomic %	23.52	36.99	7.95	1.09	16.91	1.98	11.57

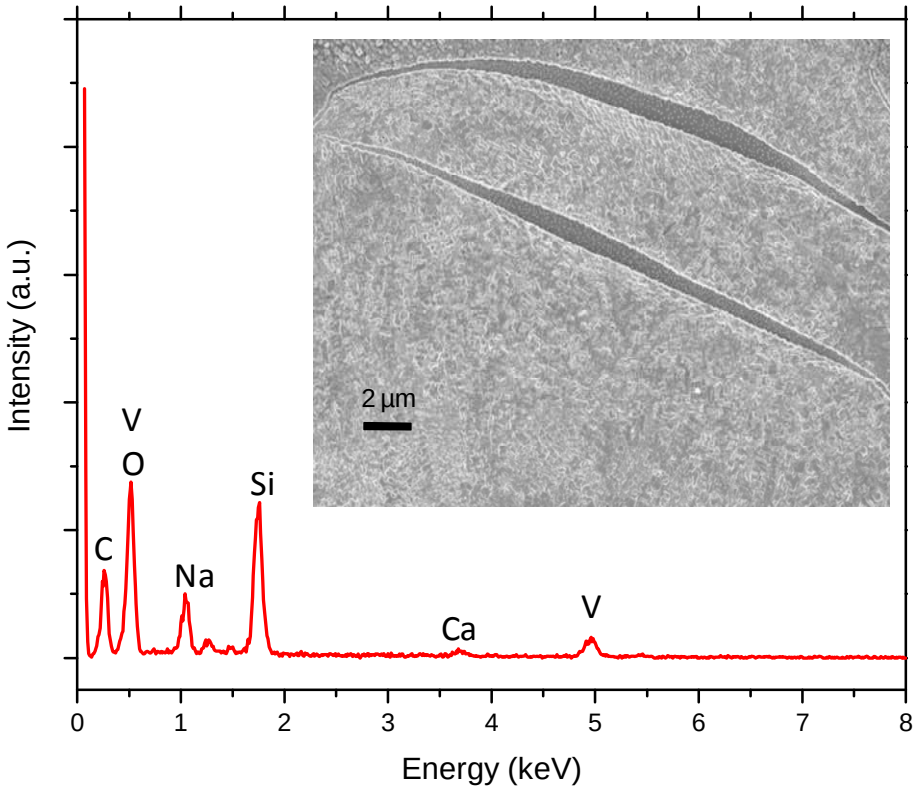

Figure 6.8: A SEM micrograph showing the morphology and the EDAX spectra of the VEW1 VO_{2-X} synthesized using a non-focused laser beam.

Sample VEP12 shows a similar morphology to sample VEW1 as shown in Figure 6.9 (a). The difference in this sample is that three types of morphologies are observed. Micro-sized islands shown in Figure 6.9 (b) reveal what seem to be agglomerated and crystalline particles with sizes in the micron range. Alongside

the islands, micro-sized “crystals” of different shapes are observed, Figure 6.9 (c). These “crystals” are also agglomerated. In between the “crystals” and the islands nanostructures are observed, Figure 6.9 (d), these nanostructures have different sizes and shapes.

Figure 6.10 (a) shows another area of the sample that has cracks. This area is rich with nano-rods and what looks like nano-spheres; Figure 6.10 (b), (c) and (d). The rods have an average diameter of 140 nm and an average length of 850 nm while the spheres have an average diameter of 100 nm. EDS analysis shows the same atoms as in Figure 6.6 and Figure 6.8.

Sample VB shows only one type of morphology throughout the sample. The sample also shows the smallest particles compared to samples VEW1 and VEP12. This means that the conditions, Table 5.3, used to synthesise these VO_{2-x} nanostructures are ideal. A high power density might be the reason for the different morphologies.

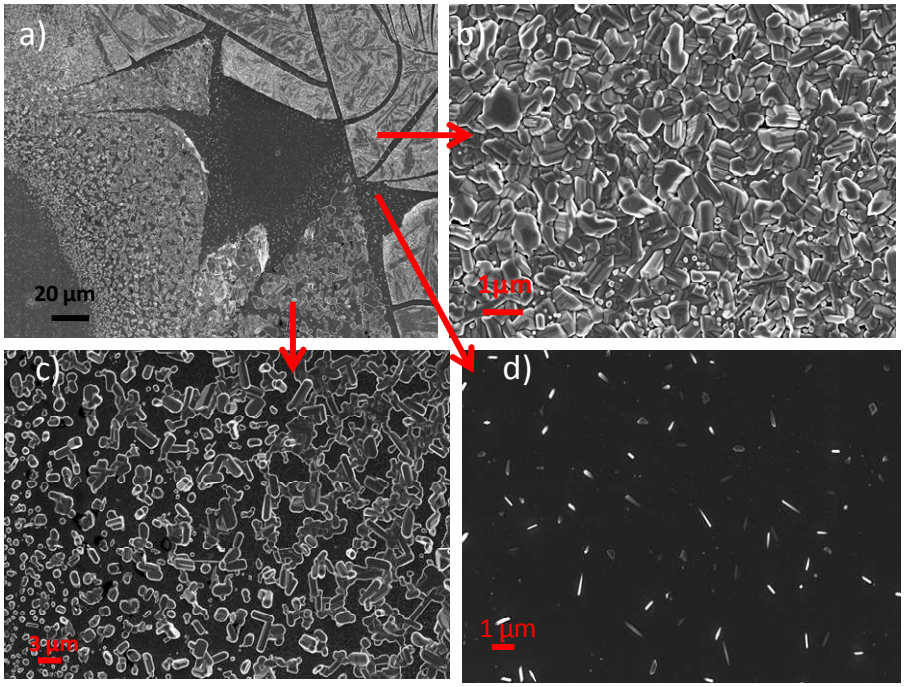

Figure 6.9: SEM micrographs of sample VEP12 VO_{2-x} structures (a) islands with cracks (b) surface of the island (c) “crystal” like structures and (d) nanostructures growing with each micro-crack.

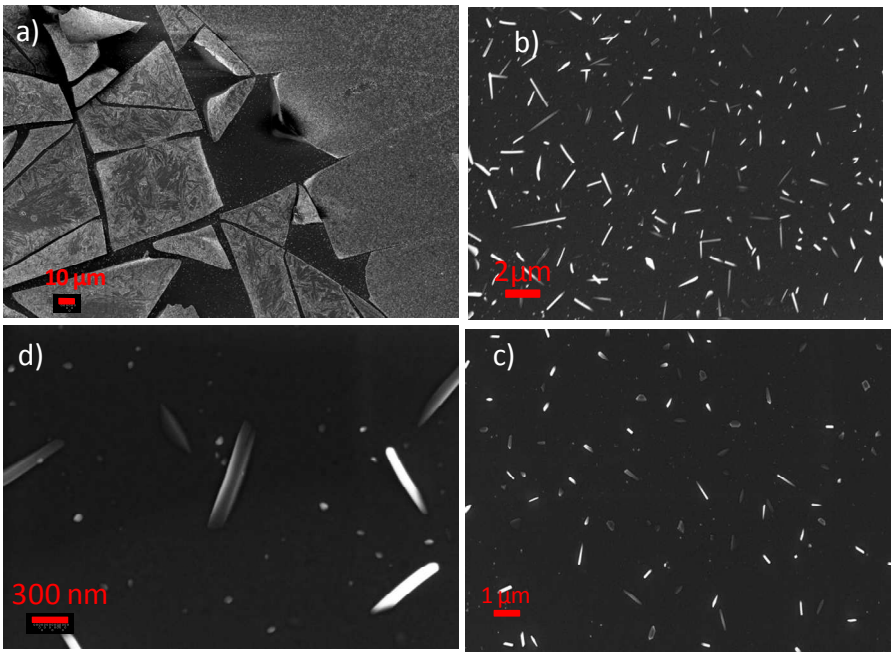

Figure 6.10: SEM micrographs of VO_{2-x} structures (a) islands with cracks (b) nano-rods at a magnification of x4500 (c) nano-rods at a magnification of x6250 and (d) nano-rods at a magnification of x23500.

6.4 Raman Spectroscopy

Raman spectroscopy is carried out using a Jobin–Yvon T64000 Raman spectrograph with a 514.5 nm line from an argon ion laser. The T64000 is operated in single spectrograph mode, with the 1800 lines/mm grating and a 20× objective on the microscope.

The Raman spectrum of sample VEP12, synthesized at a laser power of 65 W, showed bands at 175, 228, 261, 303, 422 and 532 cm^{-1}. Figure 6.11 show that the bands have high intensities. The 175, 228 and 303 cm^{-1} bands could be assigned to VO_2 (B) while the bands at 261 and 422 cm^{-1} could be assigned to β-V_2O_5. The peak at about 228 cm^{-1} is assigned to the low frequency modes of VO_2 while the characteristic peak of single silicon at 532 cm^{-1} is from the glass substrate. The 303 cm^{-1} band could be assigned to the external modes.

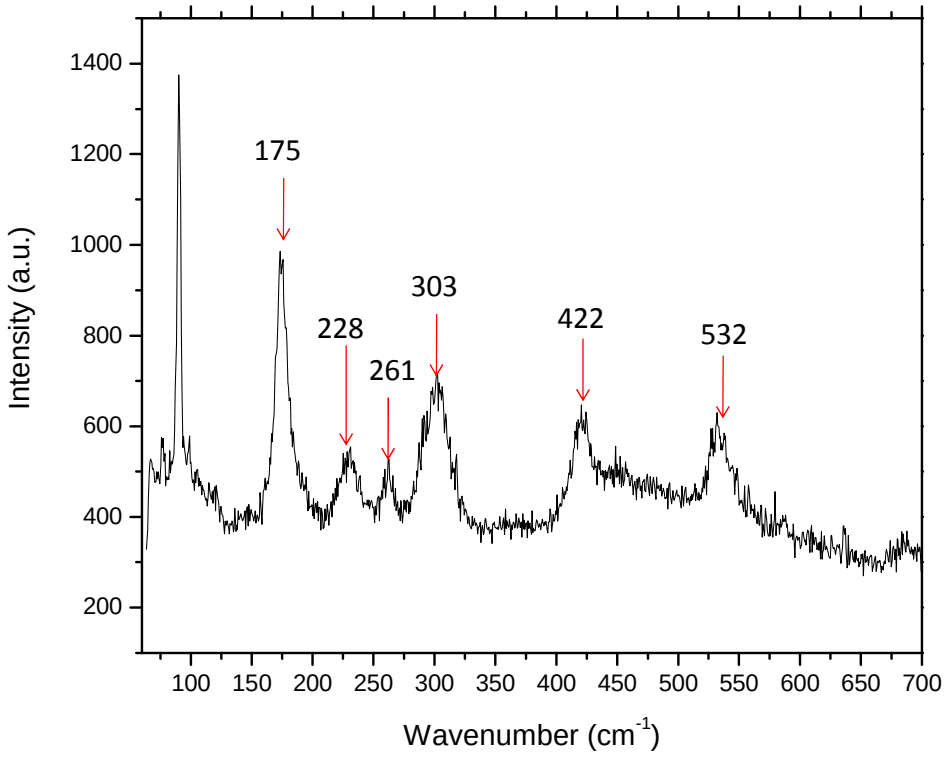

Figure 6.11: A Raman spectrum of sample VEP12 synthesized at a wavelength of 10.6 µm and power of 65 W.

Figure 6.12 shows a Raman spectrum of the VB sample. The weak spectral feature did not show any strong vanadium oxide signature. A similar rather structure less spectrum is also observed by Donev *et al* [55]. In their single-nanoparticle study the group measured the Raman response of 150 nm particles. They were unable, however, to detect a usable Raman signal from arrays of VO_2 nanoparticles smaller than about 100 nm in diameter. A scanning electron micrograph (SEM) of one such array on a silicon (Si) substrate is shown in Figure 6.13(a) and its Raman spectrum in Figure 6.13(b). Despite the long integration time (60 min) and relatively large average nanoparticles size (110 nm), only

Raman peaks belonging to the Si substrate stand out distinctly above the background. The weak spectral feature just below 200 cm^{-1}, while indeed attributable to the 195 cm^{-1} mode of VO_2, was indistinguishable from noise in the Raman spectra of arrays of smaller VO_2 nanoparticles. In fact, it was not until 125 nm nanoparticles were measured (not shown) that clear, though weak, VO_2 peaks emerged [55].

Raman scattering cross sections are typically 14–15 orders of magnitude smaller than fluorescence cross sections Raman scattering becomes increasingly less favourable for smaller nanoparticles, since their reduced volume and elastic scattering efficiency weaken the interaction with the pump light even further. However, electromagnetic field enhancements associated with the localized surface plasmons of noble-metal nanostructures can greatly increase the interaction strength between an analyte and optical radiation. In surface-enhanced Raman scattering (SERS), the analyte, which may even consist of single molecules, is placed within a few nanometers of or in contact with the signal enhancer (usually made of Ag or Au), which can be a roughened metal substrate, granular metal film, colloidally dispersed or lithographically patterned metal nanoparticles [55].

In our case the particles have an average diameter of 55 nm as shown in Figure 6.5. The same reasons presented by Donev *et al* (above) for their shape of the spectrum also apply to our Raman studies and spectra from samples with less than 100 nm particle sizes.

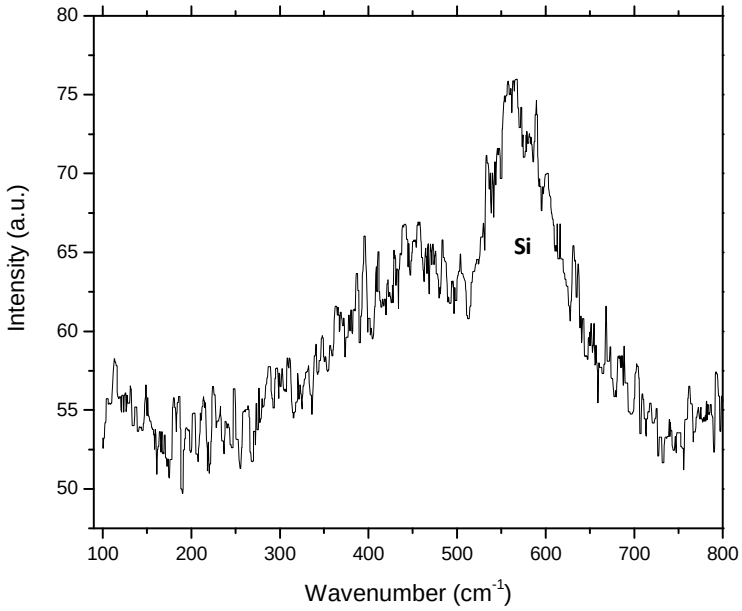

Figure 6.12: Raman spectrum of the VB sample.

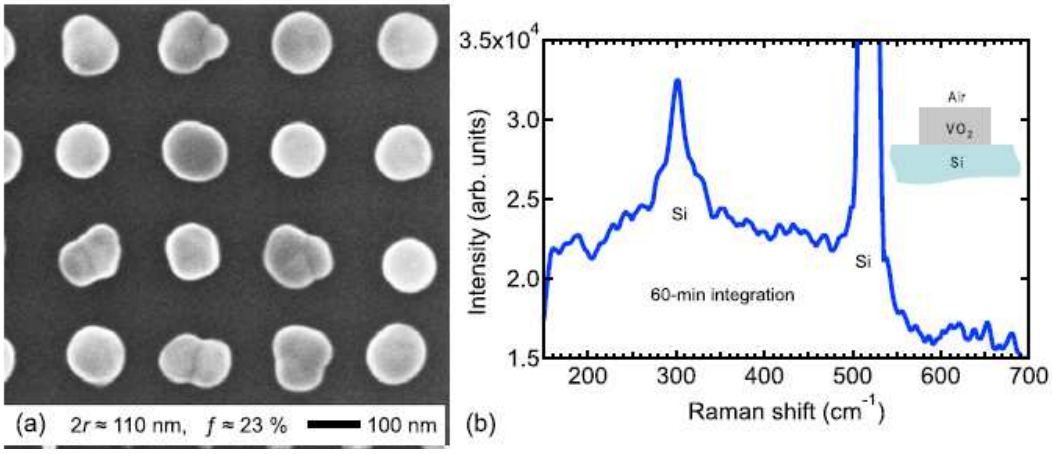

Figure 6.13: (a) SEM images (2r ≡ VO_2 NP diameter; f ≡ VO_2 areal coverage) and (b) a room-temperature Raman spectrum from arrays [55].

6.5 UV-VIS-NIR transmittance spectroscopy

Optical transmittance studies are performed on the samples synthesized under various conditions using a Varian Cary 500 UV–Vis–NIR spectrophotometer in the wavelength range from 200 nm to 3000 nm.

As a way of example, the film's optical transmittance (%) as a function of wavelength (nm) for the sample VEW1 synthesized at a wavelength of 9.22 µm, is shown in Figure 6.14. The sample exhibits thermochromism as can be seen in the different transmittance curves obtained at 25^{o}C and 70^{o}C. These show a rather small but clear difference in transmittance from the visible to the infrared regions. The sample displayed a lower optical transmittance within the visible region whereas the infrared region shows a higher transmittance at both 25^{o}C and 70^{o}C temperatures. It was also noted that the transmittance decreased in the visible and IR region as the temperature was increased.

Figure 6.15 shows the film's optical transmittance (%) as a function of wavelength (nm) of sample VEP12 which was grown with higher power intensity. A large amount of switching is observed compared to sample VEW1, Figure 6.15. The spectral transmittance of low temperature (25^{o}C) and high temperature (70^{o}C) shows a large difference in the visible and infrared (IR) region. The low temperature measurement shows a high transmittance in the infrared region of about 93 %. The value of the transmittance decreased to about 65 % upon the heating of the sample to 70^{o}C. The low temperature measurement also shows a sudden drop (from 82% to about78%) in the transmittance between the 800nm and 900 nm wavelength region. A similar drop in transmittance is also observed at

high temperature measurements, though not as pronounced as at 25°C. The visible region exhibits a lower optical transmittance which also decreases further as the temperature of the sample increases. The cause of the high transmittance could be due to the mixed phases of vanadium oxide in the sample.

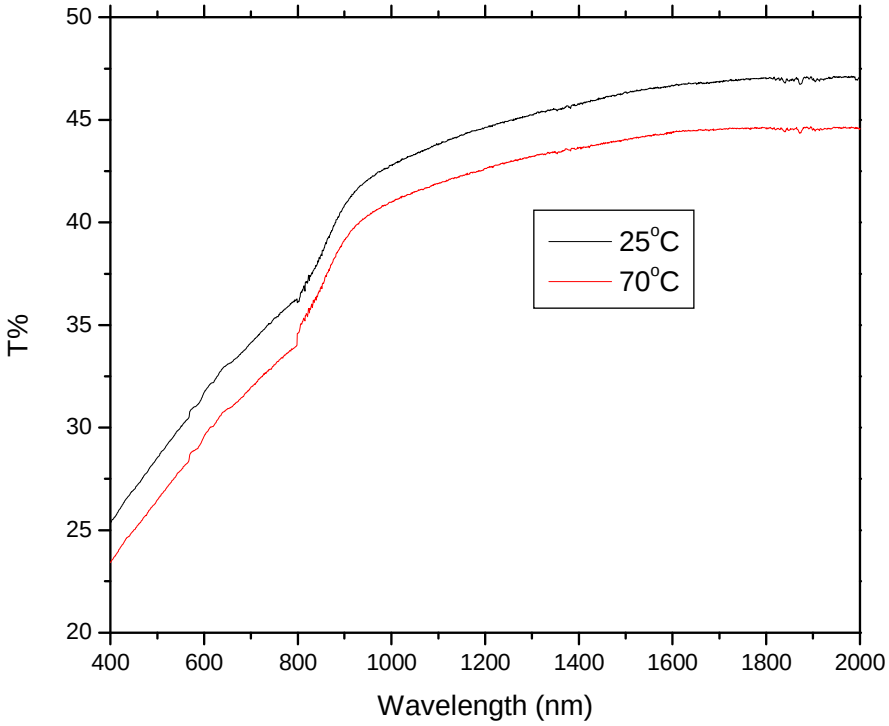

Figure 6.14: The optical transmission as a function of wavelength for the VEW1 sample at different temperatures.

The differences in the transmittance of samples VEW1 and VEP12 at different temperatures might be due to the different phases of the vanadium oxides indentified by the XRD. Sample VEW1, which was synthesized at a wavelength of 9.22 µm, was identified as VO_2 (B) by the XRD analysis and it exhibits a low

transmittance both at high and low temperatures compared to sample VEP12. Sample VEP12, which is synthesized at a power of 65 W, is identified as a mixture of β-V_2O_5 and VO_2 (B) from the XRD analysis and exhibits a high transmittance compared to sample VEW1. This mixture might be the reason for a high transmittance.

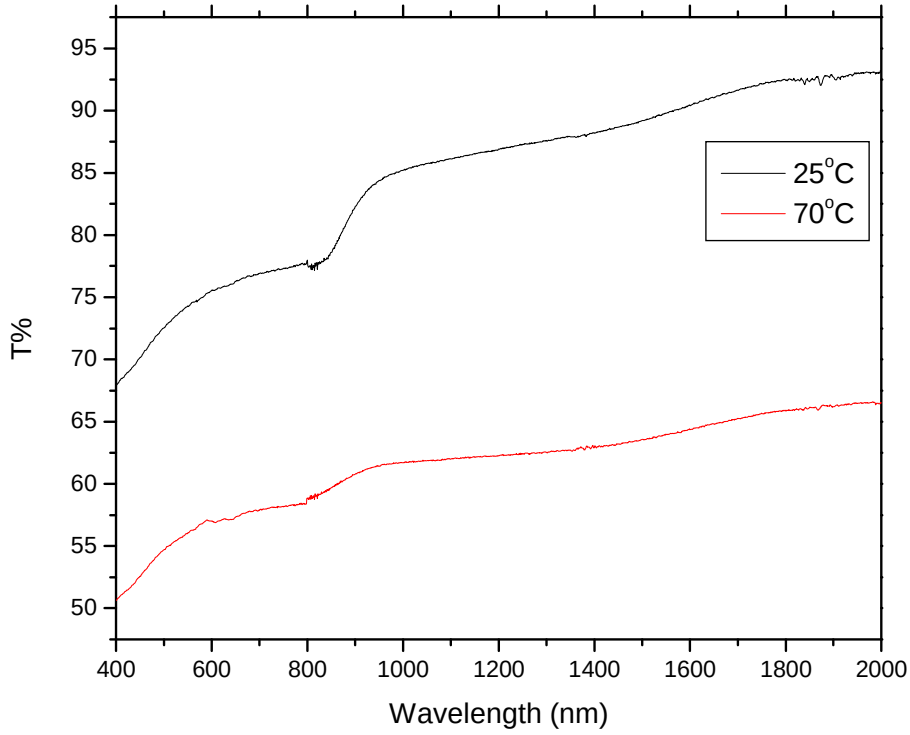

Figure 6.15: The optical transmission as a function of wavelength for the VEP12 sample at different temperatures.

Figure 6.16 shows the film optical transmittance (%) as a function of wavelength (nm) of the sample VB, which is grown using a focused laser beam. The spectral transmittance of low temperature (25°C) and high temperature (70°C) shows a difference in the visible and infrared (IR) region. The low temperature measurement shows a high transmittance in the infrared region while the high

temperature measurement shows a slightly lower transmittance in the infrared and visible region. It must be noted that the features in the 800 nm and 1200 nm are not absorption peaks but are merely features caused by the instrument as the detectors change.

The VB spectrum resembles that of the VEW1 sample. This is expected as both samples are identified as VO_2 (B). In this case the differences in the transmittance might be caused by the morphology of the samples.

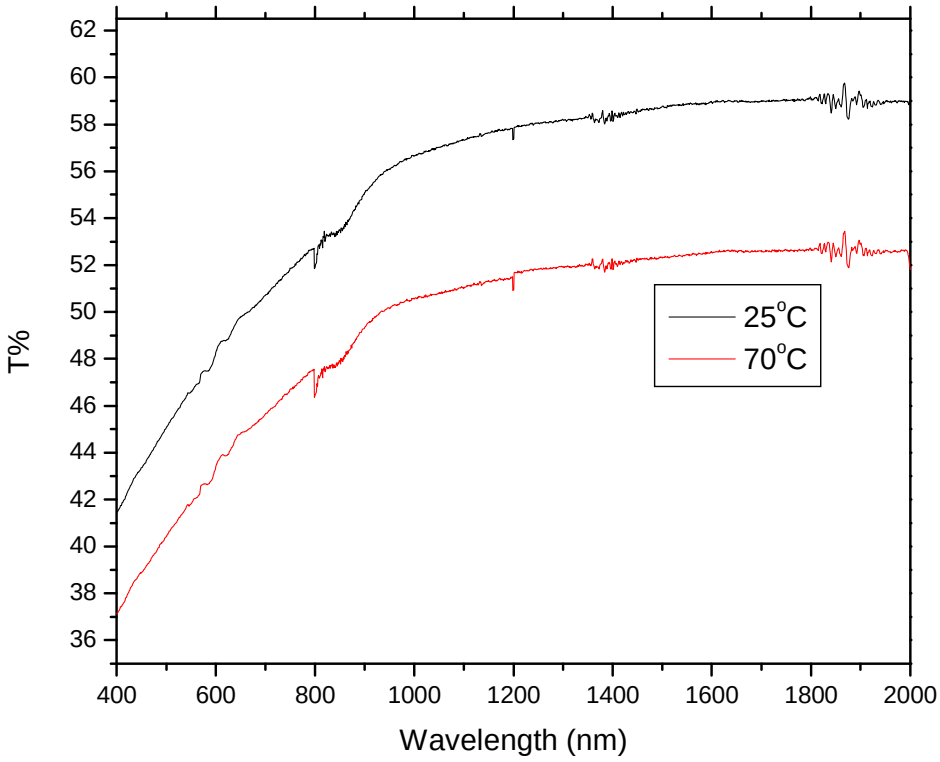

Figure 6.16: The optical transmission as a function of wavelength for the VB sample at different temperatures.

Chapter 7: Conclusion and future work

7.1 Summary

In this study the synthesis of vanadium oxide nano-structures was carried out using laser pyrolysis technique. The focus was on making VO_{2-x} depositions using various laser pyrolysis parameters and establish in this way (1) an optimum laser wavelength threshold for the photon induced dissociation of the molecular precursors while the thermal contribution was kept minimal by using low power density (laser energy of 30 W) and (2) the lower threshold for pure thermal contributions by working with wavelengths far from resonance in order to minimise pure photon induced contributions. In addition, VO_{2-x} nano-particles were synthesized using similar laser pyrolysis conditions as Mwakikunga *et al* [17] at much higher power density. A total number of 21 samples were produced and annealed at 500^{o}C in an argon atmosphere for 17 hours.

A high wavelength threshold of 9.22 µm has been discerned at which the XRD spectra of the VEW set exhibits clear peaks of interest at $2\theta=29.1^{o}$ and $2\theta=44.3^{o}$ corresponding to the VO_2 (B) compound.

The XRD analysis for the VEP set, where the power density started to increase from very low values (~16 W/cm2), has pointed out a lower power density threshold for the pure thermally induced dissociation occurring at ~110 W/cm2. At this power density the spectra begin to show relevant peaks of interest at $2\theta=12.5^{o}$ and $2\theta=18.4^{o}$ corresponding to β-V_2O_5 while the $2\theta=29.1^{o}$ peak

observed corresponds to the VO_2 (B). This sample, at around the lower power density threshold, show also mixed phases of vanadium oxide.

Interestingly, from morphological point of view, VO_{2-x} nano-structures have been observed in all samples VEW1, VEP12 and VB irrespective of power density and wavelength. At the highest wavelength threshold (sample VEW1) showed micro-sized cracks (average size of 100µm) with nano-structures inside the cracks have been observed. These nano-structures have different morphologies such as nano-rods (70 nm), nano-slabs and nano-spheres which in many respects are different to VO_2 nanostructures observed by other groups. At the lower power density threshold (sample VEP12) micro-sized cracks have also been the dominant morphological feature with existing nano-rods of average size 140 nm and nano-spheres of (average size of 100 nm) inside the cracks. At the high power density regime (sample VB) a rather uniform film with nano-rods of an average diameter of 55 nm dispersed throughout the sample is formed. The structures were determined by using the LEO 1525 field emission scanning electron microscope (SEM).

Raman spectroscopy on the samples VEW1, VEP12 and VB showed some correlation to the XRD results. Samples VEW1 and VEP12 showed bands at the 175, 228 and 303 cm^{-1} which corresponds to the VO_2 (B) bands. Sample VEP12 showed additional bands at 261 and 422 cm^{-1} which correspond to the β-V_2O_5.

The Raman spectrum at the high power density sample is mostly featureless. This confirms similar results of Donev *et al* and it is attributed to the very small particle size of the nano-structures.

The optical transmittance studies regarding the VEW1, VEP12 and VB samples were performed using the Varian Cary 500 UV–Vis–NIR spectrophotometer. Samples VEW1, VEP12 and VB showed a decrease in transmittance in the visible and IR region as the temperature was increased from 25^{o}C to 70^{o}C. VEP12 showed a greater transmittance than VEW1 and VB. Measurements at 25^{o}C showed a sudden decrease in transmittance between the 800nm and 900 nm wavelength region for the VEP12 sample. This feature smoothed out at 70^{o}C measurements.

7.2 Future work

The high power density (2.2 kW/cm^{2}) and slow flow rates have shown the potential of synthesizing uniform and nano-structured material as in sample VB. One of the aspects that could be investigated is the effect of even higher power densities to assess the relation of the uniformity of the film to the stoichiometry of the product and the size of the product.

Since our heating stage was designed to reach a temperature of 80^{o}C, we could design another heating stage that could reach negative temperatures. This could be used to study the transition temperature of the VB sample. Once the transition temperatures are known possible applications in sensors and devices can be identified.

Appendix A

List of publications

International conference peer reviewed papers

1. Lerato Shikwambana, Malcolm Govender, Bonex Mwakikunga, Elias Sideras-Haddad, and Andrew Forbes (2011), A review of the laser pyrolysis technique used to synthesize vanadium and tungsten oxide thin films, *Advanced Materials Research*, vol. 227, pp 80-83.

National conference peer reviewed papers

1. Lerato Shikwambana, Malcolm Govender, Bonex. Mwakikunga, Andrew Forbes, and Elias Sideras-Haddad (2010), Optimization of the laser pyrolysis parameters to synthesis vanadium oxide (VO_{2+x}) nanostructures, *In proceedings of 55nd South African Institute of Physics Conference, Condensed matter Physics and Material Science.*

Other publications

1. Malcolm Govender, Lerato Shikwambana, Bonex Wakufwa Mwakikunga, Elias Sideras-Haddad, Rudolph Marthinus Erasmus and Andrew Forbes (2011), Formation of tungsten oxide nanostructures by laser pyrolysis: stars, fibre and spheres, *Nanoscale research letters*, vol. 6, no. 166, pp. 1-8

Bibliography:

[1] Hornyak, G.L., Dutta, J. , Tibbals, H.F. and Rao, A.K. (2008), Introduction to Nanoscience, CRC Press, Boca Raton, FL

[2] Tomalia, D.A. (2009), In quest of a systematic framework for unifying and defining nanoscience, *Journal of Nanoparticle Research*, vol. 11, pp 1254-1310

[3] Poople Jr., C.P. and Owens, F.J. (2003), Introduction to nanotechnology, John wiley & sons, Inc

[4] Dick, A. K. (2008), A review of nanowire growth promoted by alloys and non-alloying elements with emphasis on Au-assisted III-V nanowires, *Progress in Crystal Growth and characterization of Materials*, vol. 54, pp. 138-173

[5] Blind, K., Gauch, S. (2009), Research and standardisation in nanotechnology: evidence from Germany, *Journal of Technology Transfer*, vol. 34, no. x, pp 320-342

[6] Kostoff, R. N., Koytcheff, R.G. and Lau, C.G. Y. (2007), Global nanotechnology research literature overview, *Technological Forecasting & Social Change*, vol. 74, pp. 1733–1747

[7] Cele, L.M., Ray, S.S. and Coville, N.J. (2009), *South African Journal of Science*, vol. 105, no. 7/8, pp. 242

[8] http://www.sani.org.za/pdf/Nanotechnology_10-Year_plan.pdf

[9] http://www.mbendi.com/indy/ming/vand/af/sa/p0005.htm

[10] Hagrman D., Zubieta, J., Warren, C. J., L. M. Meyer, Treacy, M. M. J. and Haushalter, R. C. (1998), A New Polymorph of VO_2 Prepared by Soft Chemical Methods, *Journal of solid state chemistry*, vol 138, pp. 178-182

[11] Grygiel, C., Pautrat, A., Sheets, W. C., Prellier, W., Mercey, B. and M`echin, L. (2008), Mesoscopic electronic heterogeneities in the transport properties of V_2O_3 thin films, *Journal of physics: Condensed matter*, vol. 20, pp. 472205 (6pp)

[12] Filonenko, V.P., Sundberg, M., Werner, P.-E, and Zibrov, I. P. (2004), Structure of a high-pressure phase of vanadium pentoxide, β-V_2O_5, *Acta Crystallographica Section B: Structural Science*, vol. 60, pp. 375-381

[13] Nag, J and Haglund Jr, R. F. (2008), Synthesis of vanadium dioxide thin films and nanoparticles, *Journal of Physics: Condensed Matter*, vol. 20, pp. 264016 (14pp)

[14] Baum, P., Yang, D.-Y. and Zewail, A. H. (2007), 4D Visualization of Transitional Structures in Phase Transformations by Electron Diffraction, *Science*, vol. 318, pp. 788-792

[15] Peng, Z., Wung, Y., Du, Y., Lu, D. and Sun, D. (2009), Phase transition and IR properties of tungsten-doped vanadium dioxide nanopowders, *Journal of Alloys and Compounds*, vol. 480, pp. 537-540

[16] Lopez, R., Boatner, L.A., Haynes, T.E, Feldman, L.C. and Hugland, R. (2002), Synthesis and characterization of size-controlled vanadium dioxide nanocrystals in a fused silica matrix, *Journal of Applied Physics*, vol. 92, pp. 4031-4036

[17] Mwakikunga, B.W., Sideras-Haddad, E., Forbes, A., and Arendse, C. (2008), Raman spectroscopy of WO_3 nano-wires and thermo-chromism study of VO_2 belts produced by ultrasonic spray and laser pyrolysis techniques, *Physica Status Solidi a*, vol. 205, pp. 150–154

[18] Hong-Tao, Y., Ke-Cheng, F., Xue-Jin, W., Chao, L., Chen-Juan, H. and Yu-Xin, N., (2004), Effect of nonstoichiometry on Raman scattering of VO_2 films, *Chinese Physics B*, vol. 13, no. 1, pp. 82 -84

[19] Rama, N., and Ramachandra Rao, M.S. (2010), Synthesis and study of electrical and magnetic properties of vanadium oxide micro and nanosized rods grown using pulsed laser deposition technique, *Solid State Communications*, vol. 150, pp. 1041-1044

[20] Wang, Y.L., Li, M.C. and Zhao, L.C. (2007), The effects of vacuum annealing on the structure of VO_2 thin films, *Surface & Coatings Technology*, vol. 201, pp 6772-6776

[21] Crnjak, Z.O and Musevic, I. (1999), Characterization of vanadium oxide and new v/ce oxide films prepared by sol-gel process, *Nanostructured Materials*, vol. 12, pp. 399-404

[22] Negra, M.D., Sambi, M. and Granozzi, G. (2001), Electronic properties and structure of vanadia ultra-thin films grown on TiO_2(1 1 0) in a water vapour ambient, *Surface Science*, vol. 494, pp. 213-228

[23] Kim, D.H. and Kwok, H.S. (1994), Pulsed laser deposition of VO_2 thin films, *Applied Physics Letters*, vol. 65, pp. 3188-3190

[24] Vernardou, D. Pemble, M.E. and Sheel, D.W (2006), The Growth of Thermochromic VO_2 Films on Glass by Atmospheric-Pressure CVD: A Comparative Study of Precursors, CVD Methodology, and Substrates, *Chemical Vapour Deposition*, vol. 12, pp. 263-274

[25] Haggerty, J.S. and Cannon, W.R. (1981), in:J.I Steinfield (Ed), *Laser Induced Chemical processes*, Plenum Press,New York, p165

[26] Alexandrescu, R., Morjan, I., Dumitrache, F., Scarisoreanu, M., Soare, I., Fleaca, C., Birjega, R., Popovici, E., Gavrila, L., Prodan, G., Ciupina, V., Filoti, G., Kuncser, V. and Vekas, L. (2008), Photochemistry Aspects of the Laser Pyrolysis Addressing the Preparation of Oxide Semiconductor Photocatalysts, *International Journal of Photoenergy*, article ID 604181, pp. 11, doi:10.1155/2008/604181

[27] Mwakikunga, B.W. (2010) *Nano-size effects on opto-electronic, structural and vibrational properties of vanadium and tungsten oxides produced by laser and ultrasonic spray pyrolysis techniques*, Phd thesis, University of the Witwatersrand, p 102

[28] Sublemontier, O., Lacour, F., Leconte, Y., Herlin-Boime N., and Reynaud, C. (2008), CO_2 laser-driven pyrolysis synthesis of silicon nanocrystals and applications, *Journal of Alloys and Compounds* , vol. 483, pp.499-502

[29] Mwakikunga, B.W., Forbes, A., Sideras-Haddad, E., Erasmus, R.M., Katumba, G. and Masina, B. (2008), Synthesis of tungsten oxide nanostructures by laser pyrolysis, *International Journal of Nanoparticles*, vol 1, no.3, pp. 185-202

[30] Alexandrescu, R., Dumitrache, F., Mojan, I., Sandu, I., Savoiu, M., Voicu, I., Fleaca, C. and Piticescu, R. (2004), TiO_2 nanosized powders by $TiCl_4$ laser pyrolysis, *Nanotechnology*, vol 15, pp. 537-545

[31] Galvez, A., Herlin-Boime, N., Reynaud, C., Clinard, C. and Rouzaud, J. (2002), Carbon nanoparticles from laser pyrolysis, *Carbon*, vol 40, pp. 2775-2789

[32] Peters, G., Jerg, K. and Schramm, B. (1998), Characterization of chromium (III) oxide powders prepared by laser-induced pyrolysis of chromyl chloride, *Materials Chemistry and Physics*, vol 55, pp. 197-201

[33] Alexandrescu, R., Morjan, I., Voicu, I., Dumitrache, F., Albu, L., Soare, I. and Prodan, G. (2005), Combining resonant/non-resonant processes: Nanometer-scale iron-based material preparation via CO_2 laser pyrolysis, *Applied surface science*, vol. 248, pp. 138-146

[34] Bomatí-Miguel, O., Zhao, X. Q., Martelli, S., Di Nunzio, P.E. and Veintemillas-Verdaguer, S. (2010), Modeling of the laser pyrolysis process by means of the aerosol theory: Case of iron nanoparticles, *Journal of Applied Physics*, vol. 107, pp. 7, doi:10.1063/1.3273483

[35] Forster, J., von Hoesslin, M. and Ulenbusch, (1996), Temperature measurements in CO_2-1aser-induced pyrolysis flames for SiC and ternary SiC/C/B powder synthesis by means of CARS, *Applied Physics B: Lasers and Optics*, vol. 62, pp. 609-612

[36] Andrews, D.L. (1997), *Lasers in Chemistry*, 3rd, Springer

[37] Mott, N. F. (1974), *Metal-insulator transitions*, Taylor & Fransis Ltd

[38] Kittel, C. (1970), *Introduction to Solid State Physics*, 3rd, Wiley

[39] Mott, N. F. and Davis, E. A. (1979), *Electronic Processes in non-crystalline materials*, 2nd, Oxford university press

[40] Cyrot, M. (1971), Theory of Mott transition: Applications to transition metal oxides, *Le Journal de physique*, Tome 33, pp. 125-134

[41] Eyert, V. (2002), The metal transition of VO_2: A band theoretical approach, *Annals Physics*, vol. 11, pp. 650-702

[42] Mwakikunga, B. W., Sideas-Haddad, E., Forbes, A., Katumba, G., Sinha Ray, S. and Arendse, C. (2009), Thermo-chromism at nanoscale, *Applied science innovations Pvt. Ltd*, (book chapter in press)

[43] http://sitemason.vanderbilt.edu/files/hb9eSI/qual.pdf

[44] Silfvast, W. T. (2004), *Laser Fundamentals 2nd ed*, Cambridge University Press

[45] Siegman, A. E. (1986), *Lasers*, University Science books

[46] Csele, M. (2004), *Fundamentals of light source and lasers*, John Wiley & sons, Hoboken, New Jersey

[47] Chapple, P. B. (1974), Beam waist and M2 measurement using a finite slit, *Optical Engineering*, vol. 33, pp 2461-2466

[48] Watt, I. M. (1985), *The principles and practice of electron microscopy*, Cambridge University Press

[49] Egerton, R. F. (2005), *Physical principles of electron microscopy*, Springer Science+Busssiness Media, Inc

[50] Long, D. A. (1977), *Raman Spectroscopy*, McGraw-Hill, Inc

[51] Lappalainen, J., Heinilehto S., Jantunen H.and Lantto, V. (2009), Electrical and optical properties of metal-insulator-transition VO_2 thin films, *Journal of electroceramics*, vol. 22, pp. 73–77

[52] Batistaa, C, Teixeirab, V. and Carneiro, J. (2008), Structural and Morphological Characterization of Magnetron Sputtered Nanocrystalline Vanadium Oxide Films, *Journal of Nano Research*, vol. 2, pp. 21-30

[53] Zou, C. W, Yan, X. D., Han, J., Chen, R.Q. and Gao, W. (2009), Microstructures and optical properties of β-V_2O_5 nanorods prepared by magnetron sputtering, *Journal of Physics D: Applied Physics*, vol. 42, pp. 145402

[54] Oka, Y., Yaob, T. and Yamamotoa, N. (1991), Structural Phase Transition of VO_2 (B) to VO_2 (A), *Journal of Materials Chemistry*, vol. 1, pp. 815-818

[55] Donev, E. U., Ziegler, J. I., Haglund Jr, R. F. and Feldman, L. C. (2009), Size effects in the structural phase transition of VO_2 nanoparticles studied by surface-enhanced Raman scattering, *Journal of optics A: pure and applied optics*, vol. 11, pp. 125002

Advanced Materials Research Vol. 227 (2011) pp 80-83
Online available since 2011/Apr/19 at www.scientific.net

doi:10.4028/www.scientific.net/AMR.227.80

A Review of the Laser Pyrolysis Technique Used to Synthesize Vanadium and Tungsten Oxide Thin Films

SHIKWAMBANA Lerato [1, 2, a], GOVENDER Malcolm [1, 2, b], MWAKIKUNGA Bonex [1, 4, c], SIDERAS-HADDAD Elias [2, d] and FORBES Andrew [1, 2, e]

[1] CSIR National Laser Centre, P. O. Box 395, Pretoria 0001, South Africa

[2] School of Physics, University of Witwatersrand, Private Bag 3, PO Wits 2050, Johannesburg, South Africa

[3] School of Physics, University of KwaZulu-Natal, Private Bag X54001, Durban 4000, South Africa

[4] Department of Physics and Biochemical Sciences, The Polytechnic, University of Malawi, Private Bag 303, Chichiri, Blantyre 3, Malawi

[a] lshikwambana@csir.co.za, [b] mgovender2@csir.co.za, [c] bmwakikunga@csir.co.za,

[d] Elias.Sideras-Haddad@wits.ac.za, [e] aforbes1@csir.co.za

Keywords: laser pyrolysis, thin films, nanostructure, interaction volume

Abstract. Laser pyrolysis is one of the most important and emerging techniques used to synthesize thin films, nano-powders and nano-structured materials. The advantages in this technique include: a well defined interaction volume, no interactions with the reactor chamber walls hence less impurities, and the attainment of very fine particles. In this paper we briefly review the development and the current status of laser pyrolysis world wide. However, the main focus is an overview of our efforts to synthesize vanadium and tungsten oxides using this technique since 2006. We discuss the role of the laser pyrolysis parameters: the beam waist, interaction volume, carrier gas flow rates, laser wavelength and power density on the phase, size and shape of the final products obtained.

Introduction

Laser pyrolysis (LP) is a modern technique used to synthesize thin films and nano-structured materials. The first use of this technique was reported by Bachmann *et.al* [1] in 1975 where they synthesized Boron trichloride (BCl_3). In 1981 Haggerty *et al* introduced the laser pyrolysis parameters and synthesized silicon nano-powder. A group in 1984 used the laser pyrolysis technique to study the gas-phase thermal decomposition of iron pentacarbonyl $Fe(CO)_5$, chromium hexacarbonyl $Cr(CO)_5$, molybdenum hexacarbonyl $Mo(CO)_5$ and tungsten hexacarbonyl $W(CO)_6$ [2]. This highlights the versatility of the technique as a synthesizing and analytical technique. In this paper we discuss the LP technique as a synthesizing method.

Laser pyrolysis of organometallic gas and liquid phases have be used for the synthesis of TiO_2 [3], FeSi [4], Fe_2O_3 [5], VO_2 [6] and WO_3 [7] nanoparticles. VO_2, WO_3 thin films and nanostructures are of interest because of their applications in gas sensors, fireproofing fabrics [8], thermochromic coatings, optical and holographic storage, fiber-optical switching devices, laser scanners, missile training systems and ultra-fast optical switching devices [9,10].

In this paper we discuss the development of the LP technique in synthesizing thin films and nano-structured materials. We review some of the important laser pyrolysis parameters used to synthesize nano-structured materials. We then conclude the discussion by reviewing our work in synthesizing VO_2 and WO_3 thin films. Recently, work to model the synthesis of nano-structures by laser pyrolysis is being investigated by Amara *et al*.

Laser pyrolysis publications

Nanotechnology is seen to have many applications in areas such as electronics, telecommunications, data processing, biotechnology, precision technology and material science [11]. Research on nanotechnology is growing rapidly with publications growing from 11 265 in 1991 to 64 737 in 2005 [12], shown in Fig.°1a). A majority of the nano-structured materials are synthesized using conventional methods such as sputtering [13], sol-gel [14], evaporation [15], pulsed laser deposition [16], chemical vapour deposition [17] and ion implantation [9]. Only a few publications on the laser pyrolysis technique have been made, as shown in Fig.°1b). The graph shows a steady increase in the number of publications each year and highlights the LP technique as an alternative method of synthesis compared to the conventional methods.

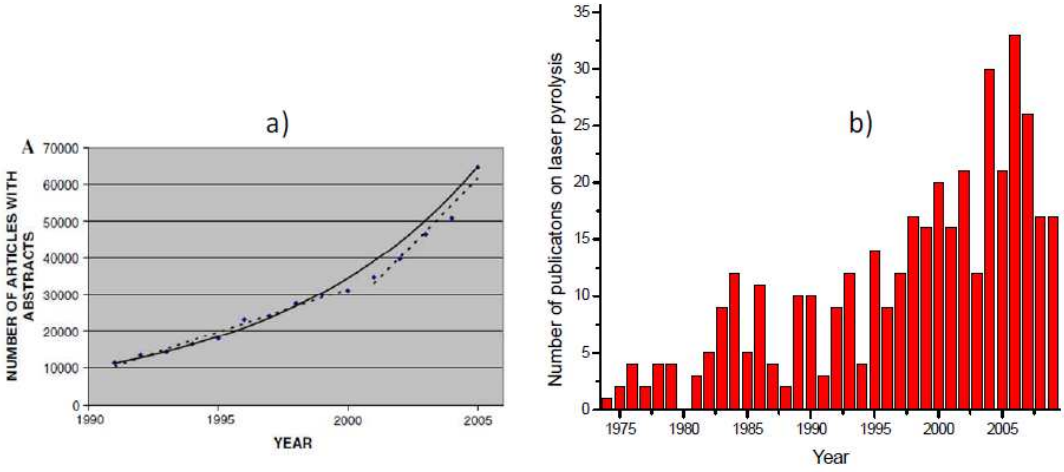

Fig.°1a) Science Citation Index (SCI) and Social Sciences Citation Index (SSCI) articles versus time total records retrieved [12] and b) Annual publications on laser pyrolysis

Process description

In the past laser pyrolysis was used to synthesize nano-powder [18], but now people use this technique to synthesize thin films [19] and nano-particles [20]. A typical schematic layout of the experiment, Fig.°2a), has a CO_2 laser, a reaction chamber, a nozzle and carrier gases. Most experiments use a continuous wave (cw) CO_2 laser but other people have reported the use of a pulsed CO_2 laser [21]. The main reason for using a CO_2 laser is based on the resonance between the emission of the laser at 10.6 μm and the absorption of at least one of the precursors [22]. The precursors can be in a gas phase [22] and/or in a liquid phase [23] but this does not affect the final product being produced. The controllable experimental parameters that affect the final products are: power density, reactor pressure and the flow rate. This parameters influence the temperature inside the chamber [24, 25]. The temperature can be determined by a contact method using a pyrometer (thermocouple) [18], but this method does not provide an accurate temperature value, and by a non-contact method using the scanning coherent anti-Stokes Raman scattering (CARS) method [26]. An accurate description of the reaction zone, Fig°2b), is useful since it can provide analytical models such as gas heat transfers, kinetics, chemistry and fluid flow [18].

WO_3 and VO_2 nano-structures

As mentioned earlier, laser pyrolysis has been used to produce various nano-structured materials and Mwakikunga *et al* [7] where the first group to report on the synthesis of WO_3 nano-wires using

this technique, Fig°3a). The group derived a reaction zone expression [7] and showed that the contributing laser parameters to the reaction zone are: the laser wavelength, laser beam quality and laser beam waist. The group reported that a reaction zone of 4 cm^3, a power density of 2.2 kW/cm^2

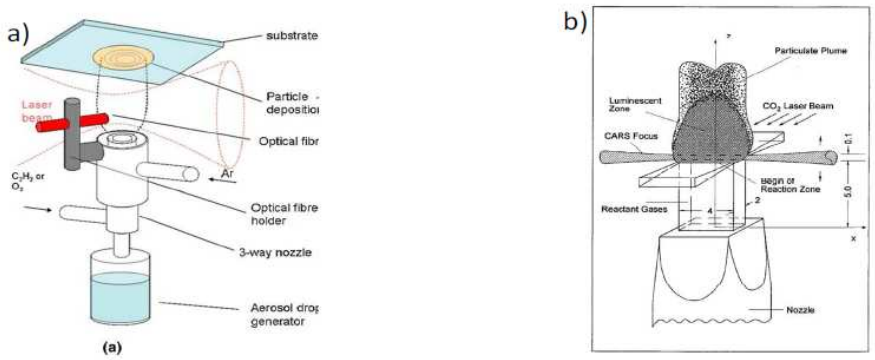

Fig. 2a) A Schematic diagram of the laser pyrolysis layout when the precursor flow rate is larger than the flow rate of the carrier gas [27] and b) is a schematic of the reaction zone [26]

and a beam waist 1.2 mm is sufficient for synthesizing WO_3 nano-wires. They also proposed a growth mechanism for the nano-wires length which they called the "solid-vapour-solid (SVS)" mechanism [27] where thermal annealing was the main driving mechanism [28]. Further work was carried out to synthesize VO_2 nano-belts, Fig°3b), using the same conditions. The group concluded that the LP technique has a potential to improve the optical, photonic and electrical/electronic properties of materials [6].

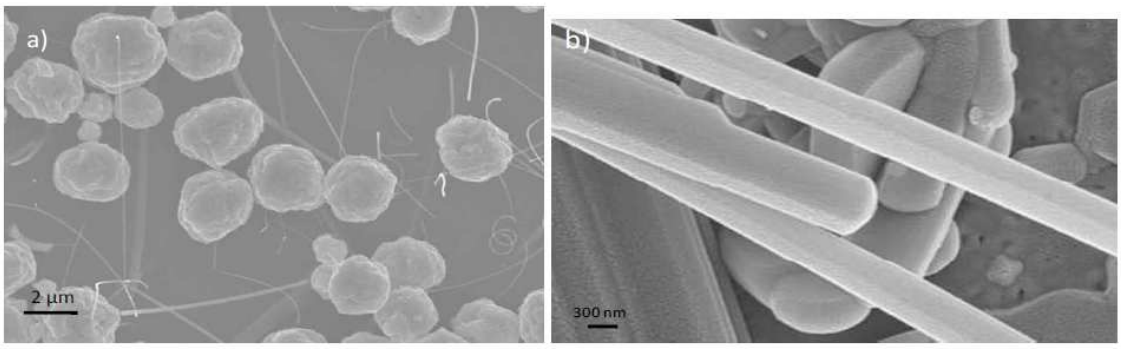

Fig.3a) A SEM micrograph of WO_3 nano-wires [7] and Fig. 3b) a SEM micrograph of VO_2 nano-belts [6]

Conclusion and future outlook

Laser pyrolysis has proven to be a clean method with no contaminations when synthesizing nano-structured material, thus this makes it an ideal method of synthesis. This review also showed that the laser pyrolysis parameters optimization depends on the type of materials being produced; different materials will be optimized differently.

Since the synthesizing method is understood, an area that still needs to be investigated is the measurement of temperature of the flame using non-contact methods. The determination of the temperature will lead to an understanding of the nano-particles formation.

References

[1] H. R. Bachmann, H. Noth, R. Rinck, K. S. Kompa: Chem. Phys. Lett. Vol. 29 (1975), p.627

[2] K. E. Lewis, D. M. Golden and G. P. Smith: J. Am. Chem. SOC. Vol. 106 (1984), p. 3905

[3] R. Alexandrescu, I. Morjan, I. Voicu, F. Dumitrache, I. Sandu, M. Savoiu, C. Fleaca and R. Piticescu: Nanotechnology Vol. 15 (2004), p. 537
[4] S. Martelli, O. Bomati-Miguel, L. De Dominics, R. Giorgi, F. Rinaldi and S. Veintemillas-Verdaguer: Appl. Surf Scien. Vol. 186 (2002), p. 562
[5] E. Popovici , F. Dumitrache, I. Morjan, R. Alexandrescu,V. Ciupina , G. Prodan, L. Vekas, D. Bica,O. Marinica, E. Vasile : Appl. Surf. Scien. Vol. 254 (2007), p. 1048
[6] B.W. Mwakikunga, E. Sideras-Haddad, A. Forbes, and C. Arendse: Phys. Stat. Sol. (a) Vol. 205 (2008), p. 150
[7] B.W. Mwakikunga, A. Forbes, E. Sideras-Haddad, R.M. Erasmus, G. Katumba, and B. Masina: Int.J. Nanoparticles, Vol. 1, No.3 (2008)
[8] W. J. Lee: J. Elect. Mat Vol. 29 (2006) , p. 183
[9] R. Lopez, L. A. Boatner, T. E. Haynes, L. C. Feldman and R. F. Haglund, Jr.: J. Appl Phys., Vol. 92, No.7, (2002)
[10] J. Nag and R.F. Haglund Jr: J. Phys. Condens. Matter 20, (2008), p. 264016.
[11] K. Blind and S. Gauch: J. Technol. Transf. Vol. 34 (2009), p. 320
[12] R. N. Kostoff, R. G. Koytcheff and C. G.Y. Lau: Technological Forecasting & Social Change Vol. 74 (2007), p. 1733
[13] Y.L. Wang, M.C. Li and L.C. Zhao: Rare Met. Mater. Eng. Vol. 7 (2005), p. 1077
[14] Z.O. Crnjak and I. Musevic: Nanostrct. Mater. Vol. 399, (1999)
[15] M.D. Negra, M. Sambi and G. Granozzi: Surf. Sci. Vol. 494 (2001), p. 213
[16] D.H. Kim and H.S. Kwok : Appl. Phys. Lett. Vol. 65 (1994), p. 3188
[17] D.Vernardou, M.E. Pemble and D.W Scheel: Chem. Vap. Deposit. Vol. 12 (2006), p. 263
[18] J.S. Haggerty, and W.R. Cannon, in : J.I Steinfield (Ed), Laser Induced Chemical processes, Plenum Press,New York, p. 165, (1981)
[19] G. Ledoux, D. Amans , J. Gong, F. Huisken, F. Cichos and J. Martin: Mater. Scien. and Engin. C Vol. 19 (2002), p. 215
[20] E. Figgemeier, W. Kylberg, E. Constable, M. Scarisoreanu, R. Alexandrescu, I. Morjan, I. Soare, R. Birjega, E. Popovici, C. Fleaca, L. Gavrila-Florescu and G. Profan: Appl. Surf. Scien. Vol. 254 (2007), p. 1037
[21] D. Pokorna, J. Bohacek, V. Vorlicek, J. Subrt, Z. Bastl, E. A. Volnina and J. Pola: J. Anal. Appl. Pyrolysis Vol. 75 (2006), p. 65
[22] O.Sublemontier, F. Lacour, Y. Leconte, N. Herlin-Boime and C. Reynaud: J. Alloys Compd Vol. 483 (2008), p. 499
[23] H. Maskrot, N. Herlin-Boime1, Y. Leconte, K. Jursikova, C. Reynaud1 and J. Vicens: J. Nanoparticle Res. Vol. 8 (2006) , p. 351
[24] G. Peters, K. Jerg, and B. Schramm:Materials: Chemisrty and Physics Vol. 55 (1998), p. 197
[25] A. Galvez, N. Herlin-Boime, C. Reynaud, C. Clinard and J. Rouzaud: Carbon Vol. 40 (2002), p. 2775
[26] J. Förster, M. von Hoesslin and J. Uhlenbusch: Appl. Phys. B Vol. 62 (1996), p.609
[27] B. W. Mwakikunga, A. Forbes, E. Sideras-Haddad and C. Arendse: Nanoscale Res Lett Vol. 3 (2008), p. 372
[28] B.W Mwakikunga, E. Sideras-Haddad, C Arendse, M. J. Witcomb and A. Forbes: J. Nanosci. & Nanotechnol. Vol. 9 (2009), p. 3286

Optimization of the laser pyrolysis parameters to synthesis vanadium oxide (VO_{2+x}) nanostructures

Lerato Shikwambana[1, 3], Malcolm Govender[1, 3], Bonex. Mwakikunga[1,3], Andrew Forbes[1, 2], and Elias Sideras-Haddad[3]

[1] *CSIR National Laser Centre, P. O. Box 395, Pretoria 0001, South Africa*
[2] *School of Physics, University of KwaZulu-Natal, Private Bag X54001, Durban 4000, South Africa*
[3] *School of Physics, University of Witwatersrand, Private Bag 3, PO Wits 2050, Johannesburg, South Africa*
Author e-mail address: lshikwambana@gmail.com

Abstract: A laser pyrolysis (LP) technique was used to synthesisVO_{2+x} nanostructures at a wavelength of 10.6 µm and power density of 2.4 kW/cm^2. Scanning electron microscopy (SEM) showed nano-rods with lengths of 185 nm and diameters of 53 nm. Energy dispersive x-ray (EDX) analysis established the presence of vanadium oxide.

1. Introduction

Vanadium dioxide (VO_2) shows a reversible metal-to-semiconducting transition at 68^{o}C [1]. This reversible feature provides potential and important applications which include data storage, intelligent window coatings, and infrared modulators. Laser pyrolysis is the preferred method of VO_2 synthesis because it has a well defined interaction volume and produces pure product [2, 3]. [2] demonstrated how a resonant interaction between a laser beam and a precursor (liquid or gaseous) could lead to a desired product. Laser pyrolysis parameters; beam waist, beam quality, power density and flow rates determine what products and structures are formed during the reaction, so it is of the essence that these parameters be studied fully so as to know which structures and products will be formed during certain conditions. In this work we report on the experimental conditions used to obtain VO_{2+x} nano-rods.

2. Results

A continues wave CO_2 laser beam with a beam waist of 0.89 mm and power density of 2.4kW/cm^2 was used to synthesis VO_{2+x} nanostructures. Argon and acetylene carrier gases had flow rates of 12 ml/min and 15 ml/min respectively. Depositions were made for 20 minutes and the resulting thin film was annealed under argon atmosphere for 17 hours at 500^{o}C. SEM showed nano-rods with lengths of 185 nm and diameters of 53 nm. EDX analysis confirmed the presence vanadium oxide.

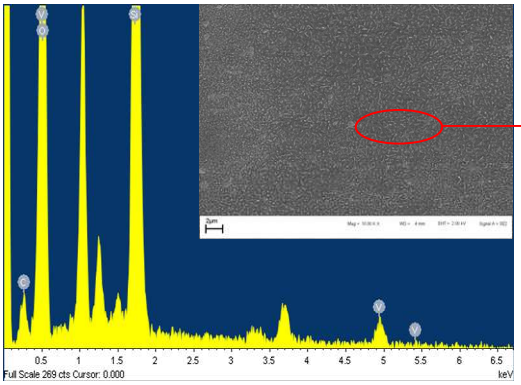

Figure 1:SEM micrographs of VO_{2+x} nano-rods and EDX analysis of the nanostructures at X10000 magnification.

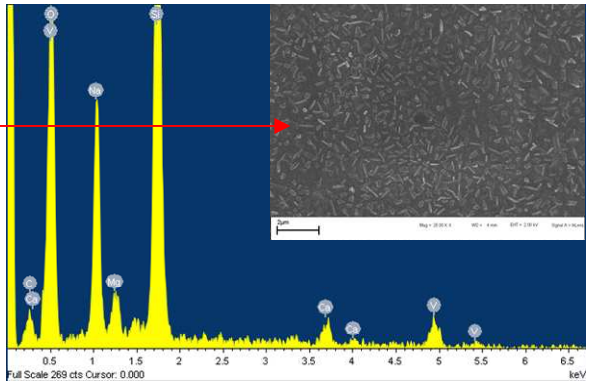

Figure 2:SEM micrographs of VO_{2+x} nano-rods and EDX analysis of the nanostructures at X25000 magnification.

3. References

[1] R.Lopez, L.A. Boatner, T.E. Haynes, L.C. Feldman, and R.Hugland, J.Appl.Phys. 92 4031, (2002)
[2] J.S. Haggerty, and W.R. Cannon, in:J.I Steinfield (Ed), Laser Induced Chemical processes, Plenum Press,New York, p165, (1981)
[3] B.W. Mwakikunga, A.Forbes, E.Sideras-Haddad, R.M. Erasmus, G.Katumba, and B.Masina, Int.J. Nanoparticles, Vol1, No.3, (2008)